

# PROPERTIES OF SOFT X-RAY BRIGHT ACTIVE GALACTIC NUCLEI

Thesis submitted for the degree of  
Doctor of Philosophy  
at the University of Leicester.

by

Simon Vaughan  
X-ray Astronomy Group  
Department of Physics and Astronomy  
University of Leicester

May 16, 2001

UMI Number: U594565

All rights reserved

INFORMATION TO ALL USERS

The quality of this reproduction is dependent upon the quality of the copy submitted.

In the unlikely event that the author did not send a complete manuscript and there are missing pages, these will be noted. Also, if material had to be removed, a note will indicate the deletion.



UMI U594565

Published by ProQuest LLC 2013. Copyright in the Dissertation held by the Author.  
Microform Edition © ProQuest LLC.

All rights reserved. This work is protected against  
unauthorized copying under Title 17, United States Code.



ProQuest LLC  
789 East Eisenhower Parkway  
P.O. Box 1346  
Ann Arbor, MI 48106-1346

## **Declaration**

I hereby declare that no part of this thesis has been previously submitted to this or any other University as part of the requirement for a higher degree. The work described herein was conducted by the undersigned except for contributions from colleagues as acknowledged in the text.

**Simon Vaughan,**  
**April 2001**

# Properties Of Soft X-ray Bright Active Galactic Nuclei

Simon Vaughan

## Abstract

Studies of the extremes of behaviour observed in Active Galactic Nuclei (AGN) constrain the physics of their emission processes by pushing existing models to their limits. Narrow-Line Seyfert 1 (NLS1s) represent one extreme of the AGN phenomenon, and soft X-ray selection is an efficient way to find NLS1s. This thesis examines the X-ray and optical properties of soft X-ray bright AGN and NLS1s in particular.

The X-ray spectral properties, as observed by *ASCA*, of a sample of 22 NLS1s are discussed. The X-ray continua show a wide range in slope, with a mean only slightly steeper than that of 'normal' Seyfert 1s and most show 'soft excess' emission, often containing a significant fraction of the X-ray luminosity. In addition, some NLS1s show spectral features in the range 0.7–0.9 keV and 1.1–1.4 keV, which are described in terms of absorption in photoionised material along the line-of-sight. The X-ray properties of the bright NLS1 Ark 564 are examined in detail and the X-ray spectrum is found to be consistent with a model comprising a power-law plus 'reflection' from ionised matter.

A re-analysis of the *ROSAT* Wide Field Camera all-sky survey data is presented. A total of 19 AGN are detected in the extreme-ultraviolet, including eight NLS1s, making this the first complete sample to contain a high fraction of NLS1s. This work is extended using a larger, complete sample of AGN selected on the basis of 0.25 keV flux. Correlations between the measured X-ray and optical properties are discussed and the sample is used to isolate objects at the extreme ends of the parameter space explored. The luminosity function of the sample is presented, along with the luminosity functions of Seyferts classified on the basis of  $H\beta$  width and X-ray spectral slope.

## **Publications**

A significant amount of the work contained in this thesis has been published, or is due to be published, elsewhere as:

Edelson, R., Vaughan, S., Warwick, R., Puchnarewicz, E., George, I., 1999, *Mon. Not. R. Ast. Soc.*, **307**, 91

*“The ROSAT Wide Field Camera extragalactic survey”*

Vaughan, S., Pounds, K., Reeves, J., Warwick, R., Edelson, R., 1999, *Mon. Not. R. Ast. Soc.*, **308**, L34

*“Evidence for an ionized accretion disc in the Narrow-line Seyfert 1 galaxy Ark 564”*

Vaughan, S., Reeves, J., Warwick, R., Edelson, R., 1999, *Mon. Not. R. Ast. Soc.*, **309**, 113

*“X-ray spectral complexity in Narrow-line Seyfert 1 galaxies”*

Vaughan, S., Edelson, R., Warwick, R. S., Malkan, M. A., Goad, M. R., 2001, *Mon. Not. R. Ast. Soc.*, **submitted**

*“A complete sample of Seyfert galaxies selected at 1/4 keV”*

## Acknowledgements

There are many, many people without whom this thesis would not have happened. My supervisor Bob Warwick and co-supervisor Rick Edelson are foremost among these – between them they have taught me pretty much all of what I know about X-ray astronomy and provided the support to keep this project going for three years. My other main collaborators for this work were Ken Pounds and James Reeves, both of whom added significantly to the work in chapters 2 and 3. Ian George originally had the idea which became the WFC sample and Liz Puchnarewicz helped collect the identifications for that sample. Matt Malkan helped collect and interpret the optical data of the *ROSAT* soft sample and let me stay at his house when I was in Los Angeles. Martin Ward and Paul O'Brien also gave me plenty of useful advice throughout the course of this work.

The builders, maintainers and operators of the telescopes used in this work also deserve thanking. Thanks to all those people on the *ROSAT*, *ASCA*, *BeppoSAX* and *RXTE* projects, and to the staff of the ING and Lick observatories. The LEDAS and HEASARC databases were also used extensively in this work. The *RXTE* GOF were particularly nice to me during my brief stay at GSFC and I thank them all for that and for staying in line long enough to get those extra cinema tickets. Without Tess Jaffe's fantastic script REX the *RXTE* analysis would have been infinitely more tedious. I also found Dick Willingale's funky but flaky program Q almost indispensable.

I also want to thank the Leicester postgrads and postdocs who did their best to distract me from finishing *that last bit of work*: Matt Burleigh (it's not paranoia when they're really after you!), Gareth for being Welsh, Paul 'gums' Dobbie, Westie for convincing me Fosters isn't a *real* drink, Steve 'the sharp' Sembay, Darren for never asking an astronomer, Cap'n Kevin (the sqiz), Keith for being American only when he wants to be, Tim for knowing his way around Edinburgh, Mike for demonstrating DIPSomania, Martin Wace for always picking the leaky glass, PJ and Duncan (Biker Grove anyone?), Steve and Greg for surreal lunch-time conversations, Graham the Mackam, Becky the Welsh Mackam, Sergio ('I need to eat!'), Paulina and even Scrunchy ('what's wrong with...?'). I must also thank the staff of Leicester's pubs, clubs and restaurants for providing enough distractions to guarantee I couldn't finish this thesis on time.

**“Well, the thing about a Black Hole - its main distinguishing feature - is it’s black. And the thing about space - your basic space colour is black. So how are you supposed to see them?”**

# Contents

<b>1</b>	<b>Introduction</b>	<b>1</b>
1.1	Overview . . . . .	1
1.2	Active Galactic Nuclei . . . . .	1
1.3	Taxonomy of Active Galactic Nuclei . . . . .	2
1.4	The black hole paradigm . . . . .	3
1.4.1	Accretion power . . . . .	4
1.4.2	Evidence in support of the black hole model . . . . .	5
1.5	X-ray properties of Seyfert galaxies . . . . .	7
1.5.1	X-ray spectra . . . . .	7
1.5.2	X-ray variability . . . . .	9
1.6	Narrow-line Seyfert 1 galaxies . . . . .	10
1.7	Conventions . . . . .	13
<b>2</b>	<b>The X-ray Spectra of Narrow-Line Seyfert 1 Galaxies</b>	<b>14</b>
2.1	Overview . . . . .	14
2.2	Observations and data reduction . . . . .	14
2.3	X-ray spectral analysis . . . . .	16
2.3.1	Initial spectral fits . . . . .	16

2.3.2	The 2–10 keV spectral form . . . . .	17
2.3.3	The soft X-ray spectra . . . . .	21
2.4	Discussion . . . . .	24
2.4.1	The hard X-ray continua of NLS1s . . . . .	24
2.4.2	The soft X-ray excess . . . . .	26
2.4.3	Iron $K_{\alpha}$ emission . . . . .	27
2.4.4	Soft X-ray spectral features . . . . .	27
2.5	Spectral variability . . . . .	30
2.6	Notes on the spectral fitting of individual objects . . . . .	30
<b>3</b>	<b>X-ray Properties of Arakelian 564</b>	<b>38</b>
3.1	Overview . . . . .	38
3.2	Arakelian 564 . . . . .	38
3.3	Observations and data reduction . . . . .	39
3.3.1	The ASCA observations . . . . .	39
3.3.2	The RXTE observations . . . . .	40
3.4	Spectral analysis . . . . .	41
3.4.1	The 3–18 keV spectrum . . . . .	42
3.4.2	The 0.8–18 keV spectrum . . . . .	45
3.5	Temporal analysis . . . . .	48
3.6	Discussion . . . . .	49
<b>4</b>	<b>The ROSAT Wide-Field Camera Extragalactic Survey</b>	<b>51</b>
4.1	Overview . . . . .	51
4.2	The ROSAT survey . . . . .	51

4.3	The Source Catalogue . . . . .	52
4.3.1	The Extragalactic Sources . . . . .	53
4.3.2	Notes on Individual Sources . . . . .	53
4.3.3	The Galactic Sources . . . . .	57
4.4	The Extragalactic Sample of EUV-Selected Sources . . . . .	59
4.4.1	Completeness of the Sample . . . . .	59
4.4.2	Comparison with Previous EUV Studies . . . . .	59
4.4.3	Comparison with a Hard X-ray Selected Sample . . . . .	60
4.4.4	The Spectral Form of the Sources . . . . .	61
4.5	The Luminosity Function of EUV-Selected AGN . . . . .	63
<b>5</b>	<b>A complete sample of soft X-ray selected AGN</b>	<b>68</b>
5.1	Overview . . . . .	68
5.2	Sample selection . . . . .	68
5.2.1	Sample completeness . . . . .	74
5.3	Optical observations of the Seyfert sample . . . . .	74
5.3.1	Fe II subtraction . . . . .	76
5.3.2	Other line measurements . . . . .	78
5.3.3	Continuum measurements . . . . .	79
5.4	Analysis . . . . .	79
5.4.1	General sample properties . . . . .	84
5.4.2	Correlations between parameters . . . . .	85
5.4.3	Outlying Seyferts . . . . .	89
5.4.4	The Seyfert Galaxy Luminosity Function . . . . .	91
5.5	Discussion . . . . .	94

<b>6</b>	<b>Conclusions</b>	<b>97</b>
6.1	Summary of results . . . . .	97
6.2	Future work . . . . .	99
<b>A</b>	<b>Optical spectra</b>	<b>101</b>
	References . . . . .	112

# Chapter 1

## Introduction

### 1.1 Overview

This introduction briefly describes some of the astrophysical background underlying the work in this thesis. It is of limited scope, but the following articles provide more thorough reviews of the relevant science. Peterson (1997) provides a well written introduction to the astrophysics of active galaxies. Rees (1984) reviews the black hole model and Frank, King & Raine (1992) detail the physics of accretion. Antonucci (1993) and Lawrence (1987) describe schemes to unify the various types of active galaxies. Mushotzky, Done & Pounds (1993) review the X-ray observations of active galaxies prior to the ASCA mission. Netzer (1991) reviews the optical emission lines and Koratkar & Blaes (1999) review the optical and ultraviolet continuum emission from active galaxies.

### 1.2 Active Galactic Nuclei

Active Galactic Nuclei (AGN) are the most luminous continuously emitting objects in the Universe. They exist in the centres of  $\gtrsim 1$  per cent of all galaxies (Huchra & Burg 1992) and emit radiation at all wavelengths from radio to X-rays (see Fig. 1.1), with a total luminosity of  $L_{bol} \gtrsim 10^{45}$  erg s<sup>-1</sup>, often exceeding the host galaxy of  $\sim 10^{11}$  stars. The Spectral Energy Distributions (SEDs) of AGN can usually be described, to first order at least, as a power-law,  $F_\nu \propto \nu^{-\alpha}$  with  $\alpha \sim 1$ . This emission spectrum is too broad to be produced by a single thermal source and so requires non-thermal or multiple emission components.

### 1.3 Taxonomy of Active Galactic Nuclei

AGN display a wide range of observed properties. The different classes of AGN have historically been defined in terms of their optical spectral properties and radio morphologies. The two largest classes of AGN are Seyfert galaxies and quasars, which are the main concern of this work, but for completeness the properties of all the main classes of AGN will now be described.

- *Seyfert 1 galaxies/radio-quiet quasars:* Also known as type-I AGN, these objects show strong, Doppler-broadened (up to  $10^4$  km/s) optical emissions lines. The Broad Line Region (BLR) responsible for these emission lines is thought to be typically  $\sim 10$  light days in size for Seyferts up to a few hundred lt-day for higher luminosity objects (Kaspi *et al.* 2000). The line emission is driven by photoionisation from the central continuum source. Type-I AGN also show narrow (FWHM  $\sim 500$  km/s) permitted and forbidden emission lines originating in more distant, lower density gas ( $\sim 100$  pc).

Salient features of the SED include a bump rising through the ultraviolet (often called the ‘Big Blue Bump,’ or BBB), a sudden drop in flux below  $100 \mu\text{m}$  (the ‘millimeter break’), and strong X-ray emission. The X-ray emission shows rapid variability on time-scales of  $\sim$ ks (e.g. Mushotzky, Done & Pounds 1993), the ultraviolet and optical continua vary over days (e.g. Edelson, Pike & Krolik 1990), while the infrared emission shows little variability (Edelson & Malkan 1987; Sembay, Hanson & Coe 1987). This suggests that the X-ray component is produced in the innermost regions of the central engine, with emission in other wavebands produced further out.

The distinction between Seyfert 1 galaxies and radio-quiet quasars now depends almost entirely on the luminosity of the central object, with Seyfert 1 galaxies being the lower-luminosity of the two. The dividing bolometric luminosity is loosely defined to be around  $L_{bol} \sim 10^{45}$  erg/s, or an absolute optical magnitude of  $M_B \sim -23$ . Seyfert 1s and radio-quiet quasars will be treated as essentially the same type of object throughout this thesis.

- *Seyfert 2 galaxies:* Often referred to as type-II AGN, these show similar narrow optical lines as Seyfert 1s but weak and narrow permitted emission lines and weaker optical/ultraviolet continuum emission. At sufficiently long wavelengths, or in polarised light (e.g. Antonucci & Miller 1985), many Seyfert 2s show permitted emission lines similar to Seyfert 1s, suggesting they possess hidden BLRs. Seyfert 2s also often show strong photoelectric absorption of X-rays, indicating a

large column of cold material along the line of sight ( $\gtrsim 10^{23} \text{ cm}^{-2}$ ; see eg. Done & Smith 1996), often identified with the material obscuring the BLR.

- **LINERS:** Low-Ionisation Nuclear Emission-line Region galaxies (Heckman 1980) represent the low-luminosity end of the range of AGN. They possess optical line spectra similar to Seyfert 2s but with relatively stronger low-ionisation lines such as [O I]  $\lambda$ 6300, which may either be driven either by shocks or by photoionisation as in other AGN (Ho, Filippenko & Sargent 1993; Terashima, Ho & Ptak 2000).
- **Radio galaxies:** Distinguished from other AGN on the basis of their spatially extended radio-lobes and jets, radio galaxies resemble the radio-loud counterparts of Seyfert galaxies. Broad-line radio galaxies (BLRGs) show nuclear emission lines similar to Seyfert 1s while narrow-line radio galaxies (NLRGs) show similarities to Seyfert 2 nuclei.
- **Radio-loud quasars:** These quasars show radio emission typically two orders of magnitude brighter, relative to the optical continuum, than radio-quiet quasars (e.g. Kellermann *et al.* 1989). The radio emission from these luminous objects is dominated by the central AGN core and not extended radio lobes as in radio galaxies. The X-ray spectra of radio-loud quasars tend to be harder than those of radio-quiet quasars and Seyfert 1 nuclei (the SED for a radio-loud quasar is shown in Fig. 1.1).
- **Blazars:** Blazars show strong and highly variable continuum emission at all wavelengths and are always radio-loud. There are two types of Blazars, optically-violet variable (OVV) and BL Lacertae objects, distinguished by the presence or absence of emission lines, respectively. The most common model for BL Lacs is that their emission is relativistically beamed along our line-of-sight (Blandford & Rees 1978).

## 1.4 The black hole paradigm

The power source responsible for the prodigious energy output of AGN, the compact ‘central engine,’ is thought to be a supermassive black hole of mass  $10^6 - 10^9 M_{\odot}$  accreting material from the surrounding galaxy.

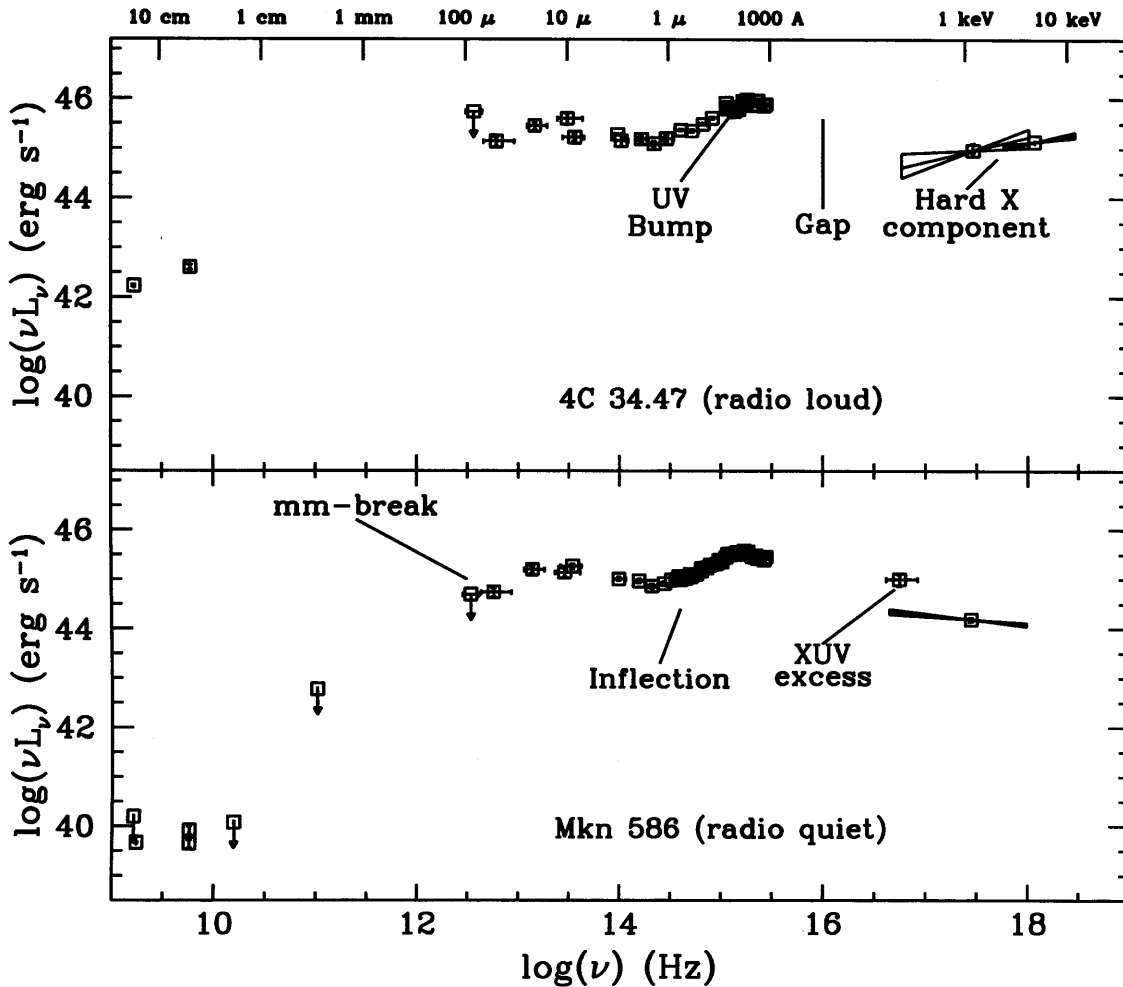


Figure 1.1: Examples of the Spectral Energy Distribution (SED) for a radio-loud (top) and a radio-quiet (bottom) quasar (from Elvis *et al.* 1994). Plotted as  $\log(\nu F_\nu)$  these show energy emitted per equally spaced logarithmic frequency interval.

#### 1.4.1 Accretion power

Material falling towards the black hole invariably possesses some angular momentum which prevents it from falling directly into the hole. Instead it forms an *accretion disc* capable of transporting the angular momentum outward (Lynden-Bell 1969; Pringle 1981). The mechanism of angular momentum transport, usually called 'viscosity,' is still unclear but is thought to be related to the magnetic field carried by the accreting matter. As the material loses angular momentum it spirals in to tighter orbits and gravitational potential energy is released. A significant amount of the rest-mass of the accreting matter can be converted to energy: around a non-rotating (Schwarzschild) black hole the efficiency of accretion

can be  $\eta \sim 0.06$ , increasing to  $\eta \sim 0.3$  for a rapidly rotating (Kerr) black hole (Thorne 1974). This process is the second most efficient known, after matter/anti-matter annihilation. The energy released is converted into observed radiation through, for example, viscous dissipation, shocks, magnetic fields and gas reprocessing. The foundations of the theory of radiative accretion discs were laid down by Shakura & Sunyaev (1973) and others in the context of X-ray binaries.

A useful measure of accretion rate is the *Eddington limit*. This is reached when the accretion rate is so high that the pressure of the outflowing radiation balances the force of the infalling gas (for spherical accretion). Equating the forces of radiation and gravity gives the Eddington luminosity:

$$L_{Edd} = \frac{4\pi G c m_p}{\sigma_e} M$$

where  $M$  is the mass of the central black hole,  $m_p$  and  $\sigma_e$  are the proton mass and Thompson cross-section, respectively. The mass accretion rate at the Eddington luminosity is given by  $\dot{M}_{Edd} = L_{Edd}/\eta c^2$ .

The temperature of a standard accretion disc can be expressed in terms of the fraction of Eddington accretion rate ( $\dot{m} = \dot{M}/\dot{M}_{Edd}$ ):

$$T(r) \approx 6.3 \times 10^5 \dot{m}^{1/4} M_8^{-1/4} r^{-3/4} \text{K}$$

where  $M_8$  is the mass of the black hole in units of  $10^8 M_\odot$  and  $r$  is the radius in units of the Schwarzschild radius. For a Seyfert galaxy with a black hole of  $10^7 M_\odot$  accreting at  $\dot{m}=0.1$ , the emission from the inner regions of the accretion disc is expected to peak around  $\sim 100$  eV. This thermal emission from the accretion disc is then a good candidate for the BBB emission in Seyfert 1s and quasars (Shields 1978; Malkan & Sargent 1982). Unfortunately the peak of the emission occurs in the far-ultraviolet and extreme ultraviolet (EUV), which are difficult to observe due to absorption by Galactic interstellar material.

#### 1.4.2 Evidence in support of the black hole model

Obtaining direct evidence for the existence of black holes in the centres of active galaxies has proven difficult and some of the success of the black hole paradigm must be put down to a lack of serious alternatives. The strongest evidence in support of the black hole model includes:

- *Iron line profile:* The strong iron  $K_{\alpha}$  fluorescence line seen in the X-ray spectrum of many Seyfert 1s possesses a broad and asymmetric profile (Tanaka *et al.* 1995; Nandra *et al.* 1997b; Nandra *et al.* 1999). The line is thought to originate from the innermost regions of the central engine, close to the putative black hole and the line profile reveals the strong Doppler and gravitational redshifts in this region. The iron line has provided perhaps the best evidence to date for the existence of black holes in the centres of AGN.
- *X-ray variability:* Seyfert 1 galaxies often exhibit rapid X-ray variability. The variability time-scales show that a significant fraction of the luminosity is radiated from compact regions of  $< 1$  day. This variability can also be used to estimate the radiative efficiency  $\eta$  (Fabian 1979). The high efficiencies  $\eta \sim 0.05$  derived from AGN light curves (see e.g. McHardy 1989) provided some of the first, strong evidence for accretion onto a black hole.
- *Reverberation mapping:* Measuring correlated variability of the optical/ultraviolet emission lines and continua of Seyfert 1s and quasars through ‘reverberation mapping’ (Blandford & McKee 1982; Peterson 1993; Netzer & Peterson 1997) can in principle determine the kinematics of the line emitting region. If the motions of the BLR gas are dominated by the gravity of the central object then reverberation mapping can provide an estimate of its mass. Typical masses for the central object in Seyfert 1s are in the range  $\sim 10^7 - 10^8 M_{\odot}$  (e.g. Wandel, Peterson & Malkan 1999).
- *Maser emission:* A few AGN produce strong, narrow maser emission lines. Precise measurements of the nucleus of the Seyfert 2 NGC 4258 have revealed the masing material to be in orbit around a central, compact object of mass  $\sim 10^7 M_{\odot}$  (Watson & Wallin 1994; Greenhill *et al.* 1995).
- *Dynamical Studies:* Measurements of the dynamics of stars and gas in the centre of our Galaxy (Ghez *et al.* 1998) and nearby galaxies (eg. Kormendy & Richstone 1995; Gebhardt *et al.* 2000) suggest the presence of central, compact, dark objects of masses  $\sim 10^6 - 10^{9.5}$ . These studies provide indirect evidence supporting the claim that many galaxies harbour central, supermassive black holes.
- *Radio Jets:* The jets in extended radio galaxies are able to maintain a fixed direction for  $\gtrsim 10^7$  years, indicating a highly stable, powerful central engine. The power released in radio jets, and the relativistic speeds in some examples (inferred from ‘superluminal motion,’ e.g. Blandford, McKee & Rees 1977) are best explained by production in a relativistically deep potential well.

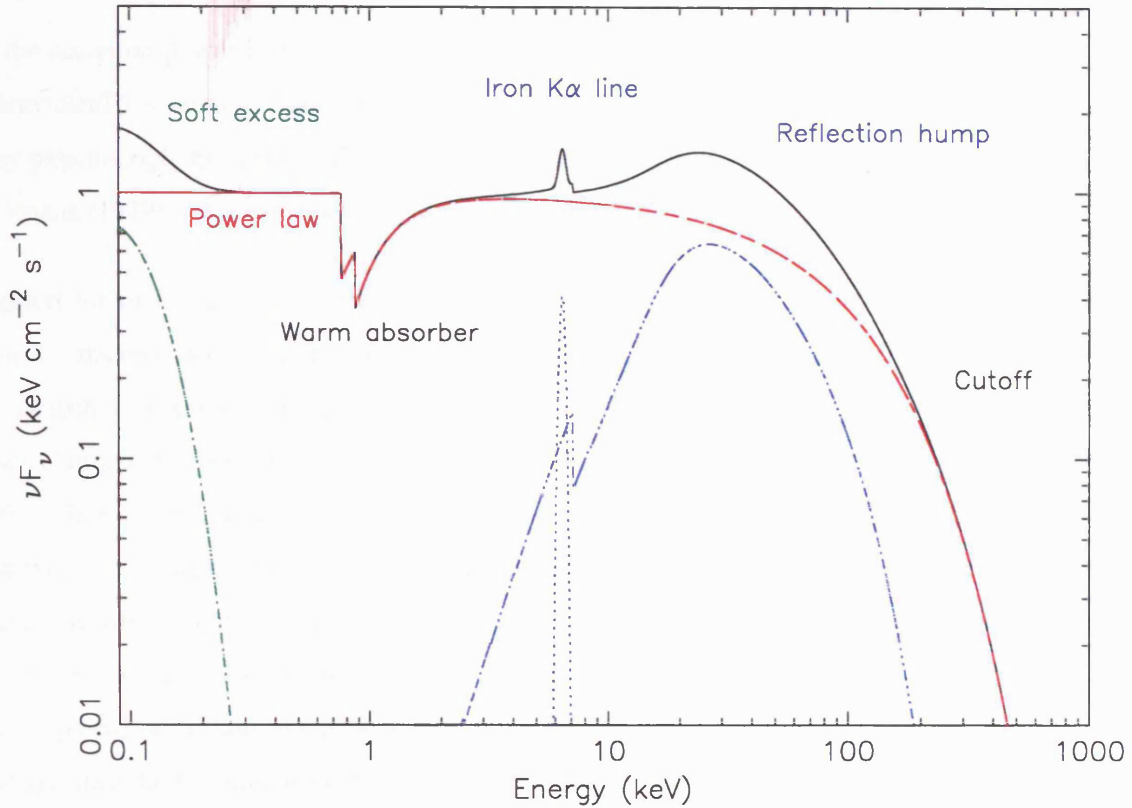


Figure 1.2: A schematic of the major components thought to comprise the X-ray spectrum of a Seyfert 1 galaxy. Shown are the X-ray power law ( $\Gamma = 2.0$ ) with an exponential cut-off, iron line and reflection continuum, warm absorber edges from O VII and O VIII, and a soft excess in the form of a blackbody.

## 1.5 X-ray properties of Seyfert galaxies

### 1.5.1 X-ray spectra

Significant hard X-ray luminosity is now regarded as one of the defining characteristics of Seyfert 1 galaxies (Elvis *et al.* 1978; Tananbaum *et al.* 1979). The hard X-ray spectra of many Seyfert 1s is dominated by a continuum component that is well described by power-law with a photon index of typically  $\Gamma = 1.9$  (Nandra & Pounds 1994), containing  $\sim 10$  per cent of the bolometric luminosity. (Note that the photon index is defined by  $P_E$  [photons  $s^{-1} \text{ keV}^{-1}$ ]  $\propto E^{-\Gamma}$ ;  $\alpha = \Gamma - 1$ .) In many Seyfert 1s additional spectral features are observed, some of which are illustrated in Fig. 1.2.

One favoured model for the X-ray emission in Seyfert nuclei has the X-ray continuum produced in a hot ( $\sim 10^8 - 10^9$  K) optically-thin corona lying above and below the surface of the putative accretion disc (e.g. Haardt & Maraschi 1993; see Fig. 1.3). In such accretion disc corona models, some fraction

of the accretion power is deposited in the corona, possibly via magnetic field lines threading the disc. Ultraviolet/EUV photons from the disc are inverse-Compton scattered to X-ray energies (up-scattered) as they pass through the corona. Models of accretion disc coronae were first developed by Galeev, Rosner & Vaiana (1979) and are reviewed by Svensson (1996) and Haardt (1997).

Support for such a geometry comes from observations of a spectral up-turn above 10 keV and strong iron  $K_{\alpha}$  fluorescence in the 6–7 keV band (Pounds *et al.* 1990; Nandra & Pounds 1994), which can be attributed to reprocessing of the X-ray continuum by optically-thick matter, possibly the accretion disc (Guilbert & Rees 1988; Lightman & White 1988; George & Fabian 1991; Matt, Perola & Piro 1991). In this scenario the X-ray source illuminates the accretion disc, with photons either absorbed and thermalised within the disc or ‘reflected’ (Compton back-scattering plus fluorescence), producing a characteristic reflection hump and line emission. Medium resolution *ASCA* spectra have shown that the iron  $K_{\alpha}$  line is often significantly broadened and redshifted (Tanaka *et al.* 1995; Nandra *et al.* 1999), with a profile of the sort that Fabian *et al.* (1995) argue is best explained by a combination of Doppler and gravitational redshifts from the inner parts of a disc around a supermassive black hole.

Many Seyfert 1s show an excess of soft X-ray emission (Arnaud *et al.* 1985; Bechtold *et al.* 1987), above the hard X-ray power-law (Figs. 1.1 and 1.2), which may represent the high energy (Wien) tail of the thermal emission of the disc (e.g. Czerny & Elvis 1987). As such the soft excess may be the internally generated thermal emission or the reprocessed X-ray continuum, or both. It is not clear whether the soft excess is connected to the BBB seen in quasars.

Recent interest has also focussed on the detection of so-called warm (i.e. partially ionised) absorption features in the soft X-ray spectra of Seyfert galaxies, which are an imprint of photoionised material along the line-of-sight to the nuclear source (e.g. Nandra & Pounds 1992). Soft X-ray photons are photoelectrically absorbed by high ionisation species, particularly of oxygen because of its high abundance, producing absorption edges in the X-ray spectrum (Netzer 1993). Such material was first suggested to explain the complex, variable spectrum of QSO MR 2251–178 by Halpern (1984) and has since been found to be a common feature in the X-ray spectra of Seyfert 1s. Reynolds (1997) and George *et al.* (1998) found that  $\sim 50$  per cent of the Seyfert 1s in their samples showed signs of warm absorption edges corresponding to O VII (at 0.74 keV) and/or O VIII (at 0.87 keV; see Fig. 1.2). The geometry of the absorbing material is unclear at present, but it is thought to lie no more than a few parsecs from the central engine

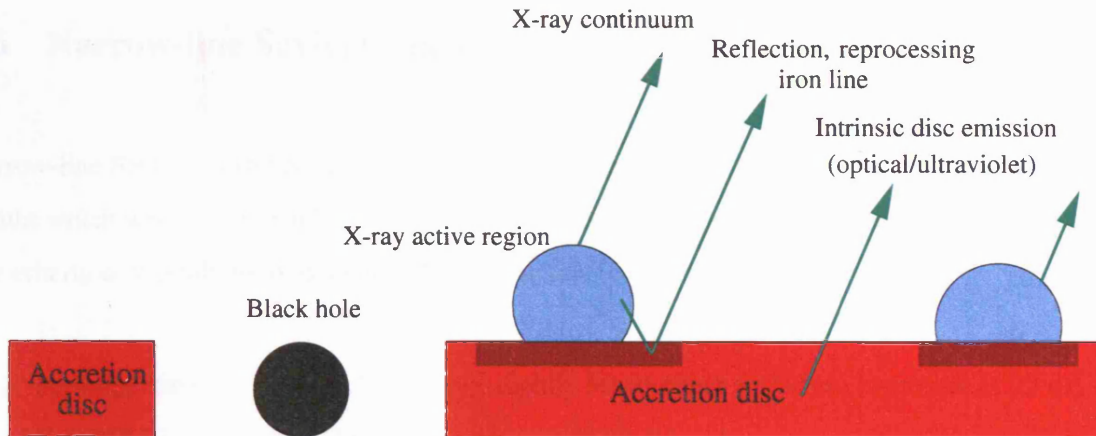


Figure 1.3: A cartoon for one model of the central regions of a Seyfert galaxy. Ultraviolet continuum emission is produced by thermal emission from the accretion disc. X-ray emission is produced by inverse-Compton scattering of low-energy photons in active regions within a hot corona. The X-ray emission then illuminates the cooler accretion disc, these photons are either absorbed and thermalised or reflected back out of the disc.

### 1.5.2 X-ray variability

It was realised relatively early on that significant X-ray flux variability was a common property of Seyfert 1 galaxies (Marshall, Warwick & Pounds 1981; Barr & Mushotzky 1986; Pounds, Turner & Warwick 1986). The rapid variability often implies small size-scales and high efficiencies, and could be a direct probe of the innermost regions of the accretion disc. AGN variability appears to be aperiodic, with featureless power density spectra (PDS) usually well described by a power-law  $P(f) \propto f^{-\alpha}$ , with  $\alpha$  typically in the range 1.5–2.0 (Green, McHardy & Lehto 1993; Lawrence & Papadakis 1993). This ‘red noise’ character of the variability means that the variability amplitude tends to be dominated by long timescale trends in the light curve. A break in the PDS at a time-scale of  $\sim 1$  month in the PDS of NGC 3516 represents one of the very few characteristic time-scales observed in AGN (Edelson & Nandra 1999; see also Uttley 2000), although its origin remains unclear.

Recent multi-wavelength campaigns to monitor Seyfert 1s (eg. Nandra *et al.* 1998; Uttley *et al.* 2000; Chiang *et al.* 2000; Edelson *et al.* 2000) suggest that the EUV through hard X-ray variability is strongly correlated, but that this variability is not correlated with the optical/ultraviolet variability. This argues against models whereby the ultraviolet emission is produced through thermal reprocessing of primary X-rays in the disc. (The relative luminosities in the ultraviolet and X-ray bands also show simple reprocessing models like this to be untenable in many cases.)

## 1.6 Narrow-line Seyfert 1 galaxies

Narrow-line Seyfert 1s (NLS1s) are a subclass of Seyfert 1 galaxies with unusually narrow optical line widths which were first identified as worthy of study by Osterbrock & Pogge (1985). The rather subjective criteria commonly used to identify NLS1s include (e.g. Goodrich 1989):

1. Permitted lines such as  $H\beta$   $\lambda 4861$  only slightly broader than forbidden lines such as  $[O\ III] \lambda 5007$  (e.g.  $H\beta$  FWHM  $\leq 2000$  km s $^{-1}$ )
2. Strong permitted line compared to forbidden lines such as  $[O\ III]$  and  $[S\ II]$  (e.g.  $[O\ III] / H\beta \leq 3$ )
3. Emission from Fe II or higher ionisation lines such as  $[Fe\ VII] \lambda 6087$  and  $[Fe\ X] \lambda 6375$

This first criteria places NLS1s very close to Seyfert 2s in the classification scheme of Khachikian & Weedman (1974), leading to many NLS1s being misclassified as Seyfert 2s (see discussions in Halpern & Oke 1987 and Pogge 2000), but criteria 2 and 3 ensure these objects are genuine Seyfert 1s (e.g. Shuder & Osterbrock 1981). It is now clear that NLS1s are not rare and that they form one end of a continuous distribution of permitted line widths in Seyfert 1 galaxies. In this work NLS1s will be loosely defined as Seyfert 1s with  $H\beta$  FWHM  $\leq 2000$  km s $^{-1}$ , while Seyfert 1s with broader lines will generally be referred to as Broad-line Seyfert 1s (BLS1s).

Early interest in NLS1s came from optical emission line studies. Boroson & Green (1992) identified a set of strong correlations between various optical properties of 87 PG quasars. This set of correlations, often referred to as the ‘primary eigenvector’ in the literature, is primarily an anti-correlation between the strengths of Fe II and  $[O\ III] \lambda 5007$  but also includes the strength and width of  $H\beta$ . NLS1s tend to lie at one end of this set of correlations, having extreme values of the correlated parameters (e.g. Brandt & Boller 1998). These properties have since been found to correlate with the soft X-ray slope observed by *ROSAT* (Boller, Brandt & Fink 1996; Laor *et al.* 1997) and with the ultraviolet line emission (Corbin & Boroson 1996; Wills *et al.* 1999).

Remillard *et al.* (1991), Boller *et al.* (1993) and Forster & Halpern (1996) found strong, rapid X-ray variability in NLS1s. Since then, rapid X-ray variability has been shown to be a common property of NLS1s (e.g. Boller, Brandt & Fink 1996; Turner *et al.* 1999b), with some sources showing exceptional variability. IRAS 13224-3809 (Boller *et al.* 1997) and PHL 1092 (Forster & Halpern 1996; Brandt *et al.*

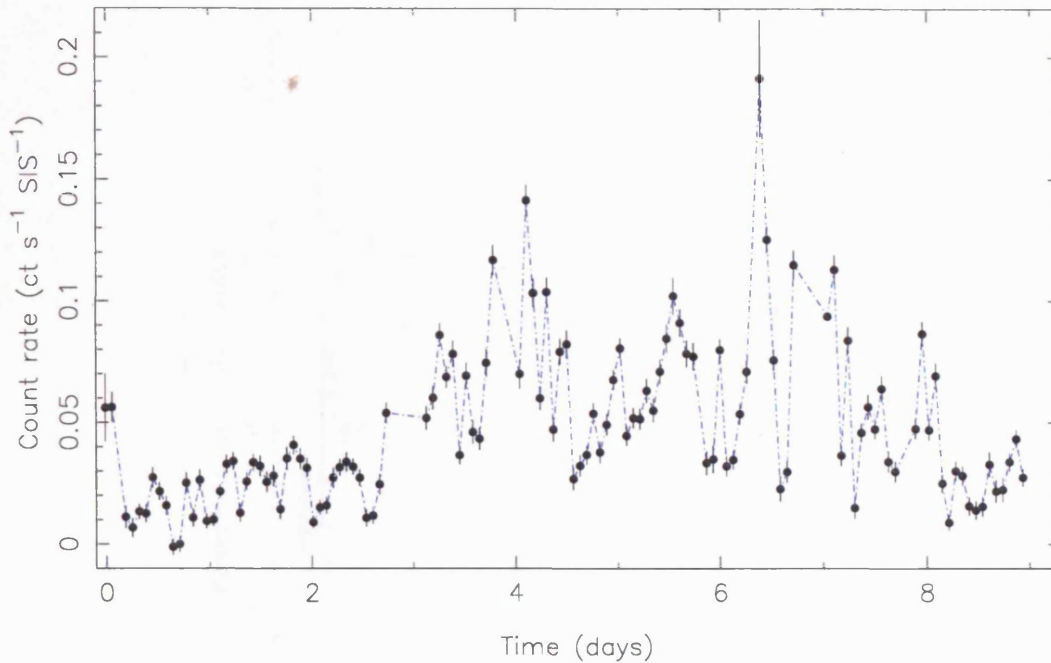


Figure 1.4: The 0.5–2 keV ASCA light curve of one of the most extreme NLS1s IRAS 13224–3809, taken in July 2000. The source shows strong and rapid variability, with factors of  $\sim 5$  variability in a few hours and a factor  $\gtrsim 30$  over the duration of the observation.

1999) in particular have shown persistent, giant, rapid variability (as much as factors of  $\sim 60$  in days; see Figure 1.4). It is now clear that, at least on time-scales of days and shorter, NLS1s show stronger X-ray variability than BLS1s (Turner *et al.* 1999b; Leighly 1999). Some AGN identified as NLS1s have displayed transient behaviour: The X-ray fluxes of WPVS 007 (Grupe *et al.* 1995a) and IC 3599 (Brandt, Pounds & Fink 1995) have dropped by  $\sim 400$  and  $\sim 80$ , respectively, on timescales of years.

Stephens (1989) first noted that X-ray selection may be an efficient way to find NLS1s. Since then soft X-ray surveys have revealed many previously unknown NLS1s (e.g. Branduardi-Raymont *et al.* 1989; Puchnarewicz *et al.* 1992; Pounds *et al.* 1993; Grupe *et al.* 1998a; Edelson *et al.* 1999). The success of soft X-ray surveys is due to the exceptional soft X-ray spectra of many NLS1s. An analysis of the soft X-ray properties of a large sample of NLS1s by Boller, Brandt & Fink (1996) showed that NLS1s tend to have unusually steep soft X-ray spectra ( $\Gamma \sim 3 - 5$ ) compared to BLS1s (but see also Xu, Wei & Hu 1999) and low intrinsic absorption. These steep spectra are due to unusually strong “soft excess” emission (e.g. Pounds, Done & Osborne 1995). This anomalous spectral steepness also extends into the 2–10 keV band in many NLS1s (Pounds, Done & Osborne 1995; Brandt, Mathur & Elvis (1997)), making NLS1s less numerous in hard X-ray surveys.

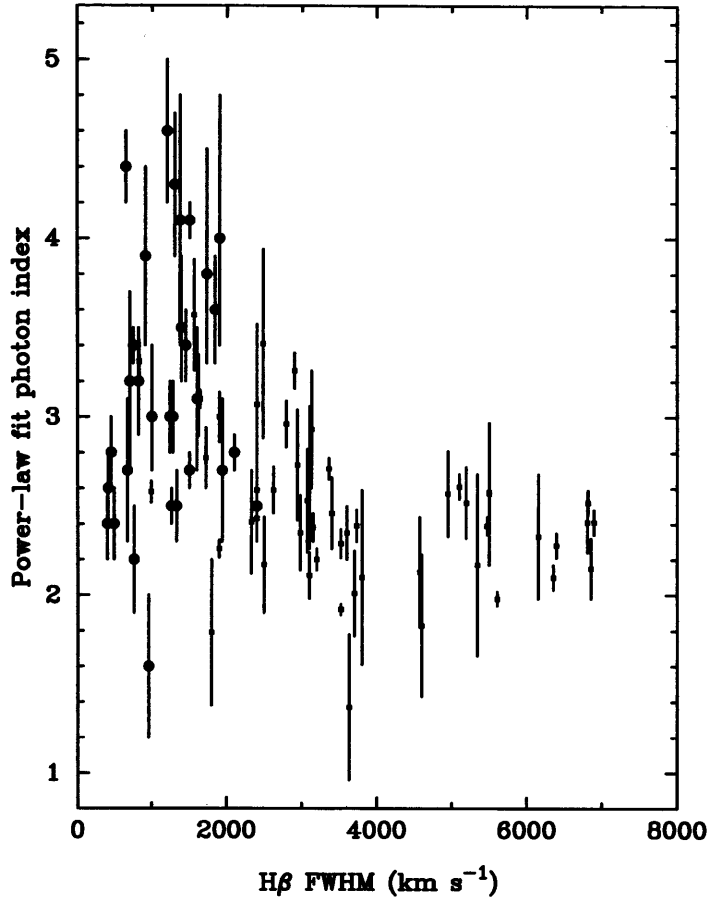


Figure 1.5: *ROSAT* photon index  $\Gamma$  against  $H\beta$  FWHM for Seyfert 1 galaxies (from Brandt 1996). The circles denote known NLS1s and the small squares the BLS1s. Note the trend for NLS1s to show steeper spectra than BLS1s.

The extreme properties reported in NLS1s (narrow permitted lines, strong soft excesses, rapid X-ray variability) might be expected to be explained by an extremal value of some underlying physical parameter. Suggestions for this physical parameter have included viewing angle of the central engine (Osterbrock & Pogge 1985; Puchnarewicz *et al.* 1992), mass accretion rate (Boroson & Green 1992; Pounds, Done & Osborne 1995) and black hole mass or spin (e.g. Boller, Brandt & Fink 1996).

The most favoured explanation for the extreme properties of NLS1s is that these are AGN containing black holes of relatively modest mass accreting at a high rate, perhaps close to the Eddington limit. Motivation for this model comes from the analogy between the X-ray spectra of NLS1s and Galactic Black Hole Candidates (GBHCs) in their ‘soft’ states (Pounds, Done & Osborne 1995). In this model, the hotter emission from the accretion disc (see § 1.4.1) provides a natural explanation for the strong soft excesses seen in NLS1s. The higher photoionising luminosity leads to a more distant BLR relative to the black hole mass (Wandel & Boller 1998; Laor 2000), which gives rise to lower Keplerian velocities of

the BLR gas and hence smaller observed optical line widths. The broadened and blueshifted ultraviolet emission lines observed in some NLS1 can be explained in terms of a radiation driven wind as might be expected in high accretion rate sources (Leighly 2000).

The X-ray spectrum should bear the signature of Compton reflection from the disc surface, which is expected to be highly ionised in high accretion rate objects (e.g., Matt, Fabian & Ross 1993). The form of the reflection features, particularly the iron K line and absorption edge and the form of the soft X-ray continuum, should therefore differ in NLS1s from BLS1s if indeed NLS1s are accreting at a higher rate. This is consistent with the possible detection of  $K_{\alpha}$  emission in hydrogen-like iron (e.g. Turner, George & Nandra 1998) in NLS1s. The steeper hard X-ray continua could arise, for example, if the strong soft excess Compton-cools the accretion disc corona in which the underlying power-law is formed (Haardt & Maraschi 1993; Pounds, Done & Osborne 1995).

Alternative models include a near face-on geometry for NLS1s, originally proposed to explain the narrow permitted line widths by Osterbrock & Pogge (1985) (see also Puchnarewicz *et al.* 1992). In this model the BLR has a flattened geometry which, when viewed face-on, shows only very small line-of-sight velocity dispersion and hence narrower lines. The strong soft excess emission in NLS1s could be due to the angular dependence of emission from the accretion disc, although this does require the accretion disc to be geometrically thick if viewed face-on (Madau 1988). In this scenario the X-ray variability may be enhanced through gravitation lensing by the black hole. Alternatively, if the disc is geometrically thin then an edge-on geometry will produce stronger soft X-ray emission. The high line-of-sight velocity of such a disc will Doppler boost the intrinsic variability, but it is difficult to see how this model explains the narrow  $H\beta$  profile.

## 1.7 Conventions

Spectral fitting of X-ray data was carried out using the XSPEC v.10 and v.11 (Arnaud 1996) software package. For the X-ray spectral analysis all errors quoted on the derived best-fit parameters correspond to a 90% confidence level for one interesting parameter (i.e. a  $\Delta\chi^2 = 2.7$  criterion) unless otherwise stated. Values of  $H_0 = 50 \text{ km s}^{-1} \text{ Mpc}^{-1}$  and  $q_0 = 0.5$  are assumed and all fit parameters quoted are for the rest frame of the source.

## Chapter 2

# The X-ray Spectra of Narrow-Line Seyfert 1 Galaxies

### 2.1 Overview

A systematic analysis of the X-ray spectral properties of a sample of 22 NLS1 is presented. Many of these sources, which were selected from the *ASCA* public archive on the basis of their relatively narrow  $H\beta$  line width ( $\text{FWHM} \leq 2000 \text{ km/s}$ ), show significant spectral complexity in the X-ray band. The chapter is organised as follows. The source sample and observations are detailed in Section 2.2 along with data reduction techniques. The results of the X-ray spectral analysis are given in Section 2.3, and discussed in Section 2.4. For completeness Section 2.5 describes a test for spectral variability in these data and Section 2.6 gives details on the spectral fits in specific objects.

### 2.2 Observations and data reduction

The sample consists of 22 objects, identified in the literature as Seyfert 1 galaxies or quasars with  $H\beta$   $\text{FWHM} \leq 2000 \text{ km s}^{-1}$ , for which *ASCA* data were publicly available at the time of the analysis (late 1998). The sample, given in Table 2.1, is not complete in any sense except that it consists of all suitable spectra of NLS1s in the *ASCA* public archive. The NLS1 galaxy Mrk 957 was also observed by *ASCA* but these data were not analysed due to the very short exposure time of the observation ( $\sim 3 \text{ ks}$ ). In addition data on Kaz 163 have been excluded because it lies in the same GIS field as Mrk 507 but its image falls at the extreme edge of the SIS detector, making the data unsuitable for detailed spectral

Table 2.1: The ASCA NLS1 sample. The columns contain the following information: (1) The source name; (2) The sequence number of the observation; (3) & (4) The observation pointing position; (5) The exposure time for SIS-0 (ks); (6) The line-of-sight Galactic hydrogen column density from Dickey & Lockman (1990) (in units of  $10^{20}$  cm $^{-2}$ ); (7) The source redshift; (8) The H $\beta$  line width (km s $^{-1}$ ); (9) References to the information in columns (7) & (8).

Name	ASCA Sequence	RA (J2000)	Dec (J2000)	SIS-0 Exp.	$N_H$	$z$	H $\beta$ FWHM	Ref.
(1)	(2)	(3)	(4)	(5)	(6)	(7)	(8)	(9)
Mrk 335	71010000	00 06 04	20 11 12	18	3.99	0.026	1640	1
I Zw 1	73042000	00 53 41	12 46 40	27	4.99	0.061	1240	2
Ton S180	74081000	00 57 28	-22 17 50	44	1.55	0.062	1000	2
PHL 1092	75042000	01 40 01	06 24 32	68	4.07	0.396	1300	2
RX J0148-27	75048000	01 48 30	-27 53 19	34	1.42	0.121	1050	3
NAB 0205+024	74071000	02 07 44	02 38 02	41	3.51	0.155	1050	4
RX J0439-45	75050000	04 40 14	-45 39 46	43	2.02	0.224	1010	3
PKS 0558-504	74096000	06 00 04	-50 22 06	33	4.39	0.137	1500	2
1H 0707-495	73043000	07 08 26	-49 37 47	34	5.80	0.040	1000	2
RE J1034+39 (1)	72020000	10 35 04	39 40 28	28	1.02	0.042	1500	2
RE J1034+39 (2)	72020010	10 34 14	39 36 05	11	1.02	0.042	1500	2
Mrk 42	75056000	11 53 12	46 11 26	36	1.99	0.024	670	2
NGC 4051 (1)	70001000	12 03 06	44 32 33	25	1.32	0.002	990	2
NGC 4051 (2)	72001000	12 02 43	44 29 50	69	1.32	0.002	990	2
PG 1211+143	70025000	12 14 13	14 03 32	13	2.74	0.080	1860	1
PG 1244+026	74070000	12 46 17	02 19 24	37	1.75	0.048	830	1
IRAS 13224-3809	72011000	13 24 52	-38 25 57	82	4.79	0.067	650	2
PG 1404+226	72021000	14 06 06	22 22 50	34	2.14	0.098	880	1
Mrk 478	73067000	14 41 43	35 24 57	29	1.03	0.079	1450	2
PG 1543+489	75059000	15 46 00	48 48 06	39	1.59	0.400	1560	1
IRAS 17020+454	73047000	17 03 09	45 36 52	35	2.22	0.060	490	2
Mrk 507	74033000	17 49 00	68 37 26	32	4.38	0.056	960	2
IRAS 20181-224	73075000	20 20 53	-22 40 10	51	5.96	0.185	580	2
Ark 564	74052000	22 42 34	29 38 21	47	6.40	0.024	750	2

REFERENCES: (1) Wang, Brinkmann & Bergeron (1996). (2) Brandt (1996). (3) Grupe (1996). (4) Zheng & O'Brien (1990).

analysis. Two objects commonly identified as NLS1s and with archival *ASCA* data were ignored on the basis of their published  $H\beta$  line widths: IRAS 13349+2438 has a measured  $H\beta$  FWHM $\sim$ 2100 km/s (Wills *et al.* 1992) and Mrk 766 has an  $H\beta$  FWHM $\sim$ 2400 (Osterbrock & Pogge 1985). The *ASCA* data of these objects have been reported in Brandt *et al.* (1997) and Leighly *et al.* (1996), respectively.

*ASCA* carries four instruments which are operated simultaneously namely two Solid-state Imaging Spectrometers (SIS-0 and SIS-1; Burke *et al.* 1991) and two Gas Imaging Spectrometers (GIS-2 and GIS-3; Kohmura *et al.* 1993). The SIS instruments operate of a nominal energy range 0.4–10 keV, with spectral resolution  $E/\Delta E \sim 50$  at 6 keV while the GIS instruments operate over 0.7–10 keV with resolution  $E/\Delta E \sim 12$  at 6 keV. More details about the *ASCA* mission are given in Tanaka, Inoue & Holt (1994).

After applying standard screening criteria (see Day *et al.* 1995) to the data, counts were accumulated, where possible, in circular apertures of 3–4 arcmin radius centred on the source. The background was estimated using source free regions from the same observation and, in the case of the GIS observations, at a similar off-axis angle to the source. After background subtraction the pulse height spectra were binned to give at least 20 counts per spectral channel. Table 2.1 lists the resulting exposure times (specifically for SIS-0, although data from all four *ASCA* instruments are utilised here). In the subsequent analysis the SIS data were restricted to the 0.6–10 keV energy range and GIS data to the 0.8–10 keV band.

## 2.3 X-ray spectral analysis

### 2.3.1 Initial spectral fits

Broadly, the analysis strategy employed was one of characterising the properties of the whole sample of sources in terms of simple spectral models. Thus initially a model comprising just a power-law continuum with absorption due to the line-of-sight Galactic  $N_H$  (see Table 2.1) was employed to illustrate the variety of X-ray spectra exhibited by NLS1 galaxies. Fig. 2.1 shows the residuals from these fits for all 24 observations, which in most instances have unacceptable minimum  $\chi^2$  values. cursory inspection of Fig. 2.1 shows that the spectra show significant curvature, being much steeper at lower energies (see also figure 3.4). In general, the iron  $K_\alpha$  emission-line is difficult to pick out (by eye), although NGC 4051 is an exception. In two sources, Mrk 507 and IRAS 20181-224, the largest negative residuals occur in the lowest spectral channels, suggesting the possibility of cold absorption over and above the Galactic

column density. In these cases the fit is improved ( $\Delta\chi^2 > 10$ ) when the  $N_H$  is allowed to be a free parameter, the specific values being  $N_H = 3.2 \pm 1.5$  and  $1.7 \pm 0.5 \times 10^{21} \text{ cm}^{-2}$  for Mrk 507 and IRAS 20181-224, respectively. (See also Iwasawa, Brandt & Fabian 1998 for more details on Mrk 507.) In the rest of this chapter it is assumed that Mrk 507 and IRAS 20181-224 are the only NLS1s in the sample with excess cold absorption.

### 2.3.2 The 2–10 keV spectral form

The data below 2 keV, where soft excesses and warm absorbers complicate the spectra, were then ignored in order to characterise better the hard X-ray spectrum of each NLS1. The 2–10 keV spectra were again fitted with a simple power law plus Galactic absorption model but with the addition of a narrow Gaussian emission line ( $\sigma = 0.01$  keV, i.e. narrower than the instrumental resolution) to represent iron  $K_\alpha$  emission in the 6.4–7.0 keV bandpass. Table 2.2 summarises the results.

For nine objects the inclusion of the iron-line component is merited in terms of the resulting improvement in  $\chi^2$  (i.e.  $\Delta\chi^2 > 6.2$ ). Also two further sources show at least a marginal improvement in  $\chi^2$  (see Table 2.2). Acceptable fits were found for most sources, with only three instances of (reduced)  $\chi^2_\nu \geq 1.1$ . The derived photon indices have a mean value of 2.1 with a standard deviation of 0.3. There is some evidence for lines originating from highly ionised iron species (i.e.  $>Fe$  XX and above) in I Zw 1, Ton S180, PKS 0558–504, PG 1244+026 and Ark 564. The measured line equivalent widths range from 100 eV to 600 eV, with large uncertainties. Similarly the constraints on the equivalent width of a (neutral) iron line in those sources lacking a significant line detection are generally rather weak. In general the signal-to-noise was too poor to meaningfully constrain the intrinsic line widths. However, the second observation of NGC 4051 is an exception in that it shows evidence for a broadened iron  $K_\alpha$  line. The best fit parameters for the line are  $E = 6.29 \pm 0.09$  keV, intrinsic width  $\sigma = 0.36^{+0.23}_{-0.15}$  keV and  $EW = 240^{+90}_{-80}$  eV. The improvement in the fit upon adding this broad feature is  $\Delta\chi^2 = 76.8$ . An attempt has been made to fit the line with the relativistic *diskline* profile of Fabian *et al.* (1989), suggesting a mildly ionised line ( $E = 6.6^{+0.1}_{-0.2}$  keV); a near to face-on inclination ( $i < 17^\circ$ ) gives the best fit to the data (assuming values for  $R_{in}$ ,  $R_{out}$  of  $10GM/c^2$ ,  $100GM/c^2$  respectively, and an emissivity law of  $\propto r^{-2}$ ). Guainazzi *et al.* (1986) discuss the spectral fitting of this ASCA observation of NGC 4051 in some detail.

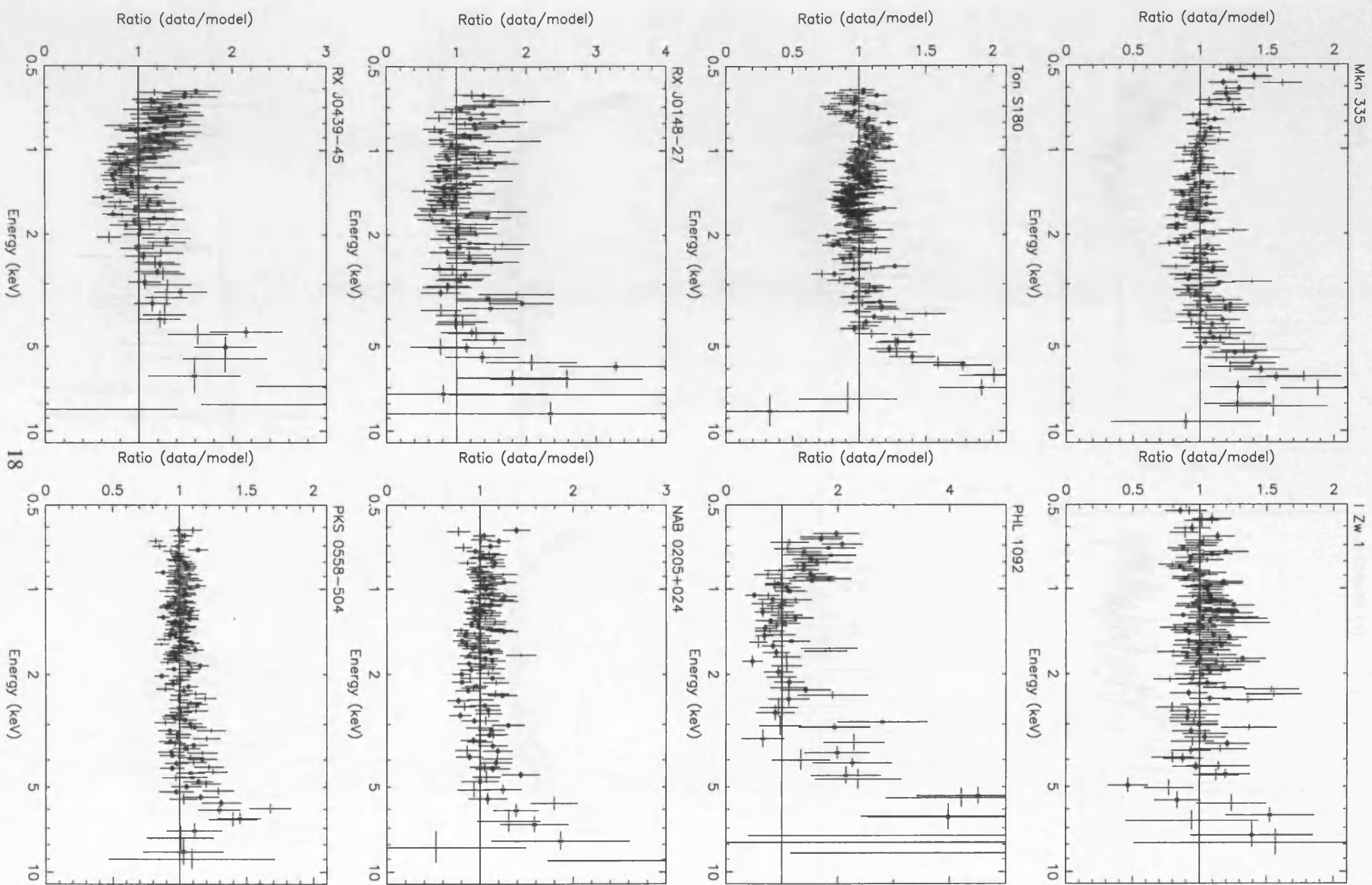


Figure 2.1:

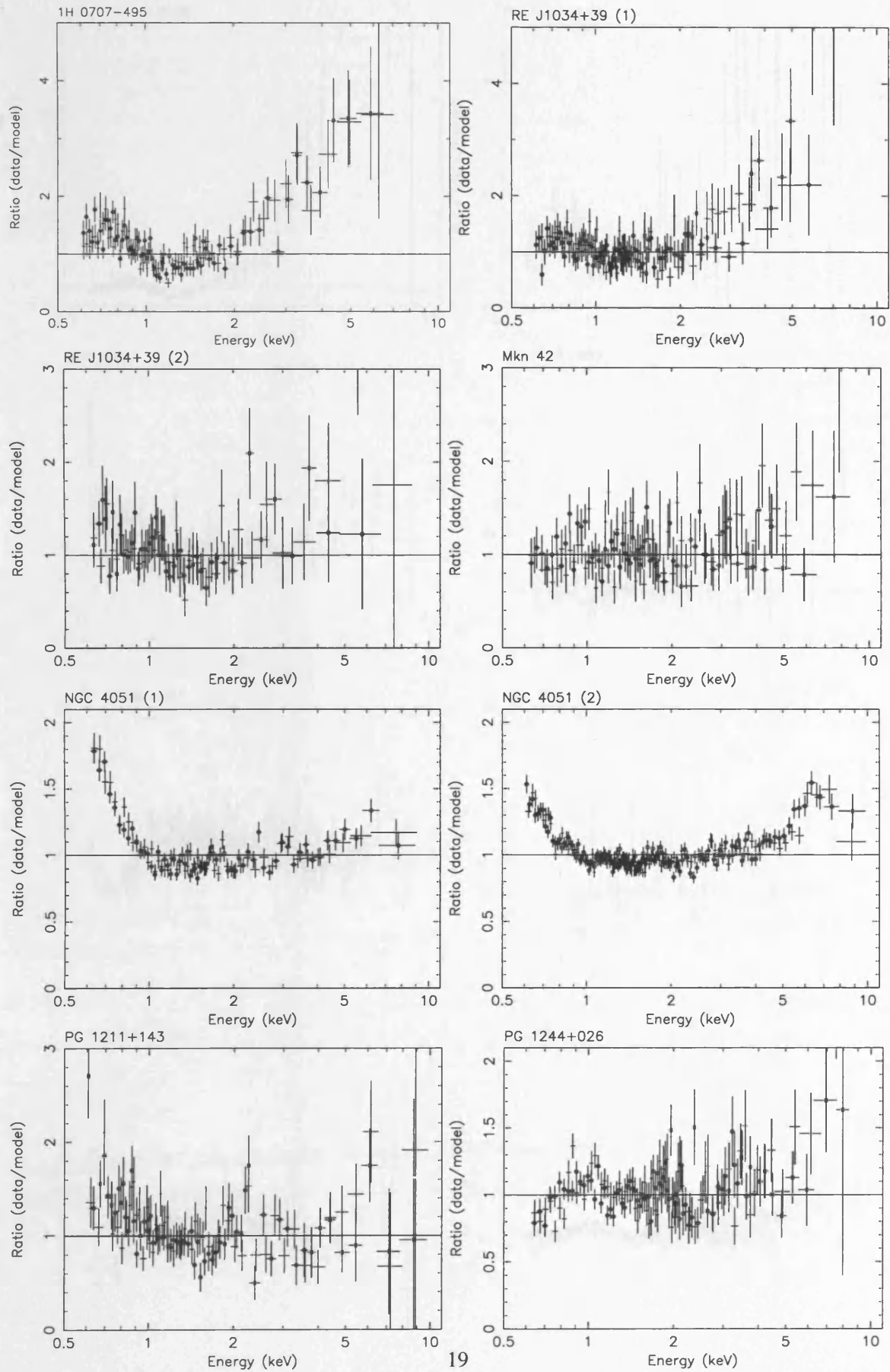


Figure 2.1: cont.

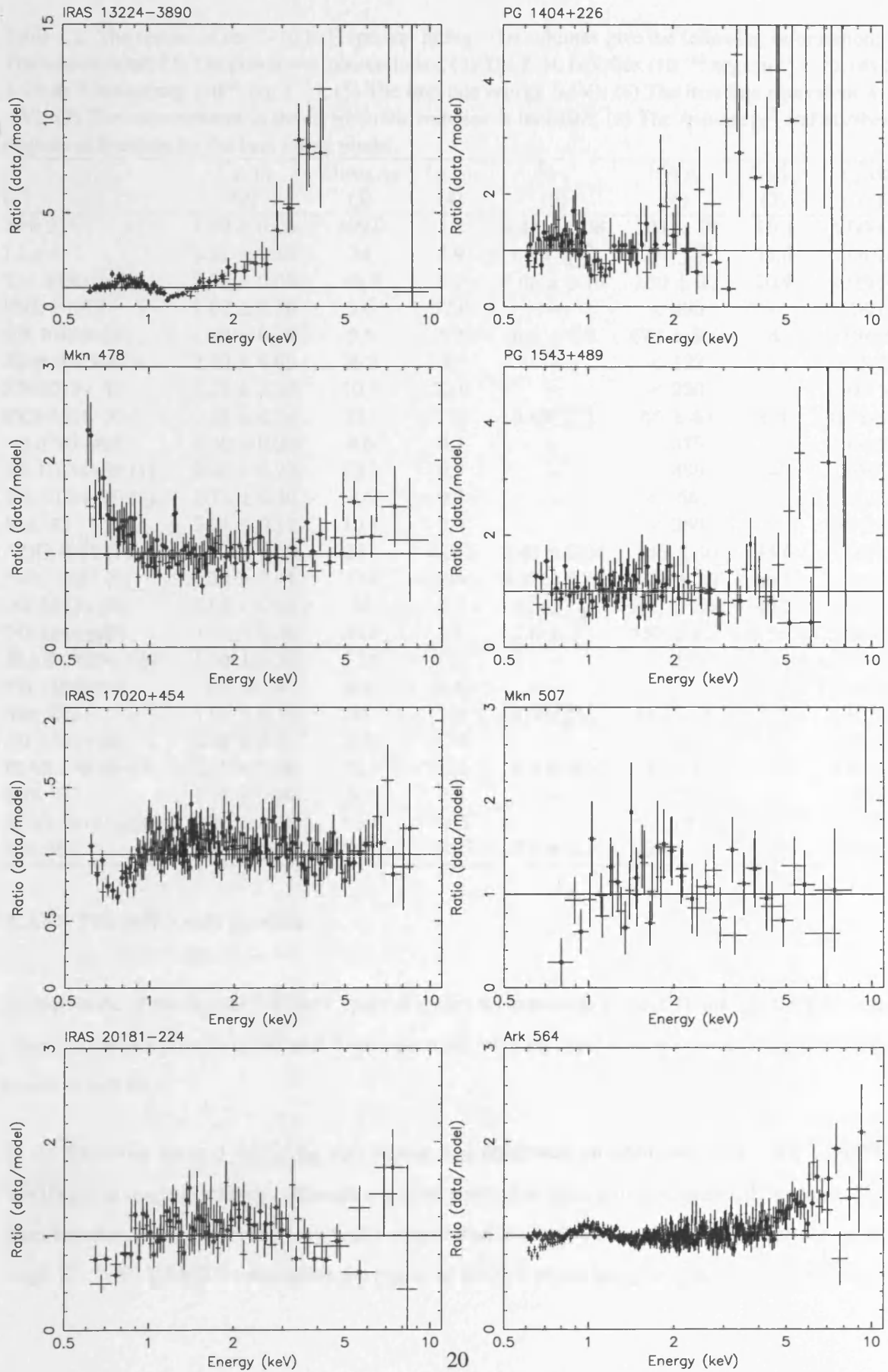


Figure 2.1: The data/model ratio from fits to the 0.6–10.0 keV ASCA spectra using a simple power-law plus Galactic absorption model. Error bars represent one sigma. For clarity only the SIS data are shown, and the SIS-0 data are marked by circles.

Table 2.2: The results of the 2–10 keV spectral fitting. The columns give the following information: (1) The source name; (2) The power-law photon index; (3) The 2–10 keV flux ( $10^{-13}$  erg cm $^{-2}$  s $^{-1}$ ); (4) The 2–10 keV luminosity ( $10^{43}$  erg s $^{-1}$ ); (5) The iron line energy (keV); (6) The iron-line equivalent width (eV); (7) The improvement in the fit when the iron line is included; (8) The *reduced*  $\chi^2$  and number of degrees of freedom for the best fitting model.

(1)	$\Gamma_{2-10}$ (2)	Flux $_{2-10}$ (3)	L $_{2-10}$ (4)	E $_{Fe}$ (5)	EW $_{Fe}$ (6)	$\Delta\chi^2_{Fe}$ (7)	$\chi^2_{\nu}/\text{dof}$ (8)
Mrk 335	$1.89 \pm 0.05$	109.0	3.2	$6.41 \pm 0.08$	$193 \pm 78$	16.3	1.00/458
I Zw 1	$2.27 \pm 0.10$	34	5.9	$6.73^{+0.15}_{-0.30}$	$450^{+250}_{-225}$	11.0	1.04/262
Ton S180	$2.39 \pm 0.05$	45.3	8.3	$6.65 \pm 0.10$	$180 \pm 90$	10.9	1.05/591
PHL 1092	$1.67 \pm 0.30$	3.6	32.0	–	< 490	–	1.18/132
RX J0148–27	$1.99 \pm 0.17$	8.5	5.7	$6.5 \pm 0.2$	$670 \pm 300$	8	0.86/87
NAB 0205+024	$2.10 \pm 0.09$	26.8	30	–	< 122	–	0.85/327
RX J0439–45	$2.25 \pm 0.16$	10.3	22.0	–	< 220	–	1.09/149
PKS 0558–504	$2.25 \pm 0.04$	121	110	$6.65^{+0.35}_{-0.20}$	$65 \pm 40$	6.5	0.98/820
1H 0707–495	$2.40 \pm 0.20$	9.6	0.7	–	< 375	–	1.04/114
RE J1034+39 (1)	$2.46 \pm 0.23$	10.2	0.7	–	< 490	–	1.08/98
RE J1034+39 (2)	$2.73 \pm 0.40$	8.6	0.7	–	< 1560	–	0.97/32
Mrk 42	$2.01 \pm 0.17$	10.5	0.3	–	< 380	–	0.93/122
NGC 4051 (1)	$1.91 \pm 0.03$	291	0.045	$6.43 \pm 0.04$	$145 \pm 40$	35.6	1.00/905
NGC 4051 (2)	$1.84 \pm 0.02$	234	0.040	$6.37 \pm 0.03$	$127 \pm 25$	66.5	1.06/1449
PG 1211+143	$2.03 \pm 0.10$	34	9.7	$6.38^{+0.12}_{-0.20}$	$260 \pm 130$	10.7	0.94/342
PG 1244+026	$2.35 \pm 0.10$	26.8	2.8	$7.0 \pm 0.1$	$460 \pm 210$	11	0.99/255
IRAS 13224–3809	$1.55 \pm 0.22$	5.16	1.0	–	< 290	–	1.12/182
PG 1404+226	$1.6 \pm 0.4$	6.4	2.4	–	< 1220	–	0.84/57
Mrk 478	$1.92 \pm 0.10$	25	7.0	$6.38^{+0.18}_{-0.10}$	$200 \pm 135$	5.7	1.02/216
PG 1543+489	$2.46 \pm 0.32$	4.0	37.2	–	< 350	–	0.87/76
IRAS 17020+454	$2.20 \pm 0.06$	78.4	12.6	$6.5 \pm 0.5$	$95 \pm 70$	5	0.87/577
Mrk 507	$1.61 \pm 0.30$	6.7	9.3	–	< 715	–	1.02/50
IRAS 20181–224	$2.33 \pm 0.12$	10.4	17.5	–	< 120	–	1.14/185
Ark 564	$2.50 \pm 0.03$	205.7	5.2	$7.0 \pm 0.3$	$123 \pm 50$	15	0.99/1171

### 2.3.3 The soft X-ray spectra

Extrapolation of the best-fit 2–10 keV spectral model (as defined in Table 2.2) down to 0.6 keV in most cases results in a poor fit of the soft X-ray spectrum, with the most common residual feature being an excess of soft flux.

In the following spectral fitting the soft excess was fitted with an additional continuum component, specifically a single blackbody, although a second power law often provides an equally good fit. (In the latter case the second power-law is typically steeper than the first by  $\Delta\Gamma \simeq 0.5$  with a break energy in the range 1–2 keV.) Table 2.3 summarises the results of fitting a power law plus blackbody model (note that

from here on the iron line parameters are frozen at the values obtained in the earlier 2–10 keV fits). In all but four objects (I Zw 1, PG 1543+489, Mrk 507 and IRAS 20181–224) a soft excess component provides a significant improvement in the fit, demonstrating that soft excesses are very common to NLS1s. The underlying power-law photon indices given in Table 2.3 have a mean of 2.12 and a standard deviation of 0.26. The fact the mean is very similar to that obtained earlier for 2–10 keV fits demonstrates that the latter fits are relatively immune to the presence of the soft excess.

Nine objects show signs of additional spectral complexity below 2 keV even after the inclusion of the blackbody component in the fit (Table 2.3). Unfortunately, modelling the *ASCA* spectra in terms of additional soft X-ray features is not particularly straightforward. Radiation damage has affected the CCDs in a way which cannot be corrected at present, as a result there is increasing uncertainty in the calibration of the SIS detectors below 1 keV (see 3.3.1). Also since most NLS1 galaxies appear to exhibit a soft X-ray excess it is difficult to distinguish subtleties in the form of the soft continuum from the effects of putative broad emission and/or absorption features.

Recent studies of the X-ray spectra of NLS1s (e.g. Leighly *et al.* 1997b; Fiore *et al.* 1998) have established that in addition to classical warm-absorption features, NLS1s often show anomalous absorption features in the 1–2 keV band. Both types of absorption are spectrally complex and will merit more detailed analysis using the predictions of appropriate photoionisation codes, once high sensitivity X-ray data with good spectral resolution become available from *Chandra* and *XMM-Newton* (e.g. Nicastro, Fiore & Matt 1999). However, a very simplistic approach has been followed here, namely attempting to improve the  $\chi^2$  in the spectral fits for nine sources noted above by including just a *single* absorption feature (in the form of a broad Gaussian absorption line) in the spectral model.

Table 2.4 lists for each of the nine sources the line energy, equivalent width and intrinsic line width obtained when such an absorption feature is added to the power-law plus blackbody continuum model. The line energies are not consistent with a single value but a bifurcation is suggested, namely absorption either in the 0.7–0.9 keV range or in the 1.1–1.4 keV range. Absorption features in the former range are usually interpreted as due to O VII and O VIII edges indicative of the presence of ionised material along the line of sight. Possible origins of the ‘anomalous’ absorption features observed at  $\sim 1.2$  keV have recently been discussed by Leighly *et al.* (1997b) and Fiore *et al.* (1998) (see section 2.4.4).

As noted above the fitting of a Gaussian absorption feature is necessarily an over simplification of the

Table 2.3: The full 0.6–10 keV spectral fits. The columns give the following information: (1) The source name; (2) The power-law photon index; (3) The blackbody temperature (eV); (4) The 0.6–10 keV flux ( $10^{-13}$  erg cm $^{-2}$  s $^{-1}$ ); (5) The derived unabsorbed luminosity ( $10^{43}$  erg s $^{-1}$ ); (6) The ratio of the 0.6–10 keV luminosities of the blackbody and power-law components; (7) The improvement in the fit when the blackbody component is added; (8) The *reduced*  $\chi^2$  and number of degrees of freedom for the best fit model.

Name (1)	$\Gamma$ (2)	kT (3)	Flux $_{0.6-10}$ (4)	$L_{0.6-10}$ (5)	$L_{bb}/L_{pl}$ (6)	$\Delta\chi^2$ (7)	$\chi^2_{\nu}/\text{dof}$ (8)
Mrk 335	$1.96 \pm 0.04$	$160 \pm 14$	191	5.7	0.12	125	1.01/757
I Zw 1	$2.30 \pm 0.03$	$150^f$	72	14.0	< 0.01	–	0.94/594
Ton S180	$2.36 \pm 0.05$	$190 \pm 5$	137	24.7	0.29	226	1.10/988
PHL 1092	$1.67 \pm 0.11$	$162 \pm 15$	7.0	73	0.80	112	1.12/268
RX J0148–27	$2.15 \pm 0.15$	$129^{+32}_{-124}$	18.3	12.7	0.15	12	0.91/230
NAB 0205+024	$2.10 \pm 0.08$	$218 \pm 19$	53	63	0.16	36	0.98/697
RX J0439–45	$2.28 \pm 0.10$	$137 \pm 11$	27.4	81	0.58	152	1.02/379
PKS 0558–504	$2.26 \pm 0.03$	$230 \pm 15$	257	247	0.08	34	1.03/1217
1H 0707–495	$2.33 \pm 0.10$	$107 \pm 4$	39.6	3.7	1.21	429	1.29/338
RE J1034+39 (1)	$2.35 \pm 0.13$	$131 \pm 9$	32.8	2.7	0.64	104	0.95/298
RE J1034+39 (2)	$2.45 \pm 0.20$	$142 \pm 20$	33.6	2.8	0.49	23	0.78/125
Mrk 42	$1.89^{+0.17}_{-0.09}$	$227 \pm 40$	20.6	0.53	0.15	8	0.99/271
NGC 4051 (1)	$1.97 \pm 0.02$	$86 \pm 5$	561	0.10	0.22	824	1.04/1205
NGC 4051 (2)	$1.94 \pm 0.01$	$106 \pm 5$	402	0.07	0.11	1160	1.13/1846
PG 1211+143	$2.07 \pm 0.06$	$110 \pm 12$	72	23.0	0.17	57	0.95/713
PG 1244+026	$2.31 \pm 0.08$	$210 \pm 10$	75	8.1	0.26	64	1.17/535
IRAS 13224–3809	$1.60 \pm 0.13$	$119 \pm 4$	18	4.7	2.1	537	1.28/426
PG 1404+226	$1.87 \pm 0.20$	$115 \pm 7$	12.9	9.1	1.9	177	1.20/167
Mrk 478	$1.96 \pm 0.05$	$89 \pm 12$	50	14.5	0.23	101	1.03/495
PG 1543+489	$2.48 \pm 0.20$	$436 \pm 436$	10.7	105	0.04	1	0.91/206
IRAS 17020+454	$2.21 \pm 0.05$	$260 \pm 36$	148	29	0.05	9	1.06/972
Mrk 507	$1.74 \pm 0.24$	$150^f$	8.6	1.5	< 0.08	–	0.96/97
IRAS 20181–224	$2.33 \pm 0.11$	$258^{+62}_{-79}$	19.3	47.4	0.08	3	1.15/389
Ark 564	$2.44 \pm 0.03$	$195 \pm 4$	568	16.7	0.21	558	1.27/1567

<sup>f</sup> Parameter has been fixed in the fit.

Table 2.4: X-ray spectral fitting of a Gaussian absorption line. The columns give the following information: (1) The source name; (2) The best fit line energy (keV); (3) The line equivalent width (eV); (4) The intrinsic line width (keV); (5) The improvement in the fit when the absorption feature is included (compared to Table 2.3).

Name (1)	Energy (2)	EW (3)	$\sigma$ (4)	$\Delta\chi^2$ (5)
Ton S180	$1.22^{+0.07}_{-0.04}$	$-95 \pm 16$	$0.31 \pm 0.04$	20
1H 0707-495	$1.08 \pm 0.03$	$-112^{+25}_{-38}$	$0.14 \pm 0.07$	32
NGC 4051	$0.83 \pm 0.03$	$-33^{+4}_{-21}$	$0.15^{+0.15}_{-0.02}$	43
PG 1244+026	$1.31^{+0.07}_{-0.03}$	$-108 \pm 50$	$0.24 \pm 0.08$	24
IRAS 13224-38	$1.10 \pm 0.07$	$-275^{+120}_{-160}$	$0.24^{+0.06}_{-0.03}$	87
PG 1404+226	$1.16 \pm 0.05$	$-100 \pm 30$	$0.09 \pm 0.02$	31
IRAS 17020+45	$0.70^{+0.05}_{-0.02}$	$-129^{+25}_{-35}$	$0.12 \pm 0.05$	64
IRAS 20181-22	$0.90 \pm 0.03$	$-42^{+61}_{-24}$	$< 1.6$	8
Ark 564	$1.38 \pm 0.03$	$-55^{+24}_{-10}$	$0.19^{+0.11}_{-0.03}$	132

true picture. In order to investigate the individual sources in somewhat more detail the spectra of the nine objects listed in Table 2.4 have been refitted including a variety of additional absorption and emission components. For example, one or two absorption edges, a single Gaussian emission line or a meka1-type optically-thin thermal plasma (Kaastra & Mewe 1993) have been tested. (Of course the modelling of the underlying soft excess changes substantially between these cases so as to maintain the match to the observed spectrum in the 0.6–2 keV bandpass). The outcome was that in five of the nine objects an absorption component gave a significantly better fit than an emission component. They are: 1H 0707–495, NGC 4051, IRAS 13224–3809, PG 1404+226 and IRAS 17020+454. Unfortunately the situation is more ambiguous in the remaining four cases (Ton S180, PG 1244+026, IRAS 20181–224 and Ark 564) since absorption and emission models can be constructed which give comparable fits to the *ASCA* data. Further comments on the spectral fitting of the individual sources are given in § 2.6.

## 2.4 Discussion

### 2.4.1 The hard X-ray continua of NLS1s

Using spectral measurements compiled from the published literature, Brandt, Mathur & Elvis (1997) identified a correlation between the hard power-law spectral index and the width of the optical  $H\beta$  line in a sample of Seyfert 1 galaxies, in the sense that NLS1s tend to have somewhat steeper hard X-ray spectra than normal broad-line objects. Fig. 5.4 shows a plot of power-law photon index (from Table 2.3) against

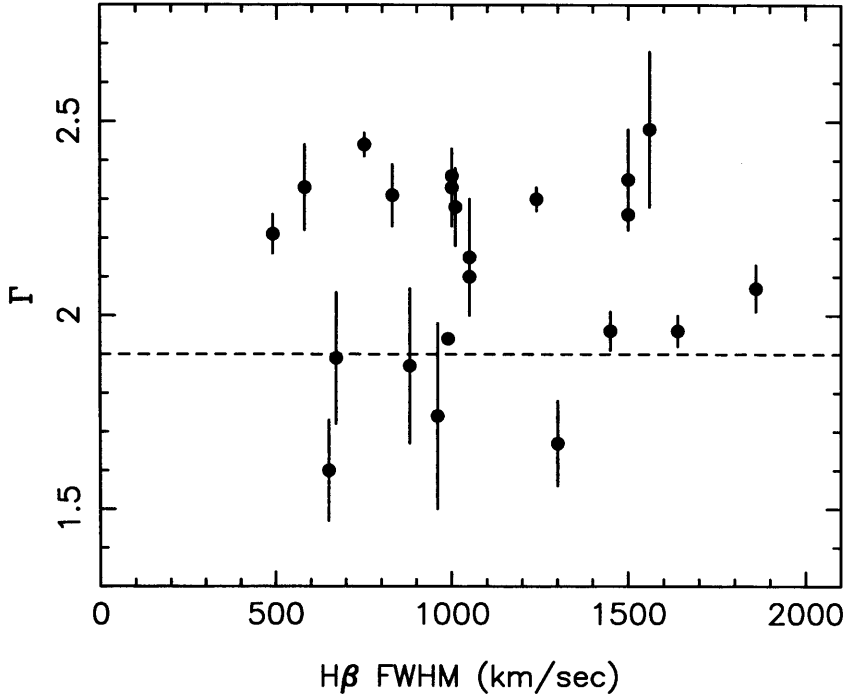


Figure 2.2: The photon index of the hard continuum plotted against the  $H\beta$  line width for the NLS1 sources in the *ASCA* sample. The dotted line represents the mean spectral index of the BLS1 sample of Nandra *et al.* (1997b).

the  $H\beta$  FWHM for the current sample. Clearly within the restricted range of line width that defines the NLS1 subclass (i.e.  $H\beta$  FWHM  $\leq 2000$  km s $^{-1}$ ) there is no hint of a correlation. As noted earlier the mean photon index of the sample of NLS1s is  $\Gamma = 2.12$ , with a standard deviation of  $\sigma=0.26$ . Nandra *et al.* (1997b) tabulate the 3–10 keV spectral slopes for 15 BLS1s (i.e. excluding the 2 NLS1s in their sample) based on *ASCA* measurements; these give an average slope of  $\Gamma = 1.9$  with a standard deviation of  $\sigma = 0.17$ . (Nandra *et al.* (1997b) include a reflection component in their analysis, which can have the effect of increasing the derived power-law spectral indices by up to  $\Delta\Gamma \simeq 0.2$ . The spectra presented here are generally too faint at high energies to warrant the inclusion of a reflection component.) Thus a modest trend in  $\Gamma$  over a broad range of  $H\beta$  line width is suggested, consistent with the Brandt, Mathur & Elvis (1997) result. However, the spectral steepening is a fairly subtle effect and the above comparison may not be entirely free of selection bias. For example, one could argue that the comparison is of a hard X-ray selected sample with one largely selected at soft X-rays (but see the discussion in Brandt, Mathur & Elvis 1997).

### 2.4.2 The soft X-ray excess

In the present analysis this component was fitted in terms of a single temperature blackbody, which should be a reasonable assumption, given the restricted *ASCA* bandpass, if the emission resembles that expected from an accretion disc (e.g. Ross, Fabian & Mineshige 1992). Indeed, the addition of a blackbody component significantly improves the fit (at the  $> 99\%$  confidence level) in 18 out of 22 objects. This is a much higher rate of incidence of soft excesses than appears to be the case for BLS1 samples (e.g. Turner & Pounds 1989; Reynolds 1997). These represent genuine soft excess *emission* – an extrapolation of the 2–10 keV continuum down to softer energies shows clear excess flux – as opposed to an apparent steepening of the soft X-ray spectrum compared to the hard X-ray spectrum due to e.g. the presence of a warm absorber.

The soft excess also appears to contain a significant amount of the X-ray luminosity of these NLS1s; it generally dominates over the hard power law at energies  $\lesssim 1.5$  keV, and presumably peaks in the extreme ultraviolet. Even in the limited *ASCA* bandpass the luminosity of the soft excess is comparable to that of the hard power law and in three objects (1H 0707–495, IRAS 13224–3809 and PG 1404+226), the blackbody component contains more luminosity than the power law in the 0.6–10 keV range, i.e.,  $L_{bb}/L_{pl} \geq 1$  (see Table 2.3). For these three sources, extrapolation of the continuum spectrum down to 0.15 keV and up to 100 keV still leaves this ratio above unity. (Note for these three objects the soft excess is dominant even after the inclusion of additional spectral features; see § 2.6). With spectral coverage over wider bandpass than *ASCA*, many more of these NLS1 spectra would appear to be dominated by the soft excess (RE J1034+396 is one such example; see Pounds, Done & Osborne 1995). The implication is that, at least in some NLS1s, the soft excess cannot be solely due to reprocessing of the hard X-ray continuum (as might be the case in Ark 564; see 3.6).

Two objects with strong soft excesses, namely PHL 1092 and IRAS 13224–3809, appear to have particularly hard underlying X-ray continua ( $\Gamma = 1.6 - 1.7$ , see Table 2.3 and also Otani, Kii & Miya 1996). This could be used as an argument against models where the soft photons Compton scatter against the hot electrons in an accretion disc corona to produce the underlying X-ray hard spectrum. However, an alternative view might be that the relatively flat 2–10 keV spectra are the result of strong reflection in these objects (any iron K emission is only poorly constrained in these objects). Sensitive broad-band X-ray spectral measurements (extending well above the Compton peak) would help distinguish between these two descriptions.

### 2.4.3 Iron $K_{\alpha}$ emission

Emission lines at 6–7 keV are detected at modest significance in nine objects, and with marginal significance in 2 others. However, as noted earlier the line properties (energy, equivalent width, intrinsic width) are in general only poorly constrained by the *ASCA* spectra. A point of interest, for follow-up when more sensitive X-ray spectra are available, is the incidence of emission lines from highly ionised gas (corresponding to Fe XX and above) in NLS1s, suggested by the current data.

### 2.4.4 Soft X-ray spectral features

The residuals to the best fitting continuum models show unusual features below 2 keV in nine objects. In three sources (NGC 4051, IRAS 17020+454 and IRAS 20181–224) these are probably due to O VII and O VIII edges at 0.74 and 0.87 keV respectively, indicative of the presence of warm absorbing gas along the line of sight to the nuclear continuum source. Of the other six objects, three (1H 0707–495, IRAS 13224–3809 and PG 1404+226) are most likely affected by absorption, whereas for the others (Ton S180, PG 1244+026 and Ark 564) the interpretation is more ambiguous (see § 2.6 and 3.6). However, for the purpose of the present discussion the assumption discussed earlier, namely that all six sources exhibit anomalous absorption in the range 1.1–1.4 keV, is adopted.

Leighly *et al.* (1997b) have reported the detection of the same anomalous absorption features in three sources and discussed possible physical origins of the effect. Specifically these authors note that in order to identify the absorption with either an O VII and/or an O VIII edge, as predicted in the warm absorber scenario, then very significant (i.e. relativistic) outflow velocities would be required in order to achieve the necessary blueshifting of the edge energies. An alternative model has been suggested by Nicastro, Fiore & Matt (1999) who invoke resonant absorption lines in a warm absorber to explain the absorption evident in the spectrum of IRAS 13224–3809, in which case there is no requirement for relativistic outflow. The basis of their model is that a steep soft X-ray spectrum can produce a different ionisation structure in the warm absorber, with carbon and oxygen fully stripped. Absorption is then produced by a complex of strong absorption lines around 1–2 keV, made up of mainly iron L resonance lines (see Fig. 4 of Nicastro, Fiore & Matt 1999). These lines would appear as negative residuals in the low-resolution *ASCA* spectra. The total equivalent widths of these lines can be  $\sim 100$  eV, consistent the results of Table. 2.4, although of course the assumption of a Gaussian absorption profile is in this case

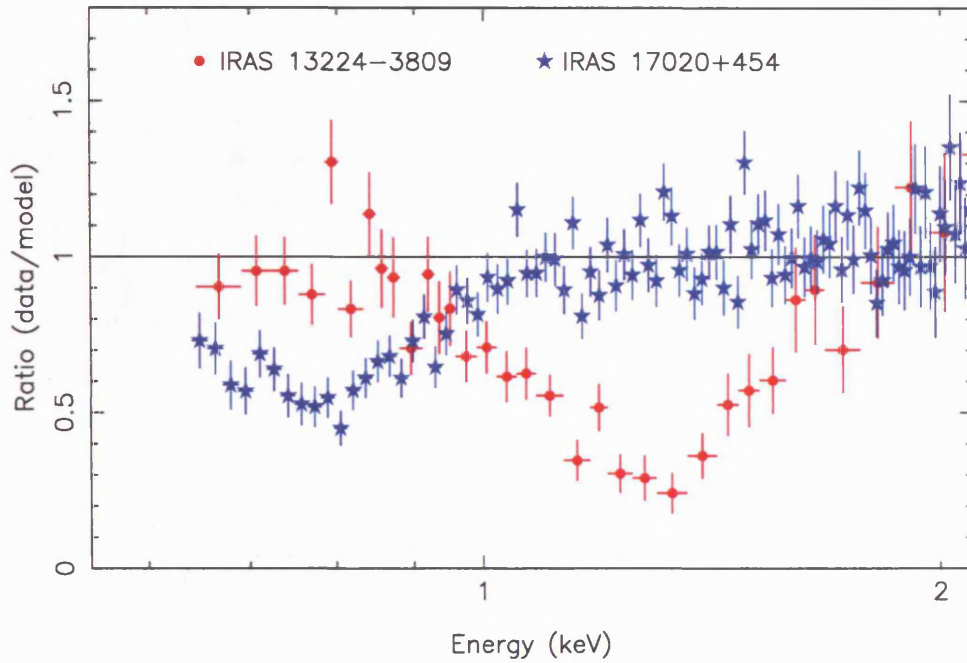


Figure 2.3: The ratio of the *ASCA* data to the best-fit continuum model for two sources, IRAS 13224–3809 (filled circles) and IRAS 17020+454 (open squares). The former source exhibits an anomalous absorption feature near 1.2 keV and the latter probably a warm (O VII) edge near 0.74 keV. Both spectra have been shifted into the source rest frame and for clarity only SIS-0 data are shown.

an extremely crude approximation to the true spectral form.

One requirement of the Nicastro, Fiore & Matt (1999) model is that the absorbing gas has to have a turbulence velocity  $\gtrsim 100 \text{ km s}^{-1}$  in order for the equivalent widths of the absorption lines to be large enough to explain the observed absorption. This is consistent with current measurements of absorption line profiles in the ultraviolet. As discussed in Reynolds & Fabian (1995), a steep X-ray spectrum will make the warm absorber more stable (against runaway heating) at high ionisation than a flat spectrum, due to the effects of Compton cooling within the warm gas. This may allow the warm absorber to remain stable at the higher values of ionisation parameter needed in the Nicastro, Fiore & Matt (1999) model.

On the basis of the above arguments, it is at least plausible that both the 0.7–0.9 keV and the 1.1–1.4 keV absorption arises due to the presence of highly ionised gas along the line of sight to the nuclear X-ray source. Interestingly the two different types of soft X-ray features (described earlier as ‘warm absorbers’ and ‘anomalous’) occupy different regions of parameter space as shown in Fig. 2.4, which shows the ratio of the luminosities of the soft excess to the hard power law components ( $L_{bb}/L_{pl}$ ) versus the  $H\beta$  line width. The sources with anomalous features tend to have relatively high  $L_{bb}/L_{pl}$  values whereas the three

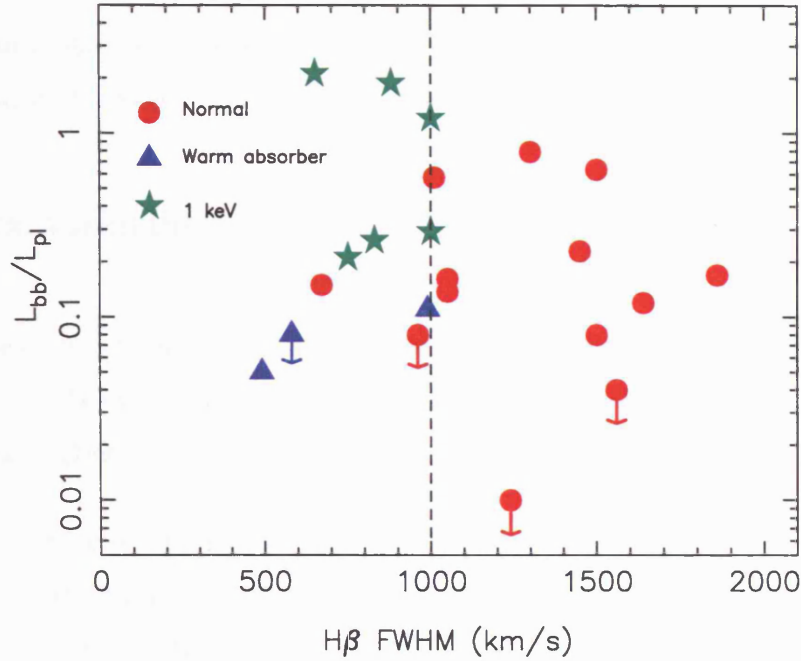


Figure 2.4: The relative luminosity of the soft excess compared to the hard power law (as given in Table 2.3) versus the H $\beta$  line width. Objects with no evidence for absorption are marked by circles and those with normal warm absorbers by crosses. The sources exhibiting anomalous 1.1–1.4 keV absorption are marked by stars. The arrows indicate upper limits on the strength of the soft excess.

sources exhibiting ‘normal’ warm absorption are found at the low end of this range. This is circumstantial evidence in support of the Nicastro, Fiore & Matt (1999) model, in that they require a strong contribution from the soft excess in order to produce the necessary conditions for the dominance of resonance over pure photoelectric absorption. This is given further weight if BLS1s are also considered, as over 50% of such sources show signs of absorption in the range 0.7–0.9 keV, most likely due to oxygen edges, but relatively few possess conspicuous soft excesses, at least in the ASCA bandpass (e.g., Reynolds 1997; George *et al.* 1998). Some alternatives for  $\sim 1.2$  keV absorption, also not requiring relativistic outflows, are discussed in Komossa & Fink (1998).

A further interesting result illustrated by Fig. 2.4 is that all but one of the NLS1s with H $\beta$  FWHM  $\leq 1000$  km s $^{-1}$  show evidence for some sort of absorption, either by ionised material or (as in one case) by neutral gas. Conversely none of the NLS1s with H $\beta$  FWHM  $> 1000$  km s $^{-1}$  exhibit signs of line-of-sight absorption. One possibility is that this represents a very sharply tuned geometry dependence. For example, if the absorbing material originates in an outflow from the disc, it would only be seen in low inclination systems (for a discussion of the ‘pole-on’ model for NLS1s, see Boller, Brandt & Fink (1996) and references therein). It is unclear, however, why such a tight upper limit should apply to the H $\beta$  line

width in such circumstances. Clearly further study of this effect using both a larger sample of NLS1s and more sophisticated modelling of the putative absorption features is merited.

## 2.5 Spectral variability

The data considered thus far have been time-average spectra. For completeness the spectral variability properties of the NLS1s are briefly discussed here. More thorough analyses can be found in Turner *et al.* (1999b) and Leighly (1999).

The background subtracted, full-band (0.5–10 keV) light curves are shown in Fig. 2.5. The data are shown binned on two time-scales. The thin red lines denote the extracted 128 s bins with errors calculated based on counting statistics. The thick black lines show the data rebinned on *ASCA*'s orbital period (5760 s) with errors calculated based on the error of the mean (eqn. 4.14 of Bevington & Robinson 1992). It is clear from these light curves that most NLS1s show strong variability on these timescales, although it is only for the brighter sources that significant variability can be seen on 128 s time-scales (e.g. NGC 4051).

As a check of the possible impact of spectral variability on the time-averaged source spectra, the 2–10 keV and 0.5–2 keV light curves of each source (average of SIS-0 and SIS-1) were extracted. The constancy of the spectral hardness (defined as ratio of the 2–10 keV count rate to the 0.5–2 keV count rate) during the observation was checked using a  $\chi^2$  test. Five out of 22 sources gave unacceptable values of  $\chi^2$  at the 95% level (NAB 0205+024, RX J0439–45, NGC 4051, Mrk 478, Ark 564) indicative of underlying spectral variability. The signal/noise is too low in the highly variable NLS1s, such as IRAS 13224-3809 (which is faint above 2 keV), to reliably detect spectral variability. It is assumed that the observation-averaged spectra provide a good representation of the source properties, at least in the case of the 17 sources without significant spectral variability. The properties of the sample as a whole are not effected by excluding the 5 sources showing spectral variability. The implicit assumption of the previous spectral analysis, namely that the properties of the sample of NLS1s are not biased by the effects of spectral variability, is therefore a reasonable one.

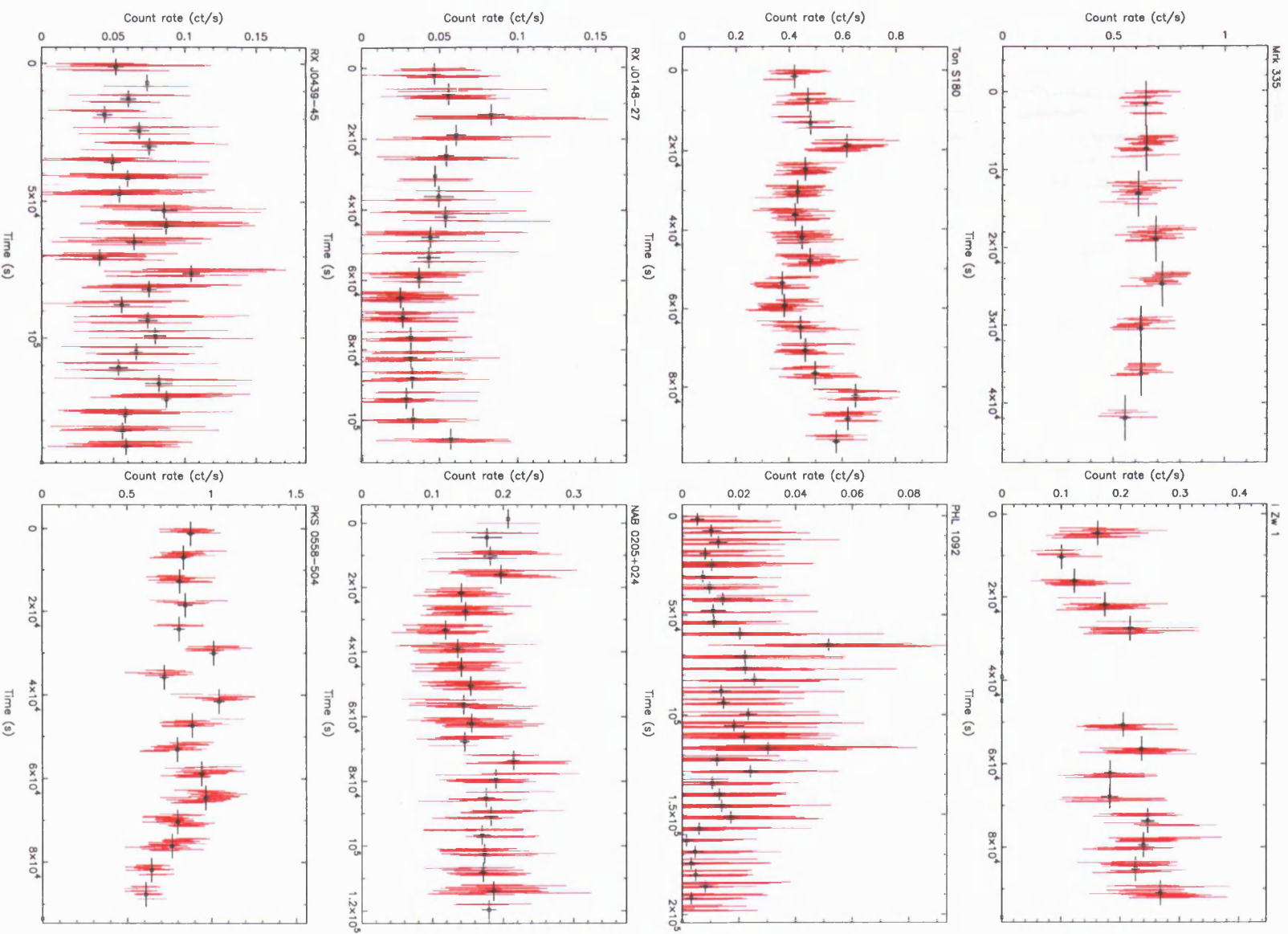


Figure 2.5:

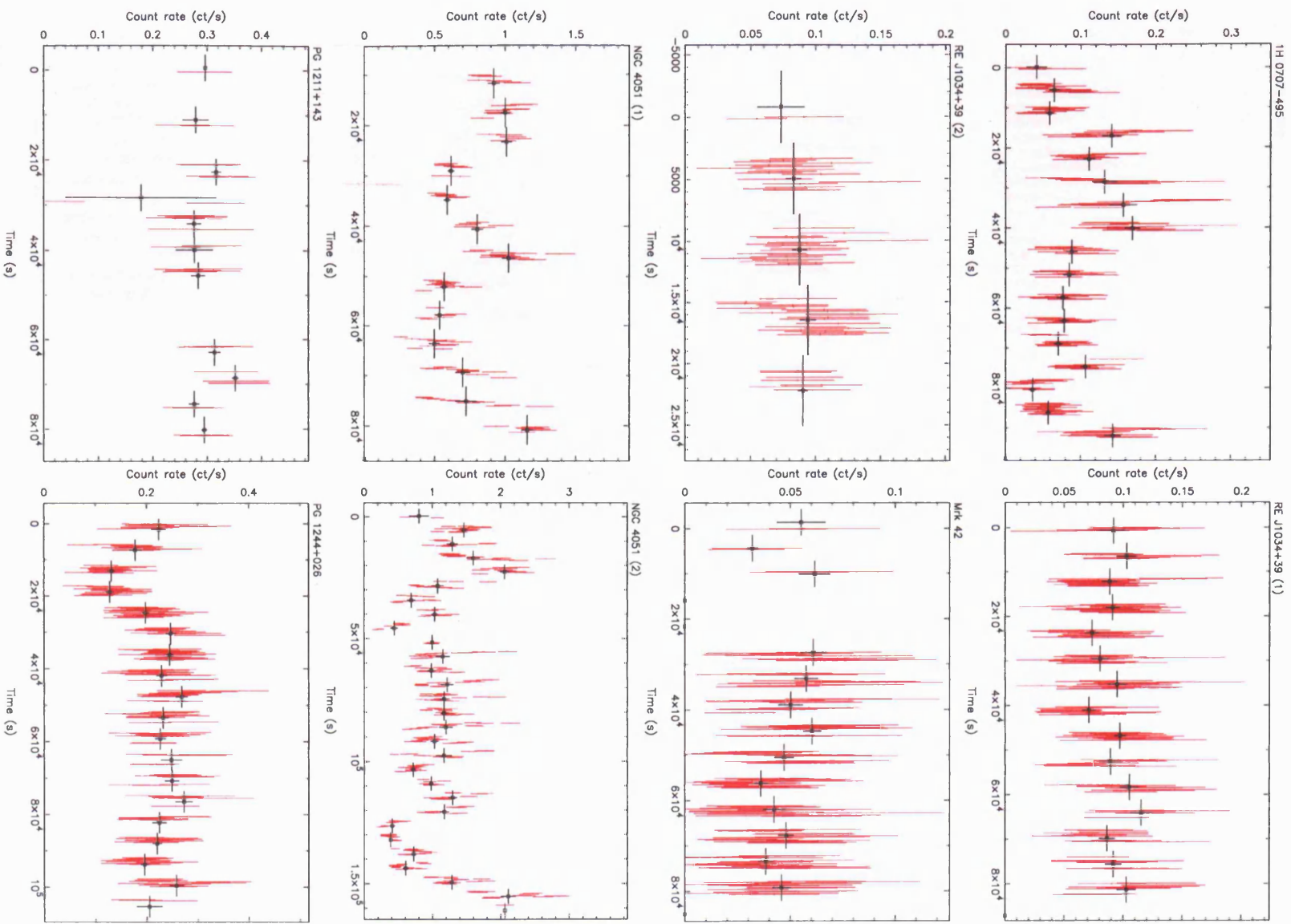


Figure 2.5: cont.

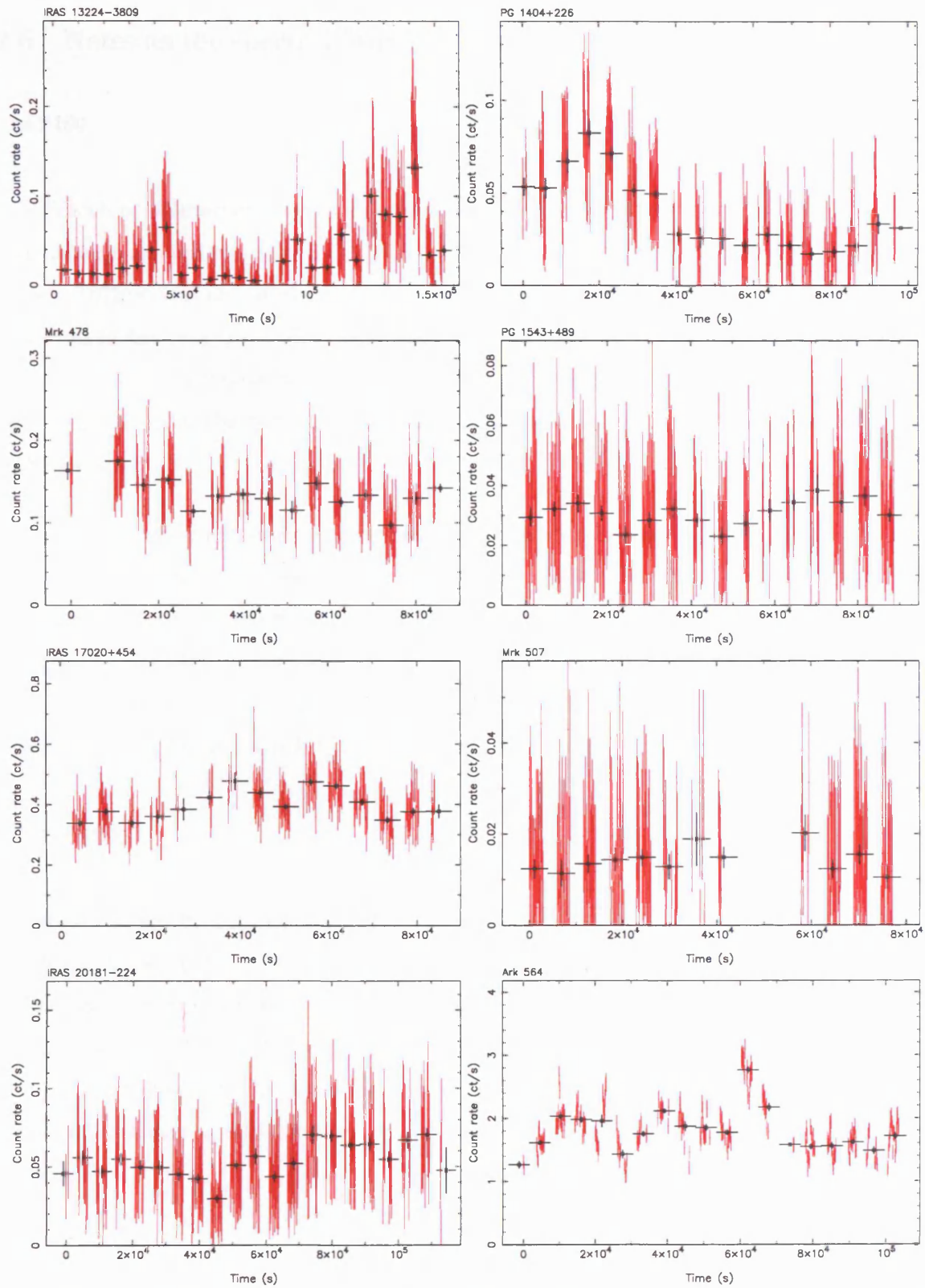


Figure 2.5: Light curves for all 24 observations of the NLS1s. These are the average of the two SIS instruments over the full 0.5–10 keV band. Red lines denote 128 s bins, while thick black lines mark the orbital averages.

## 2.6 Notes on the spectral fitting of individual objects

### Ton S180

It is difficult to differentiate between absorption and emission at  $\sim 1.2$  keV in Ton S180. A single absorption edge at a rest energy of  $E = 1.09 \pm 0.03$  keV with an optical depth  $\tau = 0.17 \pm 0.03$ , yields  $\chi^2/\nu = 1072/986$ . A second edge in the spectrum (at  $E = 1.42 \pm 0.06$  keV with  $\tau = 0.13 \pm 0.03$ ) improves the fit further ( $\chi^2/\nu = 1059/985$ ). There is some evidence for an additional edge at  $\sim 0.73$  keV ( $\chi^2/\nu = 1048/983$ ) presumably corresponding to O VII. However SIS-1 seems to underestimate the flux compared to SIS-0 below 0.8 keV, so any features in the spectrum below 0.8 keV need to be considered with caution.

A significant improvement over the soft excess fit is given when a broad Gaussian emission component is added to the model near 1 keV. The best-fit parameters are line EW =  $20 \pm 8$  eV, energy  $E = 0.94 \pm 0.03$  keV and intrinsic width  $\sigma = 0.062 \pm 0.025$  keV, for which  $\chi^2/\nu = 1055/985$ . A `mekal` model also gives an acceptable fit to the data, yielding a plasma temperature of  $kT = 0.89 \pm 0.11$  keV ( $\chi^2/\nu = 1050/986$ ). Turner, George & Nandra (1998) find similar results in their analysis of these data for Ton S180, except that they do not include a soft excess in their fits.

### 1H 0707-495

An absorption feature definitely gives the best fit in 1H 0707-495. A broad absorption line improves the fit significantly ( $\chi^2/\nu = 404/335$ ), as per Table 2.4. An equally good  $\chi^2$  can be obtained, but for 1 additional free parameter, using two edges instead of a single Gaussian; the first edge is at  $E = 1.09 \pm 0.03$  keV with  $\tau = 0.63 \pm 0.27$  and the second at  $E = 0.90 \pm 0.03$  keV with  $\tau = 0.5 \pm 0.2$ . Leighly *et al.* (1997b) also find evidence for one or more absorption features near 1 keV. The addition of a Gaussian emission line in the range 0.6–3 keV, instead of an absorption feature, does not provide any improvement in the fit.

## NGC 4051

Previous investigations of the X-ray spectrum of NGC 4051 have suggested the existence of a warm absorber. There is no evidence for additional spectral features in the first observation (taken during the PV phase of the mission) but the second (AO2) observation, which has much better signal-to-noise, does show significant features in the residuals between 0.7 and 0.9 keV. In this case the apparent warm absorber has been fitted with 2 absorption edges, for the first edge  $E = 0.73 \pm 0.02$  keV and  $\tau = 0.33 \pm 0.05$ , for the second edge  $E = 0.93 \pm 0.03$  keV and  $\tau = 0.19 \pm 0.04$ . The resulting fit statistic is  $\chi^2/\nu = 2010/1842$ , an improvement of  $\Delta\chi^2 = 77$  over the model without absorption. The results suggest a normal warm absorber in NGC 4051, with the edges probably originating from O VII and O VIII. These results are broadly consistent with those of Guainazzi *et al.* (1986), who consider the fitting of this observation in much greater detail.

## PG 1244+026

Emission and absorption components give comparable fits in PG 1244+026. The addition of a broad Gaussian absorption line significantly improves the fit ( $\chi^2/\nu = 601/532$ ), as per Table 2.4. A single edge at an energy of  $E = 1.18 \pm 0.03$  keV, gives a better fit ( $\chi^2/\nu = 591/533$ ). Adding another edge further improves the fit; with two edges (at  $E = 1.16 \pm 0.04$  keV and  $E = 0.63^{+0.04}_{-0.45}$  keV) the fit obtained is  $\chi^2/\nu = 583/531$ .

A broad Gaussian emission line at an energy of  $E = 0.97 \pm 0.04$  keV also significantly improves the fit ( $\chi^2/\nu = 589/532$ ), with an equivalent width of  $EW = 36 \pm 11$  eV. A slightly better fit ( $\chi^2/\nu = 586/533$ ) is obtained with the `mekal` model, with a plasma temperature of  $kT = 1.0 \pm 0.1$  keV. Fiore *et al.* (1998) also find evidence for either an absorption feature at  $\sim 1.2$  keV or an emission feature at 0.9 keV.

## IRAS 13224-3809

Absorption components give a slightly better fit than emission components. The addition of a single absorption edge to the model improves the fit significantly ( $\chi^2/\nu = 478/424$ ). The best fit edge energy is  $E = 1.11 \pm 0.04$  keV. A second edge improves the fit further ( $\chi^2/\nu = 467/422$ ), with edge energies at  $E = 1.00 \pm 0.04$  and  $1.18 \pm 0.03$  keV and optical depths of  $\tau = 0.73$  and 1.15 respectively. This fit

also alters the continuum parameters slightly:  $\Gamma = 1.84 \pm 0.07$  and  $kT=163 \pm 9$  eV. A broad Gaussian absorption line gives a slightly better fit ( $\chi^2/\nu = 459/423$ ), with parameters as in Table 2.4.

A broad Gaussian emission line at  $0.74 \pm 0.05$  keV gives a slightly worse fit ( $\chi^2/\nu = 470/423$ ), as does the `mekal` model ( $\chi^2/\nu = 480/424$ ) with a plasma temperature of  $kT=0.63 \pm 0.05$  keV. These results are broadly consistent with those of Leighly *et al.* (1997b) and Otani, Kii & Miya (1996).

### PG 1404+226

Significant evidence is found for an absorption feature in PG 1404+226. The addition of a single edge to the best-fitting continuum model (PL+BB) yields  $\chi^2/\nu = 172/165$ , an improvement of  $\Delta\chi^2 = 29$ , with an edge energy of  $E= 1.07 \pm 0.03$  keV and optical depth  $\tau = 0.84 \pm 0.28$ , consistent with the results of Leighly *et al.* (1997b). A slight improvement ( $\Delta\chi^2 = 8.1$ ) is also achieved by adding a second edge, although the edge energy of  $E= 2.4 \pm 0.3$  keV seems rather high. The 1 keV feature can also be modelled with a broad Gaussian absorption line, giving  $\chi^2/\nu = 170/164$  with fit parameters as in Table 2.4. George *et al.* (2000) model the soft X-ray spectrum with a broad Gaussian line representing the soft excess, and find no need for an additional emission/absorption component.

### IRAS 17020+454

The residuals from a simple power law plus Galactic absorption fit show clear signs of absorption in IRAS 17020+454 (see Fig. 2.1). The addition of an edge at an energy of  $E=0.71 \pm 0.02$  keV with a depth  $\tau = 0.91 \pm 0.22$ , improves the fit significantly ( $\chi^2/\nu = 979/971$ ). A second edge at  $E=1.15 \pm 0.04$  keV with a depth  $\tau = 0.20 \pm 0.08$  further improves the fit ( $\chi^2/\nu = 965/969$ ). A broad Gaussian absorption line gives a comparable fit as detailed in Table 2.4.

A narrow Gaussian emission line at an energy of  $E=1.06 \pm 0.02$  with an equivalent width of  $EW=23_{-7}^{+5}$  eV gives a worse fit than an absorption line ( $\chi^2/\nu = 1006/971$ ). However, the inclusion of an edge at  $0.72 \pm 0.02$  keV, as well as the emission line, does lead to a net improvement in the fit ( $\chi^2/\nu = 962/969$ ).

This is in broad agreement with Leighly *et al.* (1997a), who identify the 0.7 keV feature with an absorption edge from O VII. Komossa & Bade (1999a) present a *ROSAT* spectrum of IRAS 17020+454 and also find evidence for a warm absorber, albeit a dusty one.

## **IRAS 20181-224**

There may be an emission or absorption feature in the spectrum of IRAS 20181-224, but the improvement in the fit upon adding either is rather small. A broad absorption line gives a slight improvement in the fit, as noted in Table 2.4, but adding one or two edges in the range 0.6–3 keV gives a significantly worse fit.

A narrow Gaussian emission line at  $1.11 \pm 0.05$  keV also slightly improves the fit ( $\chi^2/\nu = 438/387$ ). The `mekal` model gives a similar result with a plasma temperature of  $kT=1.7^{+0.6}_{-0.3}$  keV. Halpern & Moran (1998) give a more detailed discussion of this object.

## **Ark 564**

The broad Gaussian absorption line model detailed in Table 2.4 is clearly not the best representation of the data ( $\chi^2/\nu = 1854/1564$ ). A more detailed discussion of the X-ray properties of Ark 564 is given in Chapter 3.

## Chapter 3

# X-ray Properties of Arakelian 564

### 3.1 Overview

Simultaneous *ASCA* and *RXTE* observations of Ark 564, the brightest known NLS1 in the 2–10 keV band, are presented. The X-ray spectrum is complex and the observed features are well described in terms of an ionised accretion disc. The chapter is organised as follows. The observations are described in Section 3.3 and the spectral fitting is detailed in Section 3.4. The variability properties of Ark 564 are given in Section 3.5, followed by conclusions in Section 3.6.

### 3.2 Arakelian 564

Arakelian 546 (aka MCG +05-53-012) is a narrow-line Seyfert 1 with an  $H\beta$  FWHM  $\sim 750$  km s<sup>-1</sup> at a redshift of  $z = 0.024$ . Figure 3.1 shows the optical spectrum of Ark 564 obtained using the Kast spectrograph on the Shane 3m (see Chapter 5). *ROSAT* data revealed a complex soft X-ray spectrum in Ark 564, well fitted with either a power law and strong soft excess, or a (steeper) power law and an absorption edge at 1.2 keV (Brandt *et al.* 1994). Ark 564 was exceptional in the sample of Walter & Fink (1993) for having usually weak ultraviolet compared to soft X-ray emission.

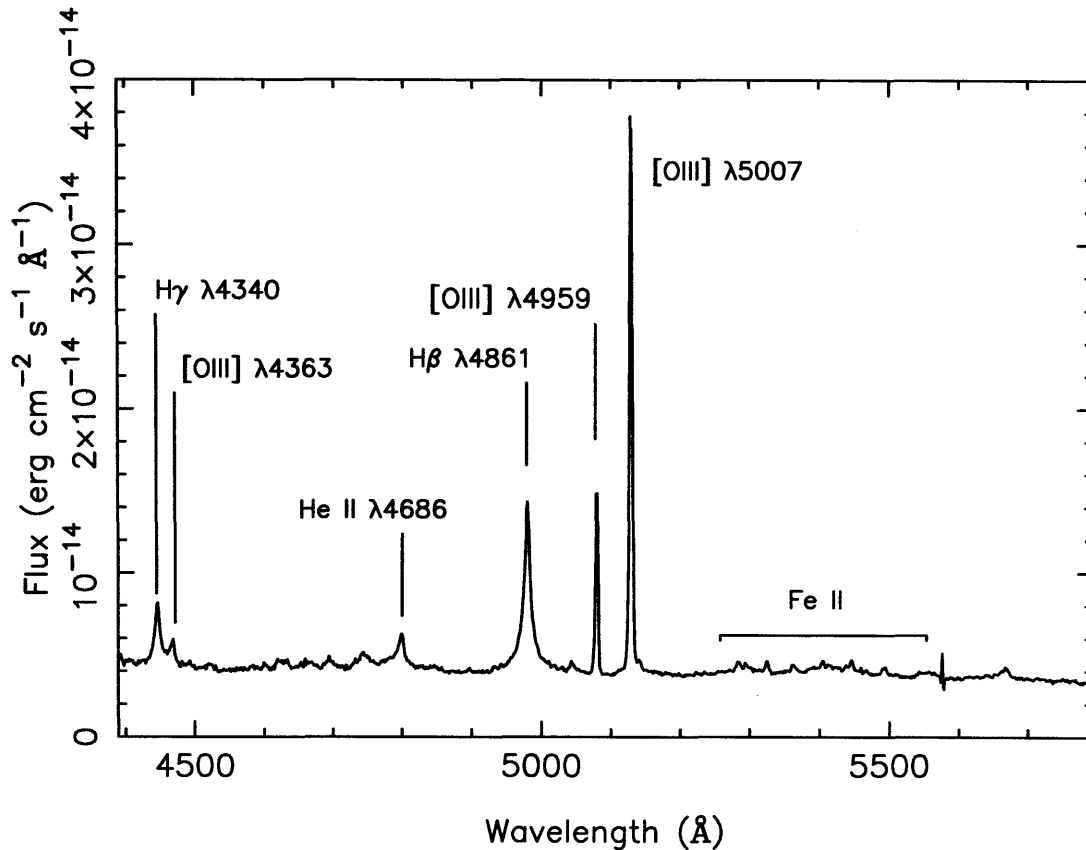


Figure 3.1: Optical spectrum of Ark 564 showing the relatively narrow  $\text{H}\beta$  line profile and Fe II emission.

### 3.3 Observations and data reduction

#### 3.3.1 The ASCA observations

Ark 564 was observed by *ASCA* on 23–25 December 1996 for a duration of 103 ksec. The data were extracted as in Section 2.2, leaving 47 ksec of ‘good’ data.

There are significant calibration problems in these *ASCA* spectra at soft energies; the SIS and GIS spectra diverge at  $\sim 1$  keV, differing by 30% at 0.8 keV, and the two SIS spectra diverge from each other at lower energies (see Appendix A of Weaver, Gelbord & Yaqoob 2001). This is most likely due to radiation damage to the SIS CCDs. The response of the GIS detectors is not thought to be time-dependent, but their sensitivity is poor below 1 keV. In order to minimize the effect of these uncertainties in the spectral analysis presented here, the SIS data below 1.0 keV were ignored, as were the GIS data below 0.8 keV.

The SIS lower-level discriminator setting was changed during this observation. (The level was relaxed mid-observation to permit detection of photons down to 0.41 keV; M. Ishida, priv. comm.) In order to assess the impact on the spectral analysis, separate SIS spectra and response matrices were generated for each discriminator setting. The difference between the spectra obtained with the different discriminator settings was not significant and was much smaller than the difference between the SIS-0 and SIS-1 spectra. Therefore, in the following analysis the data gathered with different discriminator settings were combined.

Source and background light curves were extracted in 128s bins, from both SIS detectors, in the soft (0.5–2 keV) band. (Note that a softer band was used for the light curves because the spectral calibration problems mentioned above have a much smaller effect on temporal analysis.) The background subtracted light curves from each SIS were combined to increase signal/noise and the resulting light curve was binned by orbit (5760s) for the temporal analysis.

### 3.3.2 The RXTE observations

Ark 564 was observed by the Rossi X-Ray Timing Explorer (*RXTE*) simultaneously with *ASCA* for a duration of 95 ksec. The *RXTE* Proportional Counter Array (PCA) consists of five collimated Proportional Counter Units (PCUs), sensitive to X-rays in a nominal 2–60 keV bandpass and with a total collecting area of  $\sim 6250 \text{ cm}^2$ . In the following analysis, data from the top (most sensitive) layer of the PCU array were extracted using the REX reduction script and SAEXTRACT v4.2b.

Poor quality data were excluded on the basis of the following acceptance criteria: the satellite has been out of the South Atlantic Anomaly (SAA) for at least 20 min; Earth elevation angle  $\geq 10^\circ$ ; offset from optical position of Ark 564  $\leq 0.02^\circ$ ; and ELECTRON0  $\leq 0.1$ . This last criterion removes data with high anti-coincidence rate in the propane layer of the PCUs. These selection criteria left a total of 43.6 ks of good data.

The extraction improves upon that of Vaughan *et al.* (1999) by making use of new PCA calibration<sup>1</sup> and data reduction software. In particular the data selection criteria (i.e. TIME\_SINCE\_SAA) have been relaxed slightly and data have been extracted from all five PCUs in order to improve the signal-to-noise of the *RXTE* spectrum. The background was estimated using the latest version of the ‘L7–240’

<sup>1</sup>See [http://lhea-www.gsfc.nasa.gov/users/keith/rossi2000/energy\\_response.ps](http://lhea-www.gsfc.nasa.gov/users/keith/rossi2000/energy_response.ps)

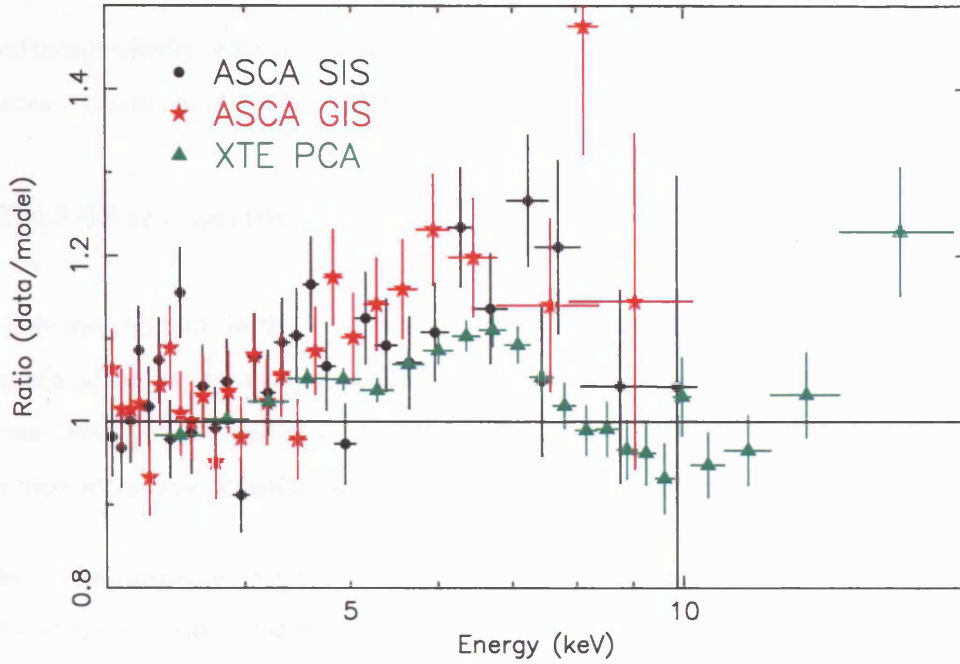


Figure 3.2: The *ASCA* and *RXTE* data compared to a power-law fitted over 3–18 keV but excluding the iron K band (4.5-9 keV).

model (Jahoda et al. 2000), specifically the model files `pca_bkgd_faint240_e3v19990909.mdl` and `pca_bkgd_faint17_e3v19990824.mdl` have been used.

As with the *ASCA* data, the background-subtracted pulse height spectrum from the PCU array was binned to give at least 20 counts per channel. In the subsequent spectral fitting the *RXTE* data below 3 keV have been ignored in order to avoid calibration uncertainties, as well as above 18 keV. The hard band (2–10 keV) light curve was extracted in 16s bins and, as with the *ASCA* light curve, was rebinned by orbit.

### 3.4 Spectral analysis

There remain problems with the inter-calibration of *RXTE* and *ASCA*. In this observation the *RXTE* spectrum overestimated the flux in the overlapping 3–10 keV band by  $\sim 25$  per cent compared to *ASCA*, and there is a difference in spectral slope of  $\Delta\Gamma \sim 0.15$ , with *RXTE* showing a steeper slope than *ASCA*. The PCA calibration gives a slope for the Crab spectrum that is  $\Delta\Gamma \sim 0.1$  steeper than that of previous missions and overestimated the flux. Therefore, for the following *ASCA* plus *RXTE* spectral analysis, the normalisations of the different instruments are left as free parameters and the *RXTE* spectral slope is

determined independently of the *ASCA* slope (but in practice differs from *ASCA* by  $\Delta\Gamma \lesssim 0.2$ ). Spectral slopes, fluxes and equivalent widths are given for the *ASCA* data.

### 3.4.1 The 3–18 keV spectrum

Initially, only the spectrum in the 3–18 keV range was analysed. A simple spectral fit using a model consisting of a power-law continuum modified by Galactic absorption ( $N_H = 6.4 \times 10^{20} \text{ cm}^{-2}$ , Dickey & Lockman 1990) gave a steep slope but a poor overall fit to the data (see Table 3.1, model 1). In particular there were clear deviations in the data–model residuals around 5–9 keV (see Fig. 3.2).

The addition of a narrow ( $\sigma = 0.01 \text{ keV}$ ) Gaussian line near 6.4 keV, to represent  $K_\alpha$  emission from neutral iron (model 2), improved the fit significantly ( $> 99.9\%$  significance in an F-test). The best-fit energy of the line was consistent with 6.4 keV but the width of this line was not well constrained using these data. Even after the addition of an iron line the residuals showed a deficit at  $\sim 8 \text{ keV}$ , particularly in the *RXTE* data. In order to quantify these features a range of simple models were fitted to the data (see Table 3.1). Specifically, models were used which included a line and an edge at energies expected from neutral iron (model 3), from helium-like iron (model 4), and with the energies left free (model 5). The He-like features provided a better fit than neutral features, but the best fit values lay between these two extremes (see Fig. 3.3). The important point is that the iron K-edge appeared at an energy clearly above that for neutral iron. Repeating the fitting with lines of increasing width, up to  $\sigma = 0.5 \text{ keV}$ , suggested that the edge energy is not an artifact of trying to fit a possible broad emission feature with a narrow line. In these fits the absorption edge energy and optical depth remained consistent with the values given above for the narrow line fit. The measured energy of the edge implies an origin in strongly ionised material. This could, in principle, lie along the line of sight (a ‘warm absorber’) or arise by reflection from optically thick matter having a highly ionised surface layer (an ‘ionised reflector’).

To pursue these alternatives, the spectra above 3 keV were fitted with the `absori` warm absorber model. The free parameters were power-law slope and normalisation, iron line energy and flux, column density and ionisation parameter ( $\xi = L/nr^2$ ; where  $n$  is the particle density at a distance  $r$  from a source of ionising luminosity  $L$ , measured in the 0.005–20 keV range). The temperature of the absorbing gas was fixed at  $10^6 \text{ K}$ . This model provided a good fit to the data ( $\chi^2_\nu = 0.96$ ; see Table 3.1, model 6). A very high  $\xi$  is needed to explain the energy of the iron edge, with a column density in excess of  $10^{23} \text{ cm}^{-2}$ . Such a highly ionised absorber, if indeed stable, will be essentially transparent at lower energies.

Table 3.1: Results of simultaneous fits to the *ASCA* and *RXTE* data in the 3–18 keV range. The columns provide the following information: (1) the type of spectral model (as defined in the text); (2) the power-law photon index; (3) and (4) the iron line energy (keV) and equivalent width (eV) respectively; (5) the iron edge energy (keV) or the ionisation parameter; (6) the edge depth, the column density of absorbing gas ( $10^{22}$  cm $^{-2}$ ) or the reflection strength; (7) the best-fit  $\chi^2$  and number of degrees of freedom in the fitting.

Model (1)	$\Gamma$ (2)	$E_{line}$ (3)	EW (4)	$E_{edge}/\xi$ (5)	$\tau/N_H/R$ (6)	$\chi^2/dof$ (7)
1. PL	$2.35 \pm 0.05$	–	–	–	–	967/902
2. PL+LINE	$2.38 \pm 0.04$	$6.35^{+0.19}_{-0.15}$	$81^{+16}_{-20}$	–	–	910/900
3. PL+LINE+EDGE	$2.37^{+0.03}_{-0.07}$	$6.4^f$	$70^{+23}_{-15}$	$7.10^f$	$0.08^{+0.04}_{-0.05}$	903/900
4. PL+LINE+EDGE	$2.35 \pm 0.04$	$6.7^f$	$41^{+21}_{-25}$	$8.76^f$	$0.25 \pm 0.06$	877/900
5. PL+LINE+EDGE	$2.34 \pm 0.05$	$6.28^{+0.32}_{-0.21}$	$43^{+17}_{-30}$	$8.25^{+0.19}_{-0.21}$	$0.25^{+0.03}_{-0.07}$	865/898
6. PL+ABSORI+LINE	$2.51 \pm 0.10$	$6.36^{+0.40}_{-0.20}$	$40^{+24}_{-20}$	$6.4^{+6.3}_{-3.3} \times 10^3$	$21.1 \pm 8.3$	863/898
7. PL+PEXRIV+LINE	$2.53^{+0.09}_{-0.08}$	$6.4^f$	< 38	$473^{+1532}_{-227}$	$0.7^{+0.4}_{-0.3}$	873/899

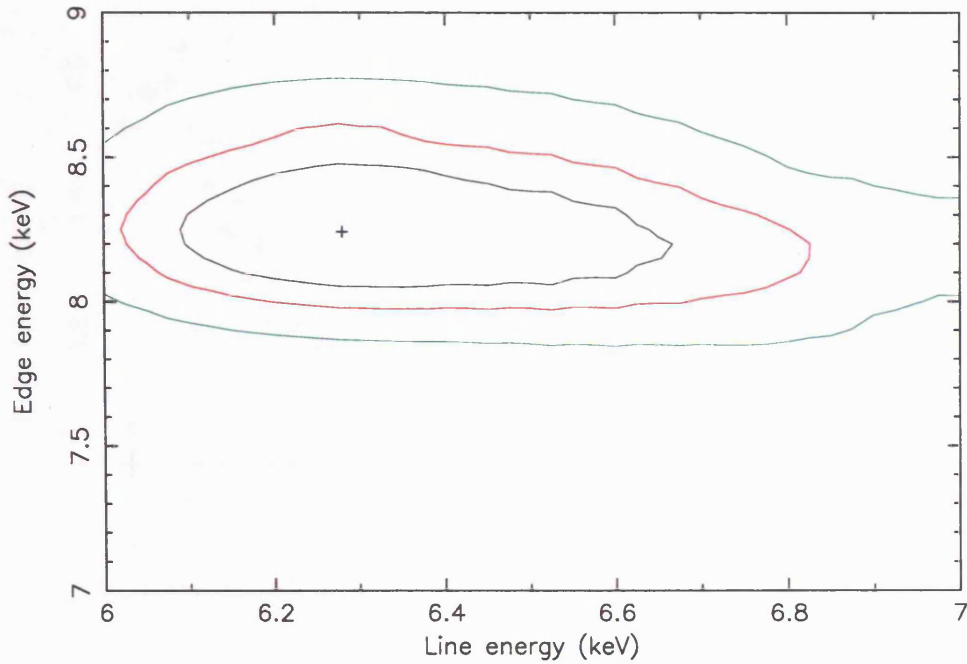


Figure 3.3: Confidence contours for the iron K-line and -edge energies, from model 5, Table 3.1. Contours mark the 68, 90 and 99% confidence levels. The edge energy is clearly not consistent with a neutral iron edge at 7.1 keV.

As an alternative, the 3–18 keV spectrum was fitted with the `pexriv` ionised reflection model (Magdziarz & Zdziarski 1995). This model consists of a power-law and reflection component from ionised material but does not contain the emission lines expected from such a reflector. The properties of any iron line emission were poorly constrained from the data and therefore the line energy was fixed at 6.4 keV. This is not necessarily inconsistent with emission from an ionised disc as the line is expected to be broadened and redshifted if the emitting region is in close proximity to the central black hole. The free parameters in the fit were the power law index and normalisation, iron line flux, the reflection strength ( $R^2$ ) and the ionisation parameter. The inclination of the reflector was fixed at  $30^\circ$  (a value which Nandra *et al.* 1997a found to be typical for Seyfert 1s based on the iron line profile) and the elemental abundances were assumed to be solar. The surface temperature of the reflector was fixed at  $10^6$  K, consistent with values expected for an ionised disc (e.g. Ross *et al.* 1999). This model also provided a good fit to the data ( $\chi^2_\nu = 0.97$ ; Table 3.1, model 7), comparable to the warm absorber model, with plausible values for both  $\xi$  and  $R$  (compared with the more detailed accretion disc models in Ballantyne, Iwasawa & Fabian 2000).

<sup>2</sup> $R$  is the ratio of the normalisations of the power-law incident on the reflector and the observed power law. A value of  $R = 1$  is expected for a disc which covers  $2\pi$  sr as seen from the X-ray source.

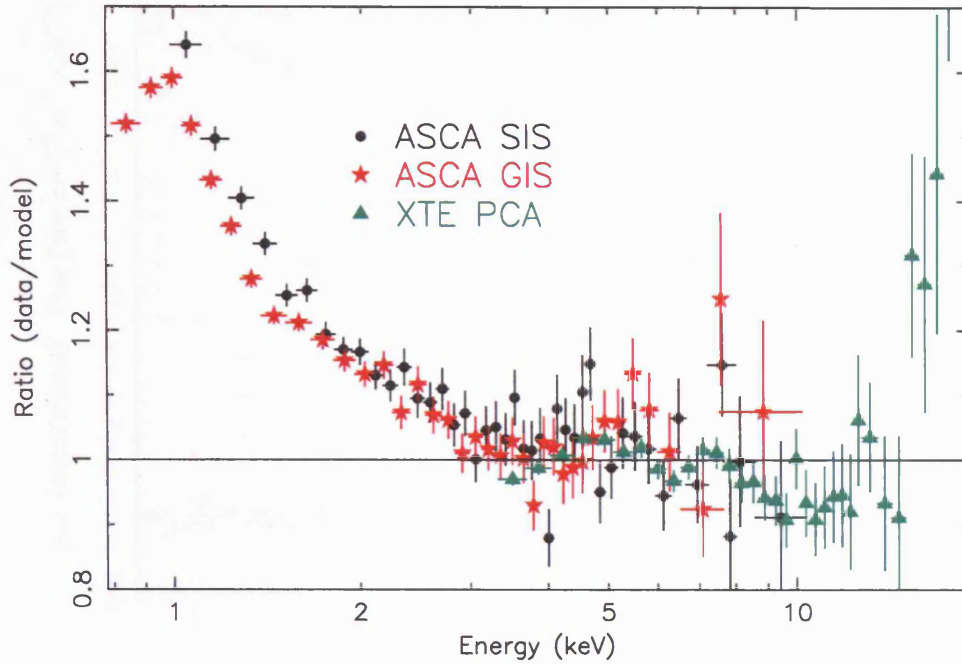


Figure 3.4: Data/model ratio produced by extrapolating the hard power-law (Table 3.2, model 2) down to 0.8 keV, revealing the soft excess emission.

### 3.4.2 The 0.8–18 keV spectrum

Having obtained a satisfactory description of the hard X-ray spectrum of Ark 564 the analysis was extended to cover the 0.8–18 keV range, but excluding the SIS data below 1.0 keV in order to avoid the calibration uncertainties mentioned above. Extrapolating a simple power-law plus line fit to the hard spectrum (Table 3.1, model 2) down to 0.8 keV shows the strong soft excess (see Figure 3.4). Refitting the ionised reflector model (Table 3.2, model 7) gave some reduction in the strength of the soft excess, due to the enhanced reflectivity of the ionised matter. However the fit (Table 3.2, model 1) still left substantial excess which was well modeled by the addition of a  $kT \approx 100$  eV black body component (leading to  $\Delta\chi^2 > 150$ ; Table 3.2, model 2).

The steep underlying power law, enhanced by the high reflectivity of the ionised disc, led to a smaller black body component than would otherwise be the case. A more complete ionised reflector model would include significant soft X-ray emission. Reference to the disc reflection models of Ross, Fabian & Young (1999) and Nayakshin, Kazanas & Kallman (2000), suggests that ionised oxygen features, in particular the recombination continuum of O VIII (above 0.87 keV) and the O VIII Ly- $\alpha$  emission line (at 0.65 keV), will be prominent for values of the ionisation parameters similar to those derived for

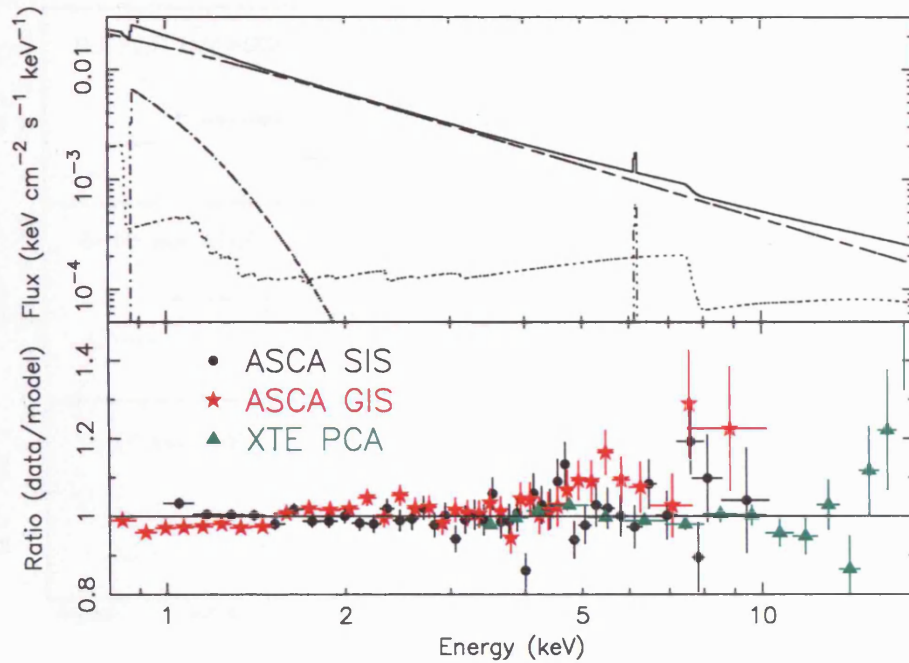


Figure 3.5: Input model and data/model ratio from the *ASCA* and *RXTE* spectrum of Ark 564 (see model 3, Table 3.2). The model spectrum (solid curve) represents the best-fit power law plus ionised reflector (dashed curves), including an O VIII recombination feature at 0.87 keV and iron line at 6.4 keV (dotted curves). The data/model residuals indicate a good fit, both in the iron K band and at softer energies.

Ark 564. (The O VIII recombination continuum has also been detected in Seyfert 2s, see Griffiths *et al.* 1998.) Therefore, as an alternative to the black body component, the ionised reflector model was refitted with the addition of O VIII recombination at 0.87 keV (using the `redge` model in XSPEC). The result (Table 3.2, model 3) was a good fit (very similar, in statistical terms, to the previous model) with a best fit temperature of  $\sim 180$  eV (i.e. within a factor of two of the earlier assumption of a disc temperature of  $10^6$  K) and a strength comparable with the predictions of more detailed accretion disc models. Therefore, to first order, both the iron K features and the soft excess in the *ASCA* and *RXTE* observation of Ark 564 can be explained in terms of reflection from highly ionised matter, presumably the putative accretion disc. Specifically, the spectral form of Ark 564 below 2 keV may have a natural explanation in terms of the combined effects of O and Si edges (present in the `pexriv` reflection continuum) together with associated recombination continuum and line emission. One important consequence of this ionised reflector description for Ark 564 is the need to reassess the strong ‘primary’ soft emission component, usually a major feature of NLS1, and generally associated with internally generated emission from the accretion disc.

The above interpretation of the X-ray spectrum of Ark 564, in terms of an ionised reflector, is also

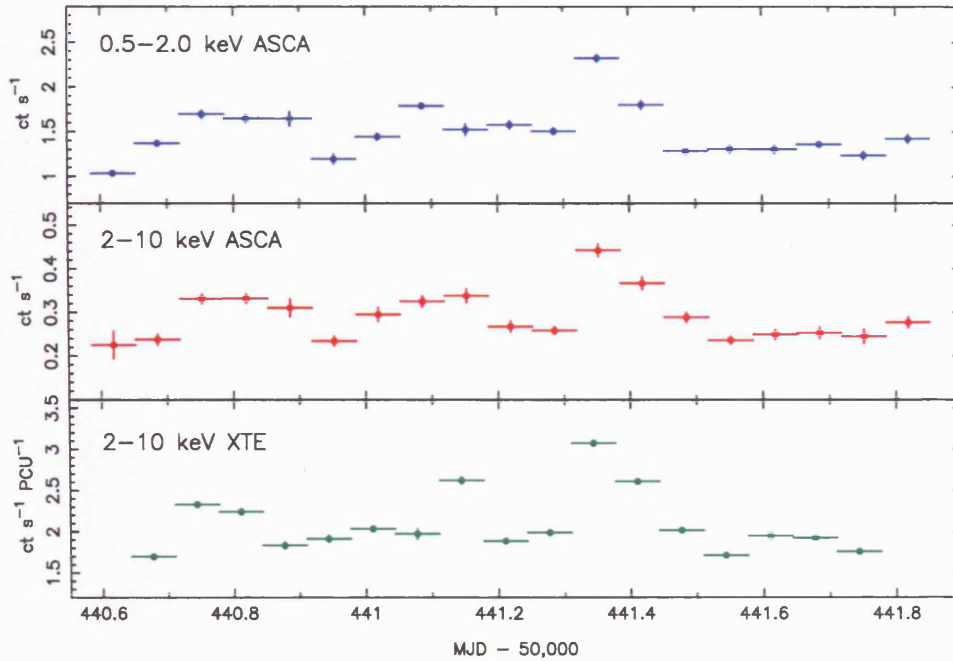


Figure 3.6: Light curves from *ASCA* and *RXTE*. Note the strong ( $\gtrsim 50\%$ ) flare near day 441.3, which is virtually identical in phase and amplitude in both bands. Errors are  $\pm 1\sigma$ .

consistent with the measured *BeppoSAX* spectrum (see Pounds & Vaughan 2000).

### 3.5 Temporal analysis

These data were also used to study the variability properties of Ark 564. Fig. 3.6 shows that the *ASCA* soft (0.5–2 keV) and hard (2–10 keV) and the *RXTE* hard (2–10 keV) band light curves reveal strong flaring, with an increase of  $>50\%$  in a single orbit that is almost identical in amplitude and phase in both bands.

The normalised excess variance ( $\sigma_{xs}^2$ ) was computed in the same fashion as Nandra *et al.* (1998) in order to quantify the variability in Ark 564. For Ark 564, the soft and hard band excess variances measured from *ASCA* are  $\sigma_{xs}^2 = 0.0357$  and  $0.0316$ , respectively, and  $0.0340$  for *RXTE*. This compares with a typical value found by Nandra *et al.* (1997b) for ‘normal’ Seyfert 1s with similar X-ray luminosity ( $\sim 6 \times 10^{43}$  erg/s) of  $\sigma_{xs}^2 = 0.005$  in the *ASCA* 0.5–10 keV band.

It is also interesting that Ark 564 showed almost identical variability amplitudes in the hard *RXTE* and soft *ASCA* bands. Furthermore, the hard and soft band variations track almost perfectly, with no measur-

Table 3.2: Results of simultaneous fits to the *ASCA* and *RXTE* data in the 0.8–20 keV range. The columns give the following information: (1) the models (as defined in the text); (2) the power law photon index; (3) the black body temperature (eV); (4) the disc ionisation parameter ( $\xi$ ); (5) the strength of the reflection component ( $R$ ); (6) the equivalent width of the O VIII recombination feature (eV); (7) the temperature derived from the O VIII feature (eV); (8) the best-fit  $\chi^2$  and number of degrees of freedom.

Model (1)	$\Gamma$ (2)	kT (3)	$\xi$ (4)	R (5)	$EW_{OVIII}$ (6)	$kT_{OVIII}$ (7)	$\chi^2/\text{dof}$ (8)
1. PL+PEXRIV	$2.78 \pm 0.01$	–	$424 \pm 230$	$> 1.54$	–	–	1839/1543
2. PL+PEXRIV+BB	$2.55 \pm 0.03$	$184 \pm 6$	$257^{+109}_{-133}$	$0.65^{+0.19}_{-0.15}$	–	–	1682/1541
3. PL+PEXRIV+LINES	$2.63 \pm 0.01$	–	$625 \pm 190$	$0.84 \pm 0.15$	$58 \pm 9$	$177 \pm 15$	1562/1541

able lag, especially during the large flare. In terms of the ionised reflection model, in which a substantial fraction of the soft X-ray flux is reprocessed harder radiation, the observed limit on the lag ( $\lesssim 96$  min), gives a maximum size for the effective reprocessing region of  $\sim 2 \times 10^{14}$  cm ( $\approx 60 R_S$  around a  $10^7 M_\odot$  black hole).

### 3.6 Discussion

The simultaneous *ASCA* and *RXTE* data presented here gave the first determination of the spectrum of an ‘ultra-soft’ NLS1 extending above 10 keV. The spectrum was extremely steep ( $\Gamma \approx 2.6$ ) and showed little sign of flattening at harder energies. There was good evidence for both K-edge and line features from ionised iron and the spectrum also showed a strong excess over the best-fit power law below 1.5 keV. Due to calibration problems with the *ASCA* detectors at low energies (see Iwasawa, Fabian & Nandra 1999), the data were not fitted below 0.8 keV and so the form of this soft excess was not well determined by these data. (An alternative description of the soft X-ray feature seen in the *ASCA* data of Ark 564 is given by Turner, George & Netzer 1999).

The existence of strong soft X-ray emission and an underlying power law much steeper than typical of BLS1s and quasars are now well established characteristics of the X-ray spectra of NLS1s (see Chapter 2). It has been suggested that the two features are linked, whereby Compton cooling of the hard X-ray source (possibly in a disc corona), and hence its steeper power law, is a consequence of the strong soft EUV flux (Pounds, Done & Osborne 1995). In this picture, the soft component, probably peaking in the hidden EUV band, is intrinsic emission from the accretion disc, which is expected to be stronger in high accretion rate objects (e.g. Szuszkiewicz, Malkan & Abramowicz 1996).

In the present analysis other spectral features are found, namely an ionised iron K-edge and recombination emission below  $\sim 1.5$  keV, indicative of reflection from an ionised disc. The higher level of irradiation thought to occur in NLS1s would lead naturally to the surface layers of the disc becoming strongly ionised (Matt, Fabian & Ross 1993). In contrast, an alternative interpretation for the observed iron K-edge - absorption in a large column of highly ionised gas - is less attractive, since the gas may well be unstable (Netzer 1993) and such material would be transparent in the soft X-ray band, leaving the need for a separate explanation of the the observed spectral features below  $\sim 2$  keV.

The ionised disc explanation is supported the recent work of Ballantyne, Iwasawa & Fabian (2000) who use the more sophisticated reflection model of Ross, Fabian & Young (1999). However, both *pexriv* and the Ross, Fabian & Young (1999) model are limited in that they assume a fixed density structure for the reflecting material. Nayakshin, Kazanas & Kallman (2000) and Ballantyne, Ross & Fabian (2001) have relaxed this assumption by developing models for X-ray illuminated accretion discs including calculations of hydrostatic balance as well as ionisation balance and radiative transfer in the disc. The predictions of these, more physically realistic models, differ slightly from those of the fixed density models. In particular, three discrete thermally stable layers are predicted, whose optical depths and effective temperatures depend on the intensity *and* spectral index of the irradiating X-rays. In the case of a ‘normal’ Seyfert 1 spectrum, the outermost layer, closest to the ionising source, is predicted to be almost fully ionised and at the local Compton temperature ( $\sim 10^7 - 10^8$  K), while at larger depths the temperature decreases sharply to the thermal disc temperature. In terms of the reflected X-ray spectrum, the upper layer is effectively a good mirror, introducing few spectral features, while the lowest layer will act like a cold (neutral) reflector, yielding the 6.4 keV Fe  $K_{\alpha}$  line and reflection hump.

However, with a steeper incident spectrum – as is the case in Ark 564 – the models predict a region of substantial optical depth with intermediate temperature ( $T \sim 10^6$  K) and ionisation. Reflection from such material would superimpose significant spectral features on the emerging X-ray spectrum, as observed in Ark 564.

An important consequence of the steep underlying power law of Ark 564, enhanced at low energies both by the high reflectivity of the disc and the additional line and recombination emission, is that the need for a primary emission ‘soft excess,’ at least within the observable X-ray band, must be reconsidered when better data from e.g., *XMM-Newton* and *Chandra* become available. However, the circumstantial evidence for the soft X-ray/EUV flux to dominate energetically in Ark 564 remains persuasive, particularly in providing a natural explanation for the steep hard power law spectrum and the absence of broad optical lines (see also § 2.4.2).

Evidence for reflection from an ionised disc has been reported in several GBHCs, exhibiting strong, ionised edges with weak, Compton-broadened Fe lines (e.g., Zycki, Done & Smith 1997, Zycki, Done & Smith 1998; but see Done & Zycki 1999). The similarity of NLS1s to GBHCs in their ‘soft state’ has been noted earlier by Pounds, Done & Osborne (1995). It is interesting to speculate that the reported weakness in higher luminosity AGN (e.g. Reeves *et al.* 1997), of the reflection components commonly

seen in BLS1 (George *et al.* 1998), may be a due to the accretion disc material in the former being highly ionised (see Reeves *et al.* 2000), with the classical indicators of cold reflection, namely strong iron fluorescence and a continuum hump above 10 keV, consequently reduced.

## Chapter 4

# The ROSAT Wide-Field Camera Extragalactic Survey

### 4.1 Overview

The results are reported of a new analysis of the *ROSAT* Wide Field Camera (WFC) all-sky survey data, designed to detect extragalactic sources of extreme ultraviolet (EUV) radiation in regions of low Galactic  $N_H$ . A total of 19 AGN are identified, more than double the number of confirmed AGN in the published WFC (2RE) survey. The chapter is organised as follows. In Section 4.3 the sample is defined, followed by a description of some of its most important properties in Section 4.4. Finally, an approximate luminosity function is derived in Section 4.5 and the local volume emissivity of EUV-selected AGN is calculated.

### 4.2 The ROSAT survey

During 1990, *ROSAT* performed an all-sky survey in both the soft X-ray (0.1–2.4 keV) and EUV (60–210 eV) bands. The former employed the *ROSAT* X-ray telescope and position sensitive detector (PSPC; Trümper *et al.* 1991) and the latter the co-aligned UK Wide Field Camera (WFC; Sims *et al.* 1990). The result has been the publication of the *ROSAT* Bright Source Catalogue (RBSC; Voges *et al.* 1999) and the WFC RE and 2RE catalogues (Pounds *et al.* 1993; Pye *et al.* 1995). In the present analysis the WFC all-sky survey database is utilised to produce the first reasonably large and complete sample of EUV-selected extragalactic objects, all of which are identified as AGN.

### 4.3 The Source Catalogue

The selection criteria used to include a source in the preliminary source list are as follows:

1. A WFC all-sky survey S1 band (90–210 eV; 60–140 Å) detection at  $\geq 2.5\sigma$
2. An S2 band (60–110 eV; 110–210 Å) *null* detection
3. A coincident strong RBSC X-ray detection (0.1–2.4 keV count rate  $\geq 0.3$  ct/sec) within 100'' of the S1 position
4. A value of the foreground Galactic column density in the direction of the source of  $N_H \leq 2.5 \times 10^{20} \text{ cm}^{-2}$  (Dickey & Lockman 1990)

Criterion (3) allowed the current survey to go more than a factor of 2 below the  $5.5\sigma$  WFC 2RE survey limit (Pye *et al.* 1995), since the requirement for *both* an S1 and soft X-ray detection limits the number chance coincidences in the sample to much less than one. Criteria (2) and (4) select against Galactic sources, since there is no reasonable expectation of extragalactic sources being detectable in the S2 band anywhere in the sky or in the S1 band if the Galactic column is too high. For example, in the S2 band, even for the lowest-column source in the sample (which has  $N_H = 6 \times 10^{19} \text{ cm}^{-2}$ ),  $\tau_{S2} = 3.7$ , corresponding to a fractional transmission of only 2.6%. For comparison the transmission in the S1 band is 16% for this same source. However, at the survey limit of  $N_H = 2.5 \times 10^{20} \text{ cm}^{-2}$ , even the S1 transmission has declined to 0.6%. Clearly only the brightest extragalactic sources would be able to be detected in the presence of such strong attenuation.

A total of 34 WFC sources were found to satisfy the above criteria. For this preliminary sample of EUV sources, SIMBAD and other catalogues were searched for potential optical counterparts. This process proved efficient in that all but one of the sources (RX J0437–47; see § 4.3.2) were identified in this fashion. The fully identified sample comprises 19 extragalactic and 15 Galactic sources. Details of these sources are presented below.

### 4.3.1 The Extragalactic Sources

Table 4.1 contains a compilation of the *ROSAT* data for the extragalactic sample. The columns provide the following information: (2) the source name; (3) the WFC S1 count rate and  $1\sigma$  error; (4) the  $2.5\sigma$  upper limit on the WFC S2 count rate; (5) the RBSC full-band (0.1–2.4 keV) count rate; (6) and (7) the *HR1* and *HR2* hardness ratios; (8) the X-ray energy index,  $\alpha_X$  (see § 4.4.4); (9) and (10) the right ascension and declination as tabulated in the RBSC; (11) the difference between the RBSC and WFC positions in arcsec. Note that the two hardness ratios *HR1* and *HR2* apply to the full PSPC band and the hard PSPC band, respectively (i.e.,  $HR1 = (H - C)/(H + C)$  and  $HR2 = (H2 - H1)/(H1 + H2)$  where *C* is the 0.1–0.4 keV count rate, *H* the 0.5–2 keV count rate, *H1* the 0.5–0.9 keV count rate, and *H2* the 0.9–2 keV count rate). Also we quote the RBSC positions in preference to the WFC positions since the former are more accurate (the X-ray telescope had better spatial resolution and typically recorded at least 10 times more counts than the WFC).

Information from other wavebands is presented in Table 4.2: column 3 gives the object type as defined in the literature (note that the  $H\beta$  line widths of the NLS1s and BLS1s overlap) column 4 gives the Galactic value of  $N_H$  derived from the survey of Dickey & Lockman (1990), columns 5–7 give the V-band optical magnitude, redshift and  $H\beta$  line width, as reported in the optical observations referenced in column 10. Columns 8 and 9 give the monochromatic luminosity at 200 eV ( $L_{200}$ ) and optical/EUV spectral slope,  $\alpha_{OE}$ , as derived in § 4.6 and § 4.4.4, respectively.

Since the EUV and soft X-ray data in Table 4.1 were gathered from a single mission at the same time, correlations and colours measured from them are reliable. However, many of the data in Table 4.2 were taken from a variety of non-simultaneous measurements, and thus any ratios involving these quantities (e.g.,  $\alpha_{OE}$ ) may be influenced by any temporal variability of the source.

### 4.3.2 Notes on Individual Sources

**WPVS 7:** With  $HR1 = -0.97$ , this NLS1 is the softest AGN in the sample. There are almost no counts in bands *H1* and *H2*, so the hardness ratio *HR2* is not well-determined. The foreground HI column is comparatively high at  $2.5 \times 10^{20} \text{ cm}^{-2}$  and, after correcting for the Galactic transmission, this is the brightest Seyfert galaxy in the sample (in terms of its incident flux). WPVS 7 appears to be a transient source, as subsequent pointed *ROSAT* observations show that its X-ray flux dropped by a factor of  $\sim 400$

Table 4.1: The WFC AGN Sample: *ROSAT* Data

No.	Name	S1 (ct/ks)	S2 (ct/ks)	RBSC (ct/s)	HR1	HR2	$\alpha_X$	R.A. (J2000)	Dec. (J2000)	Offset (")
(1)	(2)	(3)	(4)	(5)	(6)	(7)	(8)	(9)	(10)	(11)
1	WPVS 7	23±8	<15	0.96±0.07	-0.97 ± 0.01	—	4.8	00 39 15.6	-51 17 01	47
2	LB 1727	10±4	<4	4.56±0.21	-0.52 ± 0.08	0.68 ± 0.16	2.5	04 26 01.6	-51 12 01	34
3	RX J0437-47	19±7	<22	0.85±0.09	-0.64 ± 0.07	0.33 ± 0.25	2.5	04 37 26.6	-47 11 18	60
4	GB 1011+49	12±4	<4	1.94±0.07	-0.38 ± 0.03	-0.03 ± 0.06	1.2	10 15 04.3	49 26 04	38
5	1ES 1028+511	14±4	<8	4.46±0.09	-0.26 ± 0.02	0.09 ± 0.03	1.2	10 31 18.6	50 53 40	21
6	RE J1034+39	23±5	<16	2.66±0.09	-0.74 ± 0.02	-0.37 ± 0.08	2.0	10 34 38.7	39 38 34	31
7	EXO 1055+60	13±4	<11	0.39±0.03	-0.76 ± 0.04	-0.09 ± 0.21	2.0	10 58 30.1	60 16 02	37
8	Mrk 421	85±9	<16	26.60±0.23	-0.21 ± 0.01	0.02 ± 0.01	1.2	11 04 27.1	38 12 31	43
9	IC 3599	17±4	<5	5.10±0.11	-0.63 ± 0.01	-0.46 ± 0.04	1.9	12 37 41.4	26 42 29	96
10	IRAS 13349+243	15±4	<7	2.53±0.09	-0.65 ± 0.02	-0.13 ± 0.08	2.0	13 37 18.8	24 23 06	41
11	PG 1415+451	8±2	<8	0.50±0.03	-0.66 ± 0.03	-0.19 ± 0.11	2.0	14 17 00.5	44 55 56	34
12	NGC 5548	12±4	<5	4.95±0.11	-0.11 ± 0.02	0.17 ± 0.03	1.3	14 17 59.6	25 08 17	50
13	1H 1430+423	18±5	<12	4.20±0.09	-0.60 ± 0.05	0.12 ± 0.03	2.0	14 28 32.0	42 40 28	69
14	Mrk 478	66±7	<18	5.78±0.10	-0.70 ± 0.01	-0.11 ± 0.05	2.0	14 42 07.7	35 26 32	35
15	RX J1618+36	10±4	<9	0.85±0.03	-0.43 ± 0.03	-0.01 ± 0.07	1.6	16 18 09.2	36 19 50	93
16	RX J1629+40	12±3	<7	0.78±0.03	-0.79 ± 0.02	0.00 ± 0.13	2.3	16 29 01.2	40 07 53	29
17	PKS 2155-304	180±12	<17	36.20±1.53	-0.42 ± 0.03	-0.04 ± 0.07	1.8	21 58 52.2	-30 13 37	11
18	NGC 7213	12±4	<4	3.94±0.27	0.24 ± 0.06	0.23 ± 0.08	0.9	22 09 16.6	-47 10 02	21
19	RE J2248-51	18±5	<10	2.24±0.17	-0.65 ± 0.05	0.17 ± 0.17	2.2	22 48 41.4	-51 09 51	26

Table 4.2: The WFC AGN Sample: Derived Data and Data from Other Wavebands

No.	Name	Type	$N_H$ ( $10^{20} \text{ cm}^{-2}$ )	V-band Magnitude	Redshift	H $\beta$ FWHM (km/s)	$\log(L_{200})$ (erg/s/keV)	$\alpha_{OE}$	Reference
(1)	(2)	(3)	(4)	(5)	(6)	(7)	(8)	(9)	(10)
1	WPVS 7	NLS1/Trans	2.5	14.8	0.029	1620	45.3	0.66	1
2	LB 1727	BLS1	2.0	14.3	0.103	3460	45.7	1.10	2
3	RX J0437–47	BLS1	1.8	15.3	0.050	4600	45.2	0.82	3
4	GB 1011+49	BL Lac	0.8	16.1	0.200	—	45.4	1.16	4
5	1ES 1028+511	BL Lac	1.2	17.0	0.361	—	46.2	0.76	5
6	RE J1034+39	NLS1	1.0	15.6	0.042	1500	44.6	1.03	6
7	EXO 1055+60	NLS1	0.6	17.0	0.149	2155	44.9	1.01	1
8	Mrk 421	BL Lac	1.4	13.5	0.030	—	45.2	1.00	7
9	IC 3599	NLS1/Trans	1.3	15.6	0.020	677	44.0	0.79	3
10	IRAS 13349+243	NLS1	1.2	15.0	0.107	2773	45.3	1.16	3
11	PG 1415+451	BLS1	1.2	15.7	0.114	2575	45.1	1.16	8
12	NGC 5548	BLS1	1.7	13.1	0.017	5900	44.0	1.41	9
13	1H 1430+423	BL Lac	1.4	16.4	0.129	—	45.7	0.75	10
14	Mrk 478	NLS1	1.0	15.0	0.077	1915	45.5	1.02	1
15	RX J1618+36	NLS1	1.3	16.9	0.034	1707	44.3	0.84	3
16	RX J1629+40	NLS1	0.9	19.0	0.272	2676	45.7	0.53	3
17	PKS 2155–304	BL Lac	1.7	13.0	0.116	—	46.8	0.83	11
18	NGC 7213	BLS1	2.1	10.5	0.006	3200	43.4	1.81	12
19	RE J2248–51	BLS1	1.4	15.0	0.102	3460	45.5	1.04	1

REFERENCES: (1) Grupe *et al.* (1999). (2) Guainazzi *et al.* (1998). (3) This work. (4) Puchnarewicz *et al.* (1992). (5) Polomski *et al.* (1997). (6) Puchnarewicz *et al.* (1995). (7) Miller (1975). (8) Boroson & Green (1992). (9) Osterbrock (1977). (10) Sambruna *et al.* (1997). (11) Falamo, Pesce & Lockman (1993). (12) Grupe (1996).

with respect to the survey measurement, the largest such variation seen for any Seyfert 1 galaxy (Grupe 1996).

**LB 1727:** The WFC 2RE catalogue reports the detection of an EUV source identified with the Seyfert 1 galaxy LB 1727 (1H 0419–577) but at a position over  $3'$  offset from the optical counterpart and a corresponding RBSC detection. A close examination of the WFC data for this field reveals that the 2RE source is in fact a blend of two sources of roughly equal brightness in the S1 band. These two sources are clearly resolved in pointed *EUVE* and *ROSAT* HRI observations and have been identified respectively with the Seyfert galaxy LB 1727 (Guainazzi *et al.* 1998; Turner *et al.* 1999a) and an AM Her star *EUVE* J0425.6–5714 (Halpern *et al.* 1998). When the effects of the source confusion are taken into account, the WFC source associated with LB 1727 meets all the criteria defined in § 4.3 and hence it is included in the sample.

**RX J0437–47:** This was the only source in the sample without a published optical spectrum. Low-resolution optical spectra were therefore acquired from the 3.9m Anglo-Australian Telescope using the RGO and FORS spectrographs, with total integration times of 1000 and 900 sec respectively, in  $\sim 2''$  seeing conditions. The combined, flux-calibrated spectrum, shown in Fig. 4.1, is that of a Seyfert 1 galaxy at a redshift of  $z = 0.051$ . The Balmer lines are clearly broad, with  $H\beta$  FWHM = 4600 km/s, identify this source as a BLS1.

**IC 3599:** This is another highly transient source, with later pointed *ROSAT* observations giving a flux  $\sim 100$  times lower than at the time of the all-sky survey. A recent optical spectrum most closely resembles that of an extragalactic H II region, but at the time of the survey this source clearly had the appearance of a NLS1 (Brandt, Pounds & Fink 1995) and that classification is adopted herein.

**1H 1430+423:** This AGN is listed as an S1 and S2 detection in the WFC 2RE survey (Pye *et al.* 1995) but only as an S1 detection in the original WFC RE survey (Pounds *et al.* 1993). An inspection of the relevant WFC survey image confirms that any detection in the S2 band is at best very marginal (see Figure 4.2). The S2 detection in the 2RE processing appears to be a result of confusion with the high background signal in this field. Since this source is clearly of extragalactic origin, and notwithstanding selection criterion (2) above, it has been included in the sample.

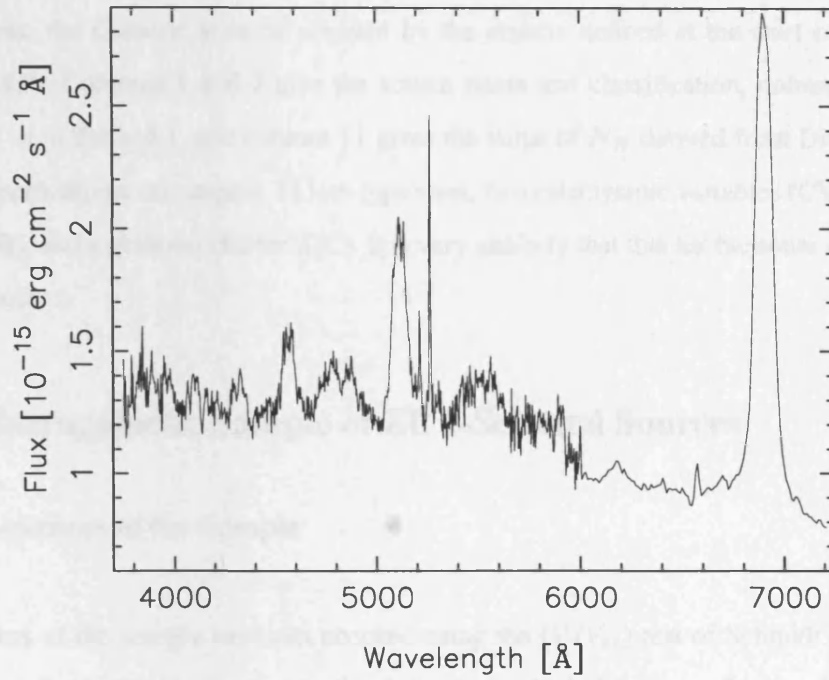


Figure 4.1: The optical spectrum of RX J0437-47.

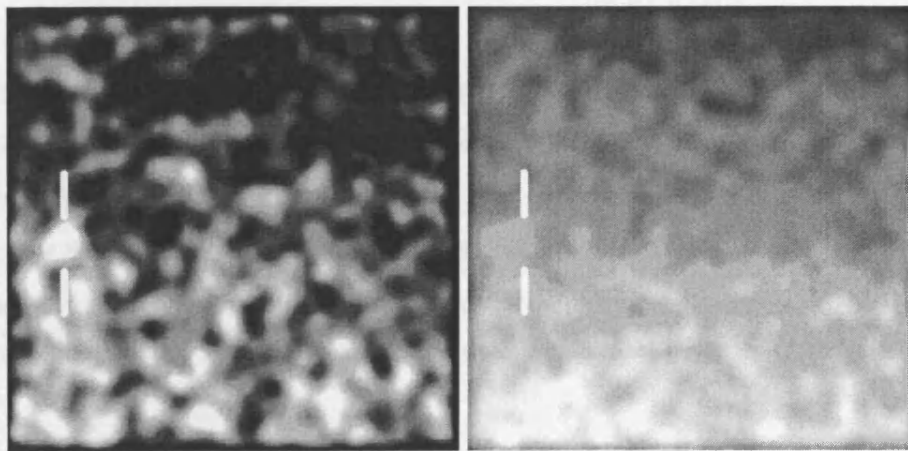


Figure 4.2: WFC S1 (left) and S2 (right) images of 1H 1430+423. The source is clearly detected (towards the left) in the S1 image but not in the S2 image.

### 4.3.3 The Galactic Sources

For completeness, the Galactic sources selected by the criteria defined at the start of this section are listed in Table 4.3. Columns 1 and 2 give the source name and classification, columns 3–10 give the same quantities as in Table 4.1, and column 11 gives the value of  $N_H$  derived from Dickey & Lockman (1990). The identifications encompass 11 late-type stars, two cataclysmic variables (CV), a low-mass X-ray binary (XRB), and a globular cluster (GC). It is very unlikely that this list harbours any unrecognized extragalactic sources.

## 4.4 The Extragalactic Sample of EUV-Selected Sources

### 4.4.1 Completeness of the Sample

The completeness of the sample has been checked using the  $\langle V/V_m \rangle$  test of Schmidt (1968). Here  $V_m$  represents the total volume of space out to the distance at which the source flux would drop below the survey limit. Likewise,  $V$  is the volume of space surveyed out to the actual distance of the object. For a complete sample of objects, uniformly distributed in Euclidean space, the expectation value of  $\langle V/V_m \rangle$ , is 0.5 with a formal  $1\sigma$  error of  $1/\sqrt{12N}$ , where  $N$  is the number of objects in the sample (Avni & Bahcall 1980).

Although in practice the WFC sample was selected on the basis of a significance threshold (*i.e.*  $2.5\sigma$  in the S1 band), here it is assumed that the sources represent a *count rate limited sample* with a threshold (at  $2.5\sigma$ ) of 10 S1 ct/ksec<sup>1</sup>. For the extragalactic sample  $\langle V/V_m \rangle = 0.54 \pm 0.07$ , implying that the above choice of count rate threshold is a reasonable one. The application of a K-S test to the distribution of the  $V/V_m$  values then gives  $P(> d) = 90\%$  (Avni & Bahcall 1980). On this basis it appears the sample shows no clear evidence for either strong evolution or incompleteness.

---

<sup>1</sup>PG 1415+451 has a measured S1 count rate that is actually below the nominal survey limit. In this one case  $V/V_m$  is set to 1.

Table 4.3: WFC Galactic sample

No.	Name	Type	S1 (ct/ks)	S2 (ct/ks)	RBSC (ct/s)	HR1 (7)	HR2 (8)	R.A. (J2000) (9)	Dec (J2000) (10)	Offset ( $''$ ) (11)	$N_H$ ( $10^{20} \text{ cm}^{-2}$ ) (12)
1	V777 Tau	F0	13±4	<17	0.56±0.06	-0.03±0.10	0.26±0.13	04 26 16.9	-37 57 30	47	2.0
2	H 0449-55	F5	41±8	<30	1.08±0.11	-0.20±0.09	0.12±0.15	04 53 30.2	-55 51 28	8	2.1
3	HD 77407	G0	30±8	<52	0.66±0.05	-0.21±0.07	0.01±0.12	09 03 26.8	37 50 32	90	2.4
4	DK Leo	K7	17±4	<14	0.51±0.51	-0.38±0.07	-0.02±0.14	10 14 19.3	21 04 37	43	2.4
5	EK UMa	CV	33±6	<13	1.11±0.04	-0.99±0.01	-1.00±0.01	10 51 35.3	54 04 37	52	1.0
6	CW UMa	M4	20±6	<9	0.37±0.04	-0.21±0.10	-0.20±0.16	11 11 51.8	33 32 13	39	2.1
7	HD 108102	F8	19±4	<17	0.60±0.04	-0.06±0.06	-0.09±0.08	12 25 01.8	25 33 41	10	1.8
8	SAO 632275	G6	10±3	<13	0.39±0.03	-0.23±0.07	0.13±0.12	12 58 34.7	38 16 41	20	1.4
9	GP Com	CV	17±5	<7	0.54±0.07	0.12±0.11	0.39±0.13	13 05 42.7	18 00 56	45	2.1
10	HD 114378	F5	17±5	<29	0.88±0.06	-0.38±0.06	-0.21±0.12	13 09 59.3	17 31 36	32	1.9
11	NGC 5272	GC	11±3	<10	0.57±0.04	-0.95±0.02	-0.12±0.56	13 42 10.2	28 22 50	56	1.2
12	AG +19 1315	K0	11±4	<10	0.55±0.06	0.03±0.09	0.41±0.12	14 01 58.2	19 25 39	57	2.4
13	HD 131511	K2	12±4	<15	0.36±0.03	-0.48±0.07	-0.29±0.17	14 53 24.3	19 09 15	65	2.5
14	Her X-1	XRB	93±8	<14	18.80±0.14	-0.37±0.01	0.11±0.01	16 57 49.6	35 20 33	33	1.8
15	HD 208496	F3	16±5	<37	0.54±0.04	-0.04±0.07	-0.31±0.10	21 58 31.6	-59 00 43	33	2.1

#### 4.4.2 Comparison with Previous EUV Studies

In total eight extragalactic sources (three NLS1 galaxies, two BLS1s and three BL Lac objects) are listed in the *ROSAT* WFC 2RE catalogue<sup>2</sup>. The 2RE catalogue employed a combined S1+S2 significance limit of  $\sigma_c \geq 5.5$ , where  $\sigma_c = \sqrt{\sigma_{S1}^2 + \sigma_{S2}^2}$ , and  $\sigma_{S1}$  and  $\sigma_{S2}$  are the significances of the detections in the two WFC filters. Since AGN are very unlikely to be detected in the S2 band, the 2RE survey was not optimized to find such sources. As noted earlier, the approach here has been to search much more deeply in the S1 band (i.e., to  $2.5\sigma$ ), whilst guarding against spurious detections by requiring a simultaneous detection in the soft X-ray band (at a level well above the threshold of the RBSC). The resulting sample of extragalactic sources, all of which are identified as AGN, is more than twice the size of that derived from 2RE catalogue.

The Extreme Ultraviolet Explorer (*EUVE*) has also conducted an extensive all-sky survey at EUV energies. Using *EUVE* survey data, Marshall, Fruscione & Carone (1995) compiled a list of 13 extragalactic sources detected by *EUVE* at  $\geq 2.5\sigma$ , eight of which appear in the current WFC sample. However, that study cross-correlated the *EUVE* data with catalogues of previously-known AGN. Since few NLS1s were known at that time, it is no surprise that this sample contains only three NLS1s (representing  $<25\%$  of the total, compared to almost 50% in the current sample). It therefore seems likely that the *EUVE* sample is incomplete and biased against NLS1s. A low-significance survey by Fruscione (1996) and Craig & Fruscione (1997) resulted in a large number of potential EUV detections of extragalactic sources. However, as recognised by the authors, a rather high fraction of these EUV sources may be spurious and even the bona fide EUV detections may represent chance coincidences with AGN (in the relatively large *EUVE* error circles) or arise due to the hard leak in the *EUVE* filters. The smaller error circles, the S2 discriminant and the sharper filter cutoff are all advantages of the WFC survey compared to that carried out by *EUVE*, at least in the narrow context of defining a complete EUV-selected sample of AGN. It must be emphasized that *all* of the identifications in the current WFC survey are very likely to be solid and secure.

---

<sup>2</sup>A ninth extragalactic source, the normal galaxy NGC 4787, was listed in the WFC 2RE catalogue. This identification is almost certainly spurious as the WFC source is detected only in the S2 band.

Table 4.4: Comparison of the WFC and *HEAO-1 A2* samples

	WFC	<i>HEAO-1 A2</i>
NLS1	8 (42%)	0 (0%)
BLS1/quasar	6 (32%)	27(78%)
Seyfert 2/NELG	0 (0%)	4 (11%)
BL Lac	5 (26%)	4 (11%)
Total	19 (100%)	35 (100%)
$\langle z \rangle$	0.079	0.035
Median redshift	0.050	0.019
$\langle HR1 \rangle$	-0.52	+0.47
$\langle HR2 \rangle$	-0.02	+0.28
$\langle V \rangle$	15.2	13.5

#### 4.4.3 Comparison with a Hard X-ray Selected Sample

It is interesting to compare the properties of the present sample selected in EUV band with those of a sample of AGN selected at much harder X-ray energies. For this purpose, the well-studied set of AGN derived from the 2–10 keV *HEAO-1 A2* survey (Piccinotti *et al.* 1982) is used. Table 4.4 compares certain properties of the WFC and *HEAO-1 A2* samples. Clearly there is quite a striking difference in the make-up of the AGN population as one moves up roughly a factor of 25 in energy. The *HEAO-1 A2* sample is dominated by BLS1s, and contains four narrow emission-line and Seyfert 2 galaxies, but *no* NLS1s. By comparison, almost half of the AGN in the EUV-selected WFC sample are NLS1s - this is yet another example of the relationship between optical emission line width and EUV/X-ray spectral properties - and the sample also contains a significantly higher proportion of BL Lacs, but no Seyfert 2s. The WFC objects are optically fainter and typically are at higher redshift than the *HEAO-1 A2* sources. Since the EUV sample was selected from a smaller region of sky (effectively  $\sim 31$  square degrees; see § 4.6), it is not unexpected that it was necessary to search to greater distances (and fainter magnitudes) in order to find comparable numbers of sources in the EUV band as contained in the *HEAO-1 A2* sample.

As noted earlier, the RBSC provides two measures of spectral hardness covering the 0.1–2.0 keV band, namely the ratios *HR1* and *HR2*. Fig. 4.3 shows a plot of *HR1* versus *HR2*, for both the present EUV-selected sample and the *HEAO-1 A2* sources. There is evidence of a correlation, indicating that sources that are characterized by a significant flux in the 0.1–0.4 keV band (i.e.,  $HR1 \lesssim 0$ ) also have rather steep spectra in the adjacent 0.5–2.0 keV band ( $HR2 \lesssim 0$ ), and vice-versa. There is very little overlap in *HR1* between the two samples, even though neither explicitly used any colour selection criteria. Again, this

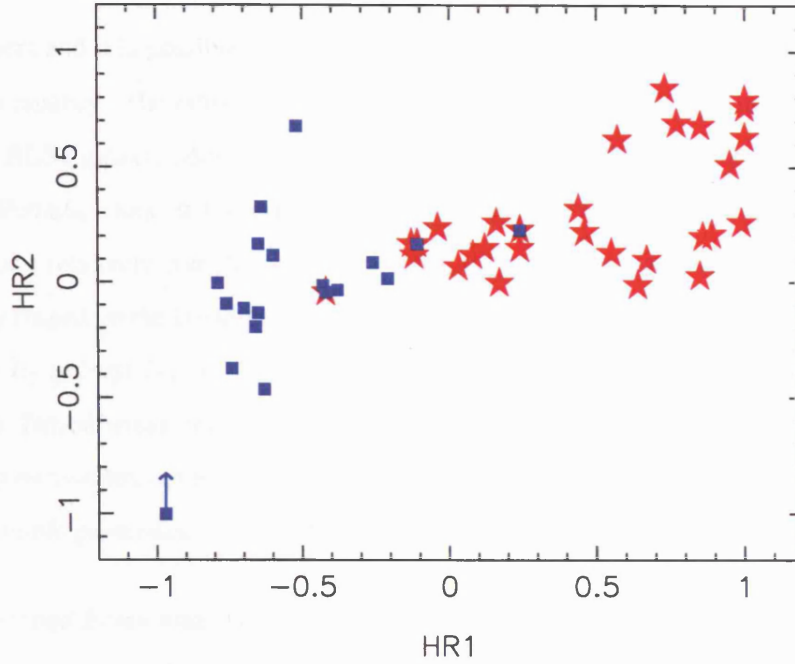


Figure 4.3: Plot of soft- and hard-band hardness ratios ( $HR1$  and  $HR2$ , respectively). A positive hardness ratio implies a flat (hard) spectrum. Squares refer to objects in the WFC sample and stars, to sources in the *HEAO-1 A2* sample. Three objects are common to both samples; they have coincident squares/stars. The NLS1 WPVS 007 is denoted by a square with an arrow to indicate a lower limit to its unmeasured  $HR2$ .

emphasizes how selection in the hard X-ray and EUV bands finds very different types of objects.

#### 4.4.4 The Spectral Form of the Sources

For each WFC source, measurements were available in four spectral channels, namely the WFC S1 band count rate and soft X-ray count rates measured by the *ROSAT* PSPC in the *C*, *H1* and *H2* bands (derived in an approximate way from the broad band, 0.1–2.4 keV count rate tabulated in the RBSC and the corresponding  $HR1$  and  $HR2$  hardness ratios; see § 4.3). These four channel data were modelled in terms of a simple power-law continuum with absorption corresponding to the foreground Galactic  $N_H$ . The energy index,  $\alpha_X$ , derived for each source is tabulated in Table 4.1.

In practice, the simple spectral model detailed above gave an unacceptable minimum  $\chi^2$  for six of the sources. However, when the constraints on the value  $N_H$  were relaxed, in each case a much better (and acceptable) fit was obtained. Interestingly all of these sources required an  $N_H$  in excess of the Galactic value in order to improve the fit (typically by an amount  $\Delta N_H \approx 5 \times 10^{19} \text{ cm}^{-2}$ ). Three of these sources

are BL Lac objects and it is possible to invoke spectral curvature (downwards below  $\sim 0.3$  keV) as the cause of the discrepancy. The other sources are IC 3599 and RE J1034+39, both of which are NLS1s, and LB 1727, a BLS1 galaxy. More detailed spectral fitting of IC 3599 (Brandt, Pounds & Fink 1995), RE J1034+39 (Pounds, Done & Osborne 1995) and LB 1727 (Turner *et al.* 1999a) is consistent with additional  $N_H$  or a relatively complex spectral form in these objects. Of course, the assumed value for the Galactic  $N_H$  (based on the broad-beam 21 cm measurements compiled by Dickey & Lockman 1990) may be in error by at least  $N_H \sim 10^{19} \text{ cm}^{-2}$  and possibly more in some instances (Elvis, Wilkes & Lockman 1989). Nevertheless, one conclusion is clear from the above analysis, namely that there is no evidence for any excess flux in the extreme ultraviolet band in the spectra of NLS1s (over and above that predicted by a simple power-law extrapolation of the soft X-ray spectrum).

Using the unabsorbed fluxes measured at 200 eV and an estimate of the optical flux at 5500 Å derived from the V-band magnitude, the optical/EUV spectral index,  $\alpha_{OE}$ , was calculated for each source (see Table 4.2) using the following formula:

$$\alpha_{OE} = -\log\left[\frac{F_\nu(200 \text{ eV})}{F_\nu(5500 \text{ Å})}\right] / \log\left[\frac{\nu(200 \text{ eV})}{\nu(5500 \text{ Å})}\right]$$

Figure 4.4 shows a plot of  $\alpha_X$  versus  $\alpha_{OE}$  for the AGN sample. An obvious point is that, apart from two objects, spectral slope in the soft X-ray band is generally steeper than the optical/EUV index. Specifically  $\langle\alpha_X\rangle = 2.0 \pm 0.9$  and  $\langle\alpha_{OE}\rangle = 1.0 \pm 0.3$  (where the error represents the standard deviation of the distribution). The implication is that many of these sources may contain a large hidden ultraviolet/EUV excess, possibly attributable to emission from the hotter inner regions of an accretion disc (e.g., Bechtold *et al.* 1987).

## 4.5 The Luminosity Function of EUV-Selected AGN

The catalogue of EUV-selected AGN represents the best sample of such sources presently available and, in principle, may be used to investigate the statistical properties of the extragalactic EUV-source population. In this section an approximate EUV luminosity function is derived and the relative contributions of the various types of AGN to the local ( $z \approx 0$ ) EUV volume emissivity is calculated.

The first step is to define the intrinsic luminosity of each source. For this purpose a standard spectral

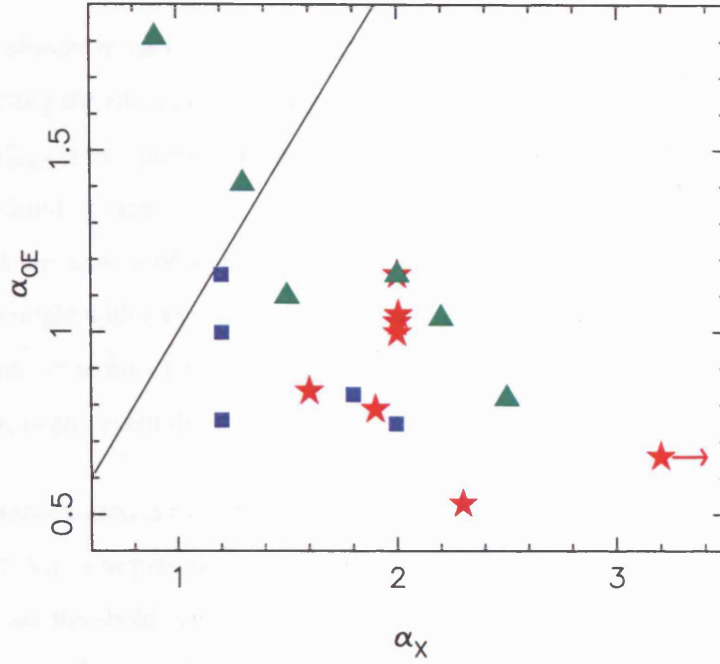


Figure 4.4: The soft X-ray spectral slope ( $\alpha_X$ ) versus the optical/EUV spectral index ( $\alpha_{OE}$ ) for the EUV-selected AGN sample. The stars correspond to NLS1s, the triangles to the BLS1s and the squares to the BL Lac objects. The dashed line corresponds to  $\alpha_{OE} = \alpha_X$ , as would be the case if the source was a pure power-law. The extreme NLS1, WPVS 7, has  $\alpha_X = 4.8$  and is denoted as the circle with an arrow (for an upper limit) in the lower right corner.

model consisting of a power-law continuum with  $\alpha_X$  fixed at 2 (i.e., close to the overall mean value for the sample) is employed. There was very little difference between this prescription and using the individual  $\alpha_X$  values tabulated in Table 4.1. Using this spectral form, together with the appropriate Galactic  $N_H$  and redshift, the observed S1 count rates for each source were converted to a *monochromatic* luminosity,  $L_{200}$ , measured at a rest-frame energy of 200 eV. The derived values of  $L_{200}$  are listed in Table 4.2. Allowing for the strong cut-off of the source spectra at low energies due to Galactic absorption, the selected energy of 200 eV is close to the typical photon energy recorded for this set of sources in the WFC S1 band. Similarly, a monochromatic luminosity was used since the typical effective detection bandwidth is very narrow (again as result of Galactic absorption). It is a matter of semantics as to whether the derived luminosities are referred to as EUV or ‘ultra-soft’ X-ray measurements.

The standard formula for calculating the luminosity function  $\Phi(L)$  of a sample of sources (e.g., Schmidt 1968) is:

$$\Phi(L) = \frac{1}{\Delta L} \sum_{i=1}^N \frac{1}{V_{max i}},$$

where there are  $N$  objects in each luminosity bin of width  $\Delta L$ , and  $V_{max_i}$  is the volume surveyed in the process of detecting the  $i$ th source. Because the  $V_{max}$  test was developed for a flux limited survey, the calculation of  $V_{max}$  is complicated in this instance by the fact that the WFC survey is significance limited (that is, the limiting flux is not constant from one part of the sky to another). Earlier (§ 4.4.1), it was assumed that the sample of sources could, at least to a first approximation, be represented as a *count-rate* limited sample with a threshold (at  $2.5\sigma$ ) of  $C_{lim} = 10$  S1 ct/ks. Since this prescription gave a reasonable outcome in terms of the  $\langle V/V_m \rangle$  test, the same approach was adopted in calculating the luminosity function; in any event the very limited source statistics most likely dominate the errors.

A second serious complication is that the transmission in the EUV band is a very strong function of the Galactic foreground  $N_H$ . The present approach of assuming a constant count rate threshold over the sky implies a variable flux threshold (when due allowance is made for the variable Galactic transmission), which in turn directly influences the survey volume. Specifically, for each source the following was calculated:

$$V_{max_i} = \int_0^{N_{Hlim}} \frac{1}{3} \Omega(N_H) \left( \frac{T(N_H)}{T(N_{H_i})} \right)^{\frac{3}{2}} d_i^3 \left( \frac{C_i}{C_{lim}} \right)^{\frac{3}{2}} dN_H,$$

where  $\Omega(N_H)$  is the differential solid angle of sky with a Galactic column density  $N_H$ ,  $T(N_H)$  is the Galactic EUV transmission as a function of  $N_H$ ,  $N_{H_i}$  is the Galactic column density in the direction of the source,  $N_{Hlim} = 2.5 \times 10^{20} \text{ cm}^{-2}$ ,  $C_i$  is the S1 count rate and  $d_i$  is the source distance.

The integral function, which accounts for the differing transmission over the survey area, can be separated to give:

$$V_{max_i} = \int_0^{N_{Hlim}} \Omega(N_H) T(N_H)^{\frac{3}{2}} dN_H \times \frac{1}{3} d_i^3 \left( \frac{C_i}{C_{lim}} \right)^{\frac{3}{2}} T(N_{H_i})^{-\frac{3}{2}}$$

The integral functions  $\int \Omega(N_H) dN_H$  and  $\int \Omega(N_H) T(N_H)^{\frac{3}{2}} dN_H$  are shown in Figure 4.5. For the present survey the latter integral, and hence area of sky effectively surveyed is  $1.2 \times 10^{-2}$  steradians or 39 square degrees (whereas integration of  $\Omega(N_H)$  between the same limits gives  $\sim 2.5$  steradians)<sup>3</sup>.

The luminosity function,  $\Phi(L_{200})$ , for the full sample of AGN (i.e., Seyfert galaxies plus BL Lac objects) was calculated from a binned representation of the data as shown in Figure 4.6. The plotted errors are

<sup>3</sup>The value given in Edelson *et al.* (1999) was underestimated by  $\sim 25\%$ .

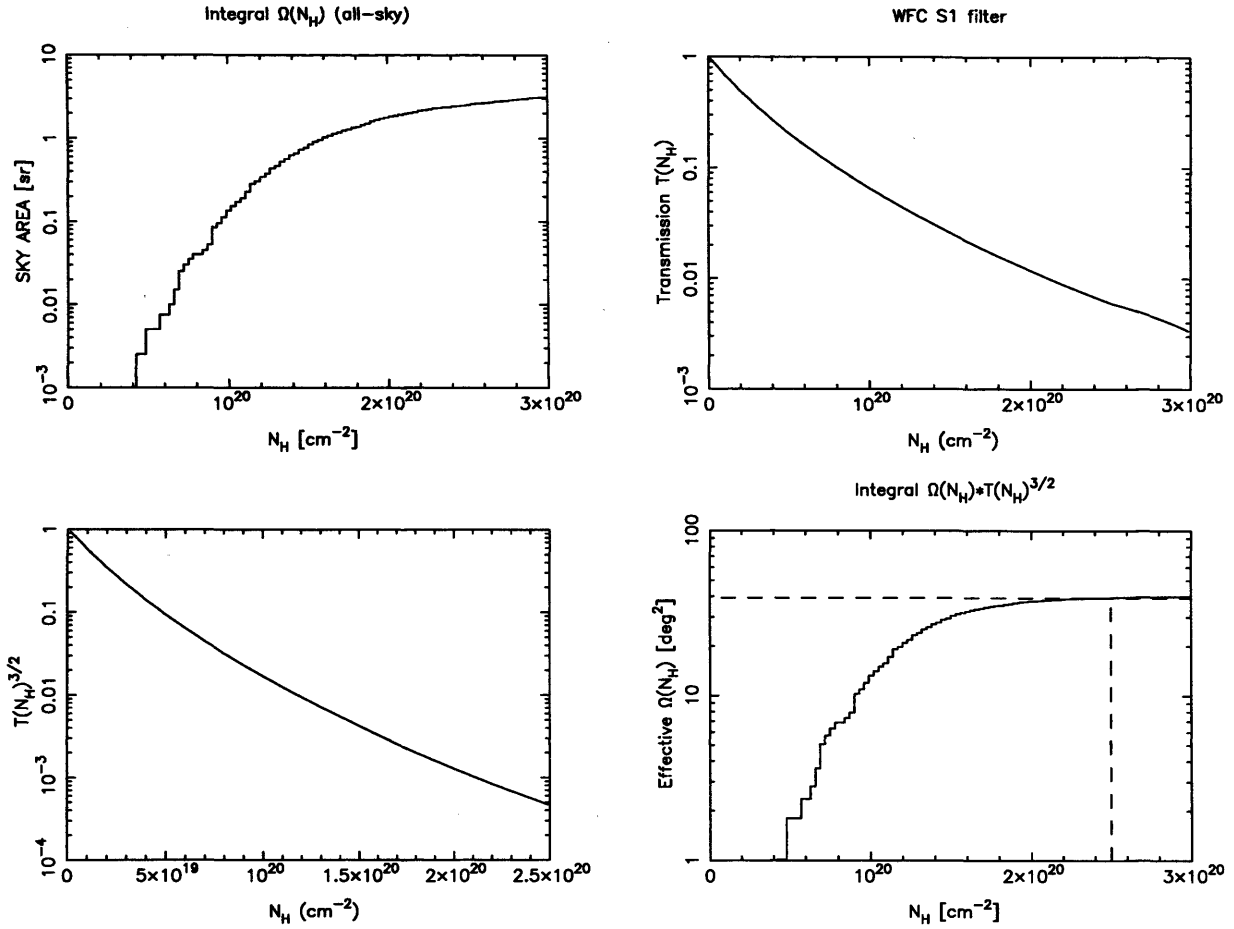


Figure 4.5: Cumulative form of the effective sky area function  $\Omega(N_H)T(N_H)^{\frac{3}{2}}$ . The dotted line shows the  $N_H$  limit used in this survey.

calculated using equation 10 of Marshall (1985) (see also Boyle, Shanks & Peterson 1988; Page & Carrera 2000). and, since they don't account for any possible systematic errors, should be considered as lower limits on the true errors. The three lower luminosity points in Figure 4.6 are consistent with the power-law form

$$\Phi(L_{200,44}) = 10^{-6} L_{200,44}^{-2} \text{ Mpc}^{-3} (10^{44} \text{ erg s}^{-1} \text{ keV}^{-1})^{-1}$$

where  $L_{200,44}$  is the monochromatic luminosity at a rest frame energy of 200 eV in units of  $10^{44} \text{ erg s}^{-1} \text{ keV}^{-1}$ . This rather flat luminosity function appears to cut off sharply in the highest luminosity bin (which contains only two sources, both of which are BL Lac objects).

The integrated volume emissivity (at  $z \approx 0$ ) has been estimated by summing the product of  $1/V_{max}$  and  $L_{200}$  over the sample of sources. A total emissivity of  $\sim 5 \times 10^{38} \text{ erg s}^{-1} \text{ keV}^{-1} \text{ Mpc}^{-3}$  was obtained

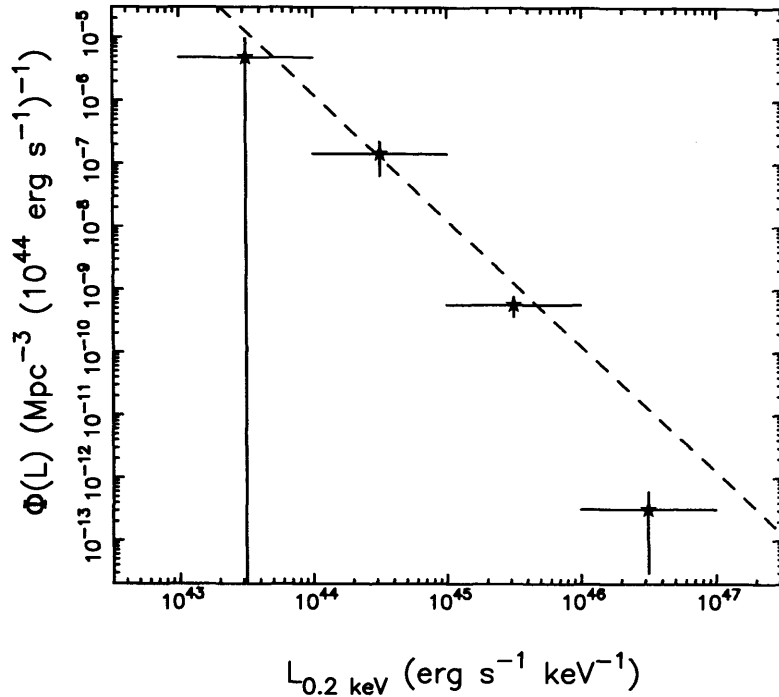


Figure 4.6: The EUV luminosity function of the AGN in the WFC sample. The monochromatic source luminosities are measured at 200 eV in the rest frame. The solid line represents the power-law function defined in the text. The first luminosity bin contains only one source, NGC 7213.

at 200 eV (which is close to the value obtained by integrating the above luminosity function between  $10^{43} - 10^{46}$  erg s $^{-1}$  keV $^{-1}$ ). The NLS1s contribute 50% of this emissivity, BLS1s 42%, and the BL Lac objects the remainder. This high contribution of NLS1s is in contrast to the situation at hard X-ray energies, where NLS1s make a negligible contribution to the volume emissivity (e.g., Piccinotti *et al.* 1982). However, it is interesting to note that a similar value for the volume emissivity at 200 eV can be obtained by extrapolating downward with a spectral slope  $\Gamma = 1.7$  from the 2–10 keV AGN volume emissivity derived from the *HEAO-1* A2 sample (Piccinotti *et al.* 1982).

The contribution of NLS1s to the volume emissivity at high redshift is probably of marginal significance (owing to the much higher total luminosity from quasars and star formation at high- $z$ ), but they be of some importance for studies of the local intergalactic ionising radiation field (e.g. Shull *et al.* 1999).

## Chapter 5

# A complete sample of soft X-ray selected AGN

### 5.1 Overview

A new sample of soft X-ray bright AGN is presented. The sample is selected on the basis of *ROSAT* C-band ( $\sim 0.25$  keV) count rate and is the first complete, count rate-limited sample in this ultrasoft band. The sample definition and source catalogues are given in the following section. Observations of the Seyfert sample are described in Section 5.3. Following this, correlations between various parameters are assessed in Section 5.4.2, outlying members of the sample are isolated in Section 5.4.3 and the luminosity function of the sample is presented in Section 5.4.4. Finally, Section 5.5 gives a brief discussion of these results.

### 5.2 Sample selection

The RBSC was used to deriving a new sample based on a count rate threshold in the 0.1-0.4 keV (i.e. 1/4 keV) *ROSAT* band. The three selection criteria used to construct a preliminary source list were as follows:

1. The 0.1–0.4 keV count rate  $C \geq 0.25$  ct s<sup>-1</sup>.
2. Galactic column  $N_H \leq 1.5 \times 10^{20}$  cm<sup>-2</sup> (using  $N_H$  measurements from Dickey & Lockman 1990).

3. Dec  $\delta \geq 0^\circ$ .

The PSPC C- and H-band (0.1–0.4 keV and 0.5–2.0 keV respectively) count rates,  $C$  and  $H$ , were derived in an approximate way from the RBSC hardness ratio ( $HR1 = (H - C)/(H + C)$ ) and full-band (0.1–2.4 keV) count rate  $T$ :

$$C \approx \frac{(1 - HR1)T}{2}$$

$$H \approx \frac{(1 + HR1)T}{2}$$

In practice this method recovered the correct values to within 0.01 ct/s compared to the values published in Schwobe *et al.* (2000). Criteria (2) and (3) delimit the survey area to regions around the Lockman Hole (Lockman, Jahoda & McCammon 1986) totalling  $\sim 0.6$  sr ( $\sim 5\%$  of the sky). Selection in terms of line-of-sight column is crucial; the  $N_H$  limit of  $1.5 \times 10^{20} \text{ cm}^{-2}$  corresponds to a transmission of  $\sim 0.14$  (or a foreground optical depth  $\tau \approx 2$ ) in the 0.1–0.4 keV band. The total number of X-ray sources satisfying the above criteria is 110.

The initial classification of the X-ray sources in the source list was based on the optical identifications of Schwobe *et al.* (2000) together with information obtained from the SIMBAD<sup>1</sup> and NED<sup>2</sup> on-line catalogues. This analysis showed that the 110 X-ray sources comprise 27 Galactic objects (3 cataclysmic variable stars, 6 white dwarfs, 17 active coronal stars and one super-soft source) and 83 extragalactic objects (54 Seyfert galaxies or quasars, 25 BL Lac objects, 4 clusters of galaxies). Table 5.1 shows the Seyfert subsample, which is the focus of the present work, but for completeness the full lists of non-Seyfert sources are also presented. Table 5.2 lists the BL Lacertae objects and Clusters and Table 5.3 lists the subsample of Galactic objects.

In Table 5.1 the columns provide the following information: (2) The source name; (3) optical type (see § 5.4.1); (4) the redshift; (5) and (6) the right ascension and declination as tabulated in the RBSC; (7) the full-band count rate; (8) hardness ratio; (9) an X-ray slope (derived as in section 4.4.4); (10) Galactic column density; (11) and (12) derived C- and H-band count rates; (13) optical V-band magnitude; (14)

<sup>1</sup><http://simbad.u-strasbg.fr/Simbad>

<sup>2</sup><http://nedwww.ipac.caltech.edu/>

Table 5.1: The Seyfert galaxy sample.

No	Name	Type	$z$	R.A. (J2000)	Dec. (J2000)	$T$ (ct/s)	$HR1$	$\alpha_X$	$N_H$ ( $10^{20} \text{ cm}^{-2}$ )	$C$ (ct/s)	$H$ (ct/s)	$m_V$	Ref
(1)	(2)	(3)	(4)	(5)	(6)	(7)	(8)	(9)	(10)	(11)	(12)	(13)	(14)
1	1E 0919+515	NLS1	0.161	09 22 46	51 20 46	0.42±0.03	-0.69±0.05	2.2	1.43	0.354	0.065	17.9	L, St
2	Mrk 110	BLS1	0.035	09 25 12	52 17 16	1.69±0.06	-0.19±0.03	1.2	1.47	1.006	0.685	16.0	BG92
3	US 0656	S1	0.160	09 30 17	47 07 25	0.46±0.03	-0.24±0.07	1.4	1.47	0.283	0.173	16.5	-
4	PG 0953+414	BLS1	0.234	09 56 52	41 15 24	0.95±0.06	-0.55±0.04	1.6	0.79	0.735	0.213	14.5	BG92
5	IRAS 10026	BLS1	0.178	10 05 42	43 32 44	0.66±0.04	-0.61±0.04	1.8	1.08	0.534	0.129	16.5	G
6	RX J1008+46	BLS1	0.388	10 08 30	46 29 57	0.42±0.03	-0.33±0.07	1.2	0.91	0.278	0.140	18.9	W
7	Ton 1187	BLS1	0.07	10 13 03	35 51 31	1.38±0.06	-0.44±0.03	1.7	1.38	0.992	0.386	17.4	G
8	RX J1019+37	NLS1	0.133	10 19 00	37 52 49	0.78±0.04	-0.07±0.05	1.0	1.38	0.415	0.360	15.0	W
9	Mrk 141	BLS1	0.042	10 19 12	63 58 02	0.51±0.04	-0.44±0.06	1.6	1.24	0.364	0.142	15.4	G
10	Mrk 142	NLS1	0.045	10 25 31	51 40 39	1.75±0.06	-0.61±0.02	1.9	1.14	1.406	0.341	16.1	G, L
11	RX J1026+55	BLS1	0.119	10 26 52	55 09 13	0.37±0.03	-0.63±0.05	2.0	0.80	0.304	0.069	17.7	W
12	RE J1034+396	NLS1	0.042	10 34 38	39 38 34	2.66±0.09	-0.74±0.02	2.2	1.02	2.312	0.346	15.6	P
13	RX J1046+52	BLS1	0.499	10 46 14	52 56 00	0.32±0.03	-0.82±0.04	2.6	1.08	0.293	0.029	17.5	W
14	RX J1050+55	BLS1	0.331	10 50 55	55 27 31	0.37±0.03	-0.69±0.05	2.0	0.77	0.316	0.058	17.0	W, G
15	RX J1054+48	BLS1	0.266	10 54 44	48 31 45	0.45±0.03	-0.36±0.06	1.5	1.23	0.309	0.145	15.7	W
16	EXO 1055+60	BLS1	0.150	10 58 30	60 16 02	0.39±0.03	-0.76±0.04	2.0	0.61	0.342	0.047	17.0	G
17	RX J1117+65	BLS1	0.147	11 17 10	65 22 10	0.55±0.03	-0.72±0.03	2.0	1.00	0.469	0.076	16.7	G
18	PG 1116+21	BLS1	0.177	11 19 08	21 19 14	1.03±0.06	-0.48±0.05	1.7	1.28	0.759	0.267	15.2	G
19	EXO 1128+691	NLS1	0.043	11 31 05	68 51 55	1.58±0.05	-0.43±0.02	1.6	1.32	1.129	0.450	16.5	Be
20	RX J1138+57	BLS1	0.116	11 38 49	57 42 45	0.58±0.04	-0.48±0.06	1.6	1.09	0.428	0.150	16.5	W
21	NGC 4051	NLS1	0.002	12 03 08	44 31 54	3.92±0.11	-0.45±0.02	1.7	1.32	2.841	1.077	10.8	L
22	RX J1209+32	NLS1	0.145	12 09 46	32 17 02	0.57±0.06	-0.62±0.09	1.9	1.06	0.458	0.107	17.7	W
23	RX J1226+32	BLS1	0.243	12 26 23	32 44 30	0.37±0.03	-0.38±0.07	1.6	1.41	0.255	0.114	17.2	W
24	RX J1232+49	NLS1	0.262	12 32 20	49 57 31	0.34±0.03	-0.60±0.07	2.0	1.31	0.272	0.068	17.0	W
25	Ton 83	NLS1	0.29	12 33 41	31 01 03	0.50±0.03	-0.52±0.05	1.8	1.35	0.378	0.119	16.2	S
26	MCG +08-23-067	NLS1	0.03	12 36 51	45 39 06	0.53±0.04	-0.27±0.06	1.3	1.37	0.334	0.192	16.0	W
27	IC 3599	NLS1/S2	0.022	12 37 41	26 42 29	5.10±0.11	-0.63±0.01	2.0	1.29	4.152	0.943	15.6	S, G

No	Name	Type	$z$	R.A. (J2000)	Dec. (J2000)	$T$ (ct/s)	$HR1$	$\alpha_X$	$N_H$ ( $10^{20} \text{ cm}^{-2}$ )	$C$ (ct/s)	$H$ (ct/s)	$m_V$	Ref
(1)	(2)	(3)	(4)	(5)	(6)	(7)	(8)	(9)	(10)	(11)	(12)	(13)	(14)
28	Was 61	BLS1	0.044	12 42 11	33 17 03	0.86±0.04	-0.27±0.04	1.1	1.33	0.545	0.313	15.4	S, G
29	RX J1244+58	NLS1	0.198	12 44 41	58 56 29	0.33±0.04	-0.78±0.05	2.1	1.21	0.293	0.036	18.0	W
30	RX J1258+23	BLS1	0.075	12 58 51	23 55 32	0.43±0.03	-0.38±0.06	1.5	1.30	0.297	0.133	17.0	W
31	RX J1312+26	BLS1	0.06	13 12 59	26 28 25	0.42±0.04	-0.41±0.07	1.4	1.05	0.295	0.123	16.8	S, G
32	Ton 1571	NLS1	0.075	13 14 22	34 29 40	0.65±0.04	-0.63±0.04	1.9	0.99	0.530	0.120	16.3	S
33	RX J1319+52	NLS1	0.092	13 19 57	52 35 33	0.66±0.04	-0.52±0.05	1.7	1.19	0.504	0.159	17.3	W
34	RX J1328+24	BLS1	0.223	13 28 20	24 09 27	0.32±0.03	-0.66±0.07	2.0	1.16	0.261	0.053	17.7	W
35	IRAS 13349+243	BLS1	0.108	13 37 18	24 23 06	2.53±0.09	-0.65±0.02	2.0	1.16	2.085	0.442	15.0	S
36	RX J1339+40	NLS1	0.118	13 39 28	40 32 29	0.35±0.03	-0.58±0.06	1.7	0.87	0.276	0.073	17.7	W
37	RX J1342+38	BLS1	0.176	13 42 31	38 29 08	0.37±0.03	-0.37±0.06	1.5	0.91	0.250	0.115	18.0	W
38	PG 1341+25	BLS1	0.087	13 43 56	25 38 45	0.50±0.04	-0.56±0.06	1.8	1.09	0.393	0.111	16.6	W
39	Mrk 663	S2	0.026	13 54 20	32 55 47	0.84±0.05	0.36±0.05	0.4	1.24	0.267	0.568	14.6	S
40	RX J1355+56	BLS1	0.122	13 55 15	56 12 44	0.55±0.06	-0.55±0.08	1.8	1.13	0.423	0.123	17.1	S, G
41	PG 1402+261	BLS1	0.164	14 05 16	25 55 36	0.65±0.04	-0.54±0.05	1.9	1.47	0.500	0.149	15.6	S, L
42	PG 1415+451	BLS1	0.114	14 17 00	44 55 56	0.50±0.03	-0.66±0.03	2.0	1.22	0.413	0.085	15.7	S, L
43	RX J1426+39	S1	0.081	14 26 30	39 03 48	0.36±0.03	-0.54±0.05	1.6	0.93	0.279	0.083	16.0	-
44	Mrk 684	NLS1	0.046	14 31 04	28 17 16	0.58±0.04	-0.23±0.06	1.4	1.48	0.355	0.222	15.2	S
45	Mrk 478	NLS1	0.079	14 42 07	35 26 32	5.78±0.10	-0.70±0.01	2.1	1.03	4.916	0.867	15.0	G, L
46	PG 1444+407	BLS1	0.267	14 46 45	40 35 10	0.34±0.03	-0.57±0.05	1.8	1.25	0.269	0.074	16.0	S
47	RX J1448+35	BLS1	0.113	14 48 25	35 59 55	0.37±0.03	-0.71±0.06	2.1	1.07	0.312	0.053	16.4	W
48	NGC 5905	H II	0.011	15 15 23	55 30 57	0.31±0.02	-0.99±0.01	3.6	1.44	0.308	0.002	12.5	S
49	RX J1529+56	BLS1	0.099	15 29 07	56 16 04	0.74±0.03	-0.43±0.03	1.7	1.29	0.531	0.212	15.8	W
50	MCG +06-36-003	BLS1	0.070	16 13 01	37 16 56	0.42±0.03	-0.31±0.06	1.4	1.24	0.272	0.143	15.5	W
51	RX J1618+36	NLS1	0.034	16 18 09	36 19 50	0.85±0.03	-0.43±0.03	1.6	1.28	0.608	0.242	16.9	S, G
52	RX J1619+40	BLS1	0.038	16 19 51	40 58 34	0.51±0.03	-0.54±0.04	1.6	0.93	0.393	0.117	16.0	S, W
53	RX J1629+40	BLS1	0.272	16 29 01	40 07 53	0.79±0.03	-0.79±0.02	2.3	0.85	0.702	0.082	19.0	S
54	RX J1646+39	NLS1	0.10	16 46 25	39 29 21	0.40±0.03	-0.42±0.06	1.6	1.31	0.281	0.115	17.1	S, G

Table 5.2: The BL Lac and cluster samples. The columns provide the following information: (2) The source name; (3) the source type; (4) the redshift; (5) and (6) the right ascension and declination as tabulated in the RBSC; (7) the full-band count rate; (8) the hardness ratio  $HR1$ ; (9) the Galactic column; (10) and (11) the derived C- and H-band count rates.

No	Name	Type	$z$	R.A. (J2000)	Dec. (J2000)	$T$ (ct/s)	$HR1$	$N_H$ ( $10^{20} \text{ cm}^{-2}$ )	$C$ (ct/s)	$H$ (ct/s)
(1)	(2)	(3)	(4)	(5)	(6)	(7)	(8)	(9)	(10)	(11)
1	1ES 0927+5	BL Lac	0.190	09 30 37	49 50 28	2.15±0.07	0.06±0.03	1.40	1.012	1.142
2	RX J1008+47	BL Lac	0.343	10 08 11	47 05 26	1.10±0.05	-0.29±0.04	0.88	0.711	0.392
3	B3 1009+427	BL Lac	0.364	10 12 44	42 29 58	0.66±0.04	0.02±0.05	1.09	0.325	0.339
4	GB 1011+496	BL Lac	0.2	10 15 04	49 26 04	1.94±0.07	-0.38±0.03	0.79	1.340	0.602
5	RX J1016+41	BL Lac	0.281	10 16 16	41 08 17	0.48±0.03	-0.08±0.06	1.14	0.259	0.221
6	1ES 1028+511	BL Lac	0.361	10 31 18	50 53 40	4.46±0.09	-0.26±0.02	1.17	2.812	1.652
7	87GB 10553	BL Lac	0.144	10 58 37	56 28 16	0.46±0.03	-0.48±0.05	0.67	0.340	0.119
8	FIRST J110	BL Lac	–	11 00 21	40 19 33	0.61±0.04	-0.35±0.06	1.16	0.410	0.198
9	Mrk 421	BL Lac	0.03	11 04 27	38 12 31	26.57±0.28	-0.21±0.01	0.71	16.075	10.495
10	87GB 11051	BL Lac	–	11 07 48	15 02 17	0.45±0.04	-0.19±0.08	1.49	0.270	0.184
11	87GB 11429	BL Lac	0.138	11 17 06	20 14 10	4.34±0.12	-0.01±0.02	1.36	2.191	2.147
12	Mrk 180	BL Lac	0.046	11 36 26	70 09 32	4.53±0.08	-0.20±0.01	1.42	2.719	1.813
13	87GB 11333	BL Lac	0.135	11 36 30	67 37 08	1.91±0.06	0.07±0.03	1.35	0.886	1.020
14	Ton 116	BL Lac	–	12 43 12	36 27 42	1.30±0.05	-0.36±0.03	1.36	0.882	0.415
15	PG 1246+586	BL Lac	–	12 48 18	58 20 31	0.52±0.04	-0.42±0.06	1.12	0.366	0.150
16	1ES 1255+244	BL Lac	0.141	12 57 31	24 12 45	0.93±0.05	-0.10±0.05	1.26	0.513	0.420
17	RX J1302+50	BL Lac	0.688	13 02 55	50 56 21	0.52±0.04	-0.05±0.06	1.18	0.274	0.248
18	RX J1341+39	BL Lac	0.163	13 41 04	39 59 42	0.76±0.04	-0.10±0.04	0.80	0.416	0.340
19	RX J1420+53	BL Lac	–	14 20 24	53 34 03	0.29±0.02	-0.92±0.03	1.18	0.275	0.011
20	RX J1442+58	BL Lac	0.638	14 22 39	58 01 59	2.0±0.06	-0.09±0.02	1.32	1.090	0.910
21	H 1426+428	BL Lac	0.129	14 28 32	42 40 28	4.20±0.09	-0.06±0.02	1.38	2.228	1.975
22	PG 1437+398	BL Lac	–	14 39 17	39 32 48	1.43±0.05	-0.35±0.03	1.05	0.966	0.465
23	[WB92] 144	BL Lac	–	14 48 01	36 08 33	0.60±0.04	-0.54±0.05	1.05	0.460	0.137
24	1ES 1533+535	BL Lac	0.89	15 35 01	53 20 42	1.43±0.04	0.00±0.02	1.32	0.716	0.716
25	RX J1631+42	BL Lac	0.468	16 31 24	42 16 56	0.53±0.03	-0.07±0.04	1.04	0.282	0.245
1	ABELL 1656	Cluster	0.023	12 59 47	27 56 35	11.70±0.13	0.33±0.05	0.92	3.920	7.781
2	ABELL 1795	Cluster	0.062	13 48 52	26 35 40	3.77±0.09	0.28±0.02	1.19	1.358	2.415
3	ABELL 1914	Cluster	0.171	14 26 01	37 49 35	0.91±0.04	0.25±0.04	0.95	0.342	0.571
4	ABELL 2129	Cluster	0.030	16 28 37	39 32 48	4.5±0.08	0.30±0.01	0.86	1.575	2.925

Table 5.3: The Galactic sample. The columns provide the following information: (2) the source name; (3) and (4) the right ascension and declination as tabulated in the RBSC; (5) the full-band count rate; (6) hardness ratio; (7) Galactic column; (8) and (9) derived C- and H-band count rates; (10 and (11) the source type and optical magnitude (V-band where available).

No.	Name	R.A. (J2000)	Dec (J2000)	$T$ (ct/s)	$HR1$	$N_H$ ( $10^{20} \text{ cm}^{-2}$ )	$C$ (ct/s)	$H$ (ct/s)	Type	Mag
(1)	(2)	(3)	(4)	(5)	(6)	(7)	(8)	(9)	(10)	(11)
1	HD76943 B	09 00 38	41 47 02	0.68±0.05	-0.46±0.05	1.29	0.493	0.183	F5V	4.0
2	HR 3922	09 57 12	57 25 12	0.62±0.03	0.09±0.05	1.08	0.280	0.336	G5III	6.0
3	G 196-3	10 04 21	50 23 17	0.69±0.04	-0.26±0.05	0.82	0.434	0.255	M3Ve	13.3
4	RE J1032+53	10 32 10	53 29 40	5.07±0.10	-1.00±0.00	1.16	5.069	0.000	WD/DA	14.5
5	RE J1043+49	10 43 11	49 02 27	0.93±0.05	-1.00±0.00	1.32	0.930	0.000	WD	16.1
6	FH Uma	10 47 10	63 35 22	0.26±0.02	-0.97±0.01	1.06	0.253	0.004	CV/AM Her	19.4
7	EK Uma	10 51 35	54 04 37	1.11±0.05	-0.99±0.00	0.98	1.103	0.006	CV/AM Her	18.0
8	DM Uma	10 55 43	60 28 10	0.90±0.04	-0.19±0.04	0.68	0.534	0.363	K0/RSCVN	9.3
9	LB 1919	10 59 16	51 24 52	4.18±0.09	-0.99±0.00	1.06	4.159	0.021	WD/DA	16.8
10	HD 95559	11 02 02	22 35 46	1.01±0.07	0.01±0.07	1.41	0.498	0.509	G5III	8.9
11	AN Uma	11 04 25	45 03 19	1.77±0.07	-0.94±0.01	1.11	1.718	0.053	CV/AM Her	15.5
12	Ton 61	11 12 38	24 09 09	0.61±0.05	-0.96±0.03	1.23	0.596	0.012	WD/DA	15.1
13	PG 1234+48	12 36 45	47 55 30	1.45±0.06	-1.00±0.00	1.19	1.451	0.000	WD/sd:B	14.4
14	31 Com	12 51 42	27 32 21	1.11±0.09	0.31±0.07	0.90	0.382	0.724	G0IIIp	4.9
15	Gl 490	12 57 40	35 13 34	0.84±0.04	-0.22±0.04	1.23	0.511	0.327	M0.5e	10.3
16	RS CVn	13 10 36	35 56 04	0.89±0.04	0.04±0.04	1.03	0.425	0.461	F4v+RSCVn	8.2
17	HZ 43	13 16 21	29 05 55	72.84±0.32	-0.99±0.00	1.08	72.470	0.364	WD/DA	12.7
18	HD 116204	13 21 32	38 52 49	1.32±0.05	0.22±0.03	0.97	0.513	0.803	G8III/RSCVn	7.3
19	GJ 3789	13 31 46	29 16 31	0.41±0.03	-0.32±0.07	1.16	0.271	0.139	M4	12.0
20	BD +23 258	13 32 41	22 30 07	0.84±0.05	-0.13±0.05	1.44	0.477	0.367	KV	9.6
21	HR 5110	13 34 47	37 10 59	2.77±0.08	-0.07±0.02	0.92	1.481	1.287	F2IV/RSCVn	4.9
22	RX J1342+28	13 42 10	28 22 50	0.58±0.04	-0.95±0.02	1.14	0.561	0.014	SSS/Glob Cl	-
23	HD 123351	14 06 26	30 50 51	0.81±0.05	0.00±0.05	1.25	0.405	0.405	K0	7.6
24	HR 5404	14 25 11	51 51 09	2.00±0.06	0.02±0.02	1.29	0.978	1.018	F7V	4.1
25	RX J1605+54	16 05 18	54 21 01	0.50±0.02	-0.11±0.04	1.23	0.278	0.223	M	19.1
26	HD 146696	16 15 43	44 33 10	0.58±0.04	0.07±0.06	1.15	0.271	0.312	G0	8.9
27	GJ 9557A	16 19 55	39 42 23	0.64±0.03	-0.16±0.04	0.93	0.371	0.269	F0V	5.5

reference for the optical information (W indicates WHT data and S indicates Shane data - see section 5.3, Be indicates data from Bedford, Vilhu & Petrov (1988), BG92 from Boroson & Green (1992), G from Grupe *et al.* (1999), L from Lipari, Terlevich & Macchetto (1993), P from Puchnarewicz *et al.* (1995), St from Stephens (1989)). The tabulated information is derived from the published RBSC data (e.g., Voges *et al.* 1999 and Schwobe *et al.* 2000) except for the Galactic  $N_H$  (Dickey & Lockman 1990).

### 5.2.1 Sample completeness

The completeness of the sample was checked using the  $\langle V/V_{max} \rangle$  test of Schmidt (1968). For the Seyfert sample  $\langle V/V_{max} \rangle = 0.52 \pm 0.04$  indicating no evidence for either strong evolution or incompleteness. The BL Lac sample (Table 5.2) shows evidence for either incompleteness or negative evolution, with  $\langle V/V_{max} \rangle = 0.37 \pm 0.06$ . This effect has been seen in previous samples of X-ray selected BL Lacs, first in the *Einstein* Medium Sensitivity Survey (Maccacaro *et al.* 1984) and also in *ROSAT* selected samples (Bade *et al.* 1998), and may be due to cosmological evolution of some subset of the BL Lac population.

The Galactic sample has  $\langle V/V_{max} \rangle = 0.38 \pm 0.06$ . This apparent incompleteness is most likely due to the source populations falling below the Euclidean prediction at distances comparable to the scale height of the Galactic disc. In order to check this, distance estimates for 17 of the sources were taken from the literature (e.g., Strassmeier *et al.* 1993; Vennes *et al.* 1997) or derived from the distance moduli of the stars with well-known spectral type. The mean distance to the ten main sequence stars with known distances is  $\sim 90$  pc, and the mean distance to the older stars (white dwarfs, RS CVn systems) is  $\sim 180$  pc. These are comparable to the scale heights of the *young thin disc* of the Galaxy ( $\sim 100$  pc) and the *old thin disc* ( $\sim 300$  pc), respectively (e.g., Haywood, Robin & Creze 1997; Vallenari, Bertelli & Schmidtbreick 2000 and references therein).

## 5.3 Optical observations of the Seyfert sample

In order to measure the optical properties of the *complete* sample of Seyfert galaxies, new optical spectra have been acquired for 38 of the 54 objects listed in Table 5.1 (labelled as W or S in column 14 of the Table). These data, when combined with the previously published optical work and non-simultaneous *ROSAT* survey data, provide detailed information about the properties of the Seyfert sample.

The new optical spectra were obtained with the 4.2m William Herschel Telescope (WHT) at the Observatorio Roque de los Muchachos on the Island of La Palma, on the nights of 1999 March 21 and 22, and with the 3.0m Shane Telescope at Lick Observatory, Mt. Hamilton, California from 1999 May 21–23.

The WHT observations used the ISIS spectrograph<sup>3</sup> with the R300B grating and a EEV 42 CCD camera on the blue arm and the R158R grating with a TEK 2 CCD camera on the red arm. The combination of blue and red spectra provided coverage from 3600Å to 9000Å. The Shane data were obtained with the Kast spectrograph<sup>4</sup> using grism #2 and grating #6 in the blue and red arms respectively, both with Reticon 1200x400 CCD cameras. This set-up provided similar wavelength coverage (3500Å–9000Å) to the WHT data.

The data were extracted following standard procedures using IRAF<sup>5</sup>. Individual frames were bias subtracted and flat-field corrected. Spectra were traced on the CCD using a low-order polynomial and then optimally extracted (Horne 1986) using a variable extraction slit-width (typically 4"). Background regions for sky subtraction were located where possible either side of the target spectrum. Sky-line and cosmic ray removal occurs during the extraction procedure. Extracted spectra were wavelength calibrated, corrected for atmospheric extinction and flux calibrated by comparison with a photometric standard.

Multiple exposures of the same object were combined where possible prior to extraction in order to increase the signal-to-noise ratio and help remove cosmic ray contamination. However, this was not possible in cases where only one exposure was taken or when target source image moved across the CCD chip between exposures, in which case the data were extracted separately from each frame and then combined.

The absolute fluxes of the separate blue and red spectra for each object generally match to within 10 per cent. One source, RX J1619+40, was observed at both observatories to allow a test of the flux calibration. The two sets of spectra match to within 20 per cent over the useful wavelength range. Given that the source may have varied between the two observations (separated by 2 months) it seems reasonable to conclude that the absolute flux calibration of these data are good to within 20 per cent, a value which is typical of optical spectroscopy obtained under non-photometric conditions. The spectral resolution of the data were estimated from fits to the intrinsically narrow arc lamp lines. For the WHT data the blue

---

<sup>3</sup>See [http://www.ing.iac.es/~bgarcia/isis\\_new/isis\\_home.html](http://www.ing.iac.es/~bgarcia/isis_new/isis_home.html)

<sup>4</sup>See [http://www.ucolick.org/~mountain/mthamilton/techdocs/instruments/kast/kast\\_index.html](http://www.ucolick.org/~mountain/mthamilton/techdocs/instruments/kast/kast_index.html)

<sup>5</sup>IRAF is the Image Reduction and Analysis Facility and is written and supported by the IRAF programming group at the National Optical Astronomy Observatories (NOAO) in Tucson, Arizona. See <http://iraf.noao.edu/iraf/web/>

spectra have a FWHM  $\sim 3.5 \text{ \AA}$  and the red have FWHM  $\sim 5 \text{ \AA}$ , the Shane data have FWHM of  $4 \text{ \AA}$  and  $8 \text{ \AA}$  in the blue and red respectively. These correspond to a velocity width  $\sim 200 \text{ km/s}$  at [O III]  $\lambda 5007$ .

Before any measurements were taken from the optical data, the red and blue spectra for each object were combined into one spectrum. The data were convolved with a Gaussian (of width smaller than the spectral resolution) in order to smooth out any remaining bad pixels (but without degrading the spectral resolution). The blue data were then scaled to match the flux of the red data in the region of overlap, which was typically  $350 \text{ \AA}$  wide for the Shane data but only  $\lesssim 100 \text{ \AA}$  for the WHT data. (The red data were chosen as the flux norm simply because the signal-to-noise is higher in the red arm than it is in the blue.) The data were then combined and averaged in the overlap region to produce a single, continuous blue-red spectrum.

Due to the small overlap between blue and red spectra in the WHT observations, the normalisation between blue and red is rather less accurate than in the case of the Shane data, and forcing continuity between blue and red may introduce a systematic error in the shape of the spectrum in the overlapping region. For most sources this has no effect on the derived spectral properties, but if, as in the case of RX J1054+48, the  $H\beta$  line falls in the overlap region then the detailed profile of the line will be distorted somewhat. This is unavoidable as the line falls at the far end of each spectrum, where the calibration is worst, and the small overlap means that neither spectrum contains the complete line profile.

The optical spectra were used to measure the basic optical properties of each object. Redshifts were obtained from the identification papers or derived from fitting a Gaussian to the upper half of the observed [O III]  $\lambda 5007$  line in each spectrum. (The centroid of a Gaussian fit and the line peak were generally consistent within the limits set by the spectral resolution of the data.)

### 5.3.1 Fe II subtraction

In many of these spectra there is a clear contribution from blends of Fe II line emission on both the blue and red sides of the  $H\beta$  - [O III] complex. An automatic fitting routine developed by Goad (2001) (based on the method of Boroson & Green 1992) was used to estimate the strength of these lines, and remove any Fe II contamination from the  $H\beta$  region. (This method was also used by Grupe *et al.* 1999, although in that analysis the width of Fe II was fixed to be the same as  $H\beta$ ).

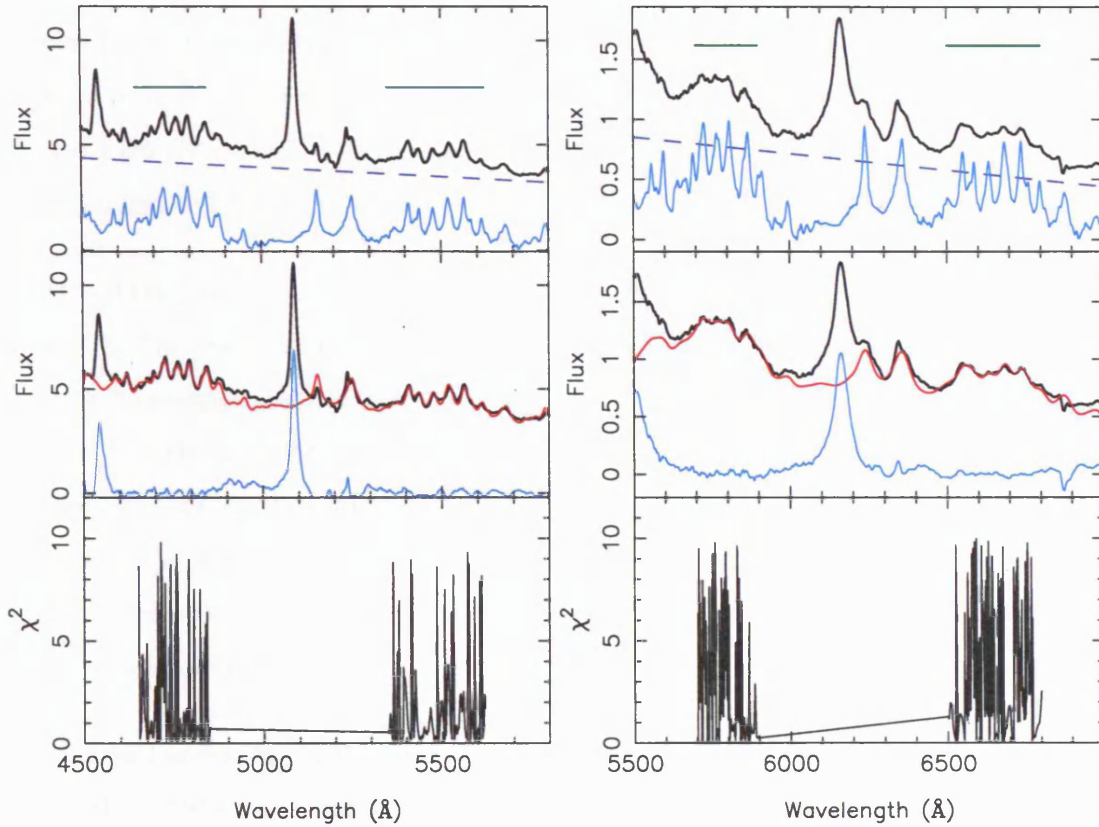


Figure 5.1: Examples of the Fe II subtraction procedure. The left hand panels show data for Mrk 684, an NLS1, while the right-hand panels show data for the broad-line Seyfert 1 PG 1444+407. The top-most panels show the spectrum centred around  $H\beta$  (thick black line), the 1 Zw I template shifted to the redshift of the source (cyan), the best-fit continuum (dashed line) and the regions over which  $\chi^2$  is calculated (green). The middle panels show the best-fit continuum plus Fe II model (red) overlaid on the data (black), and the data minus the model (cyan). The lower panels show the  $\chi^2$  values over the fit regions. The fluxes are in units of  $10^{-15} \text{ erg s}^{-1} \text{ cm}^{-2} \text{ \AA}^{-1}$ .

The method involves comparing a template optical Fe II line spectrum with the observed spectra. The template used in the present work was the same as that of Boroson & Green (1992), namely the Fe II lines of the bright NLS1 I Zw 1, which shows very strong and narrow permitted Fe II emission (e.g., Phillips 1978; Oke & Lauer 1979). The template was redshifted to match the source, smoothed (by convolving with a Gaussian), and scaled to fit the data either side of  $H\beta$ . (The convolution was carried out over a wavelength range broad enough that edge effects are not significant). The four free parameters in the fit were: the strength of the Fe II emission, the width of the convolution kernel (broadening parameter), and two parameters describing a 1st order polynomial used to model the continuum local to  $H\beta$ . (Where possible the region around He II  $\lambda 4686$  was ignored in the fit, although in some cases the He II emission may be broad and this will effect the fit.) The best-fit optical Fe II spectrum was then subtracted from

the data. The Fe II flux was measured between  $\lambda 4434$  and  $\lambda 4684$  as in Boroson & Green (1992). (Note that when Fe II measurements were taken from the literature, they were scaled by a factor, derived from the I Zw 1 template, to take into account the different in wavelength ranges used to define Fe II flux.) Figure 5.1 demonstrates the procedure.

The  $H\beta$  –[O III] regions of all the observed objects, before and after Fe II subtraction, are shown in Figure 5.2. The procedure described above generally did a reasonable job of estimating the strength of the Fe II emission and decontaminating the optical spectrum. There are three obvious exceptions however. In both RX J1050+55 and RX J1054+48 the part of the spectrum containing the  $H\beta$  line is redshifted into the region between the blue and red WHT spectra, and as the overlap between the two spectra is not well determined it is difficult to accurately measure the surrounding Fe II emission. In the highest redshift member of the sample, RX J1046+52, the  $H\beta$  –[O III] region is affected by strong A-band telluric absorption.

As mentioned above, the width of the Fe II lines in the fit was left as a free parameters. I Zw 1 has  $\text{FWHM } H\beta \sim 900 \text{ km s}^{-1}$ , and has Fe II lines of comparable width. This means that it was not possible to accurately model optical Fe II emission narrower than  $900 \text{ km s}^{-1}$ . As there are very few Seyfert 1s with  $\text{FWHM } H\beta \lesssim 900 \text{ km s}^{-1}$  this posed no serious problem. (The results of this fitting agree with the claim of Boroson & Green (1992) that the  $H\beta$  and optical Fe II lines have similar widths.) The other limitation of this method is that it assumes the ratios of the optical Fe II lines within and between blends are the same as those in I Zw 1. This appears to be a reasonable approximation for most objects, but a few (e.g., PG 1415+451) may show slightly different ratios.

### 5.3.2 Other line measurements

The other optical properties were measured from the dereddened, Fe II subtracted spectra using the DIPSO software package. To measure line fluxes local straight-line continua were fitted and subtracted from underneath the lines and the remaining line flux was integrated. In many cases there is a clear contribution to  $H\beta$  from a separate narrow component. In order to measure the properties of only the broad  $H\beta$  line, a narrow  $H\beta$  component was constructed, with a width determined from fitting the narrow [O III] lines, and included in a multiple Gaussian fit to the  $H\beta$  line. In most spectra the narrow component could be isolated and removed before the properties of the broad  $H\beta$  line were measured. The  $H\alpha$  line contains contributions from [N II]  $\lambda 6548, 6584$  which in general could not be isolated in

these data. Here, as in Grupe *et al.* (1999), the [N II] flux is subtracted by assuming that these lines contribute 35% of the flux in [O III]  $\lambda 5007$ , following Ferland & Osterbrock (1986).

### 5.3.3 Continuum measurements

The continuum level at the positions of H $\beta$   $\lambda 4861$  and H $\alpha$   $\lambda 6563$  was measured from the Fe II subtracted spectra, and further continuum fluxes were measured at 4000, 5500 and 7000 Å (in the rest frame of the source). The equivalent widths of the H $\beta$ , [O III] and Fe II lines were calculated with respect to the continuum underneath H $\beta$  to allow direct comparison with the measurements of Boroson & Green (1992) and Grupe *et al.* (1999). Two spectral indices ( $S_\nu \propto \nu^{-\alpha}$ ) were constructed from these flux measurements, namely:

$$\alpha_{opt} = 4.11 \log\left(\frac{f_{7000\text{\AA}}}{f_{4000\text{\AA}}}\right)$$

$$\alpha_{OX} = 0.489 \log\left(\frac{f_{5500\text{\AA}}}{f_{0.25\text{keV}}}\right)$$

These indices are almost identical to those used in Grupe *et al.* (1998a). In seven cases where the  $\lambda 5500$  flux is not available it was derived in an approximate way from  $m_V$  (column 13 of Table 5.1). Assuming that the uncertainty in flux ratios is  $\sim 10\%$  leads to an uncertainty of  $\sim 0.27$  in  $\alpha_{opt}$  and  $\sim 0.03$  in  $\alpha_{OX}$  and

Table 5.4 lists the derived parameters. The columns list the following information: (3) FWHM of broad H $\beta$ ; (4) FWHM of [O III]  $\lambda 5007$ ; (5), (6) and (7) list the local equivalent widths of the H $\beta$ , Fe II and [O III]  $\lambda 5007$  lines; (8) Balmer decrement, i.e., the ratio of fluxes in H $\alpha$ /H $\beta$ ; (9) ratio of the peak fluxes of [O III]  $\lambda 5007$  and broad H $\beta$ ; (10) and (11) ratio of fluxes of [O III] and Fe II to broad H $\beta$ ; (12) and (13) spectral indices defined above; (14) the monochromatic 0.25 keV luminosity in  $\nu L_\nu$  units (in the rest frame of the source).

Table 5.4: Properties of the sources which comprise the 1/4 keV-selected Seyfert galaxy sample.

No	Name	H $\beta$ FWHM (km/s)	[O III] FWHM (km/s)	H $\beta$ EW (Å)	Fe II EW (Å)	[O III] EW (Å)	H $\alpha$ / H $\beta$	peak [O III] / H $\beta$	[O III] / H $\beta$	Fe II / H $\beta$	$\alpha_{opt}$	$\alpha_{OX}$	$\log(\nu L_{1/4})$ erg/s
(1)	(2)	(3)	(4)	(5)	(6)	(7)	(8)	(9)	(10)	(11)	(12)	(13)	(14)
1	1E 0919+515	1390	-	38	78	-	-	-	-	2.05	-	0.9	44.5
2	Mrk 110	2120	-	145	20	3	-	2.5	0.7	0.14	-	0.9	43.9
3	US 0656	-	-	-	-	-	-	-	-	-	-	1.0	44.8
4	PG 0953+414	3130	-	156	39	19	-	0.8	0.1	0.25	-	1.4	45.2
5	IRAS 10026+4347	2990	825	55	99	5	-	-	0.1	1.81	0.1	1.1	44.8
6	RX J1008+46	13645	765	120	0	31	-	4.4	0.3	0.00	-	0.8	45.4
7	Ton 1187	2850	370	76	33	22	3.5	-	0.3	0.43	-	1.2	44.5
8	RX J1019+37	1130	675	75	0	26	2.8	5.9	0.3	0.00	1.3	0.8	44.8
9	Mrk 141	4175	395	30	38	16	3.8	-	0.5	1.25	1.5	1.3	43.4
10	Mrk 142	1790	280	52	86	10	3.3	-	0.2	1.65	1.2	0.9	44.0
11	RX J1026+55	5035	530	183	78	29	1.7	2.2	0.2	0.43	1.6	1.1	44.1
12	RE J1034+396	1500	900	60	-	45	3.0	-	0.8	-	-	1.0	44.0
13	RX J1046+52	2670	-	29	-	-	-	-	-	-	-	1.1	45.4
14	RX J1050+55	2780	760	51	0	23	5.0	1.6	0.5	0.00	1.5	1.2	45.1
15	RX J1054+48	5210	1115	71	0	18	3.6	1.2	0.3	0.00	-0.2	1.3	45.2
16	EXO 1055+60	2155	540	90	110	25	-	-	0.3	1.27	1.3	1.2	44.2
17	RX J1117+65	2160	880	65	78	11	-	-	0.2	1.20	1.2	1.1	44.5
18	PG 1116+21	2920	-	175	81	11	-	0.3	0.1	0.46	-	1.2	45.1
19	EXO 1128+691	1800	-	10	-	-	-	-	-	-	-	0.8	44.0
20	RX J1138+57	2845	485	39	56	25	3.3	3.7	0.6	1.43	0.5	0.9	44.4
21	NGC 4051	990	-	-	-	-	-	-	-	-	-	1.8	41.8
22	RX J1209+32	1370	860	63	67	28	3.5	0.9	0.4	1.06	0.6	0.9	44.5
23	RX J1226+32	3940	640	66	0	43	5.0	3.9	0.6	0.00	1.4	0.9	45.0
24	RX J1232+49	1905	895	55	92	9	4.5	0.3	0.2	1.67	0.9	0.9	44.9
25	Ton 83	1435	670	92	38	13	3.5	0.4	0.1	0.41	0.6	1.0	45.4
26	MCG +8-23-067	1245	645	30	0	41	3.6	2.6	1.4	0.00	2.5	1.0	43.2
27	IC 3599	675	615	9	0	18	3.7	2.3	2.1	0.00	1.8	0.7	43.7

No	Name	H $\beta$ FWHM (km/s)	[O III] FWHM (km/s)	H $\beta$ EW (Å)	Fe II EW (Å)	[O III] EW (Å)	H $\alpha$ / H $\beta$	peak [O III] / H $\beta$	[O III] / H $\beta$	Fe II / H $\beta$	$\alpha_{opt}$	$\alpha_{OX}$	$\log(\nu L_{1/4})$ erg/s
(1)	(2)	(3)	(4)	(5)	(6)	(7)	(8)	(9)	(10)	(11)	(12)	(13)	(14)
28	Was 61	2765	740	30	62	55	6.8	6.7	1.8	2.09	2.6	1.1	43.8
29	RX J1244+58	720	785	56	47	11	3.3	0.3	0.2	0.84	0.3	0.9	44.5
30	RX J1258+23	6920	420	29	25	34	4.0	18.6	1.2	0.86	2.8	1.0	43.9
31	RX J1312+26	3530	535	20	12	3	2.7	1.1	0.2	0.58	1.5	1.1	43.6
32	Ton 1571	1330	650	59	86	10	2.7	0.4	0.2	1.47	0.7	1.2	43.8
33	RX J1319+52	1620	415	29	45	35	4.0	4.5	1.2	1.53	1.1	0.9	44.2
34	RX J1328+24	2370	610	65	25	20	4.4	1.2	0.3	0.39	0.8	1.1	44.7
35	IRAS 13349+243	2775	1340	54	76	7	4.8	0.3	0.1	1.41	1.1	1.3	44.9
36	RX J1339+40	1180	425	21	9	9	3.5	1.1	0.4	0.43	1.4	0.9	44.1
37	RX J1342+38	4290	385	75	12	45	3.7	6.5	0.6	0.16	0.8	0.8	44.6
38	PG 1341+25	3300	440	60	43	18	3.9	2.1	0.3	0.72	1.0	1.2	44.0
39	Mrk 663	-	770	0	0	11	-	-	-	-	3.5	1.1	43.4
40	RX J1355+56	2600	935	44	46	46	4.8	5.0	1.8	1.05	0.5	1.1	44.4
41	PG 1402+261	2220	-	74	168	<1.8	-	<0.6	<0.02	2.25	-0.5	1.1	44.8
42	PG 1415+451	2575	-	69	132	<5.6	2.6	<0.03	<0.07	1.91	0.5	1.3	44.2
43	RX J1426+39	-	-	-	-	-	-	-	-	-	-	1.3	43.8
44	Mrk 684	1170	-	45	82	<1.1	2.0	<0.09	<0.02	1.81	0.9	1.3	43.7
45	Mrk 478	1915	610	65	87	12	3.7	-	0.2	1.34	0.7	0.9	44.9
46	PG 1444+407	2775	-	141	135	<7.3	2.5	<0.14	<0.04	0.96	-0.1	1.2	45.0
47	RX J1448+35	2430	625	54	64	24	3.1	1.7	0.4	1.18	0.5	1.3	44.0
48	NGC 5905	405	415	3	0	2	10.9	0.4	0.5	0.00	2.7	1.7	41.7
49	RX J1529+56	4055	540	100	8	170	3.8	12.5	1.7	0.08	0.9	1.1	44.4
50	MCG +06-36-003	6320	420	100	35	34	3.3	5.0	0.3	0.35	1.2	1.2	43.9
51	RX J1618+36	1705	390	20	23	13	2.9	2.7	0.6	1.14	1.7	1.0	43.5
52	RX J1619+40	3330	650	44	35	29	2.9	3.2	0.7	0.81	1.5	1.1	43.2
53	RX J1629+40	2675	750	55	36	32	3.0	1.6	0.6	0.64	0.4	0.9	45.1
54	RX J1646+39	1515	800	84	40	22	2.0	0.7	0.3	0.47	1.0	1.1	44.2

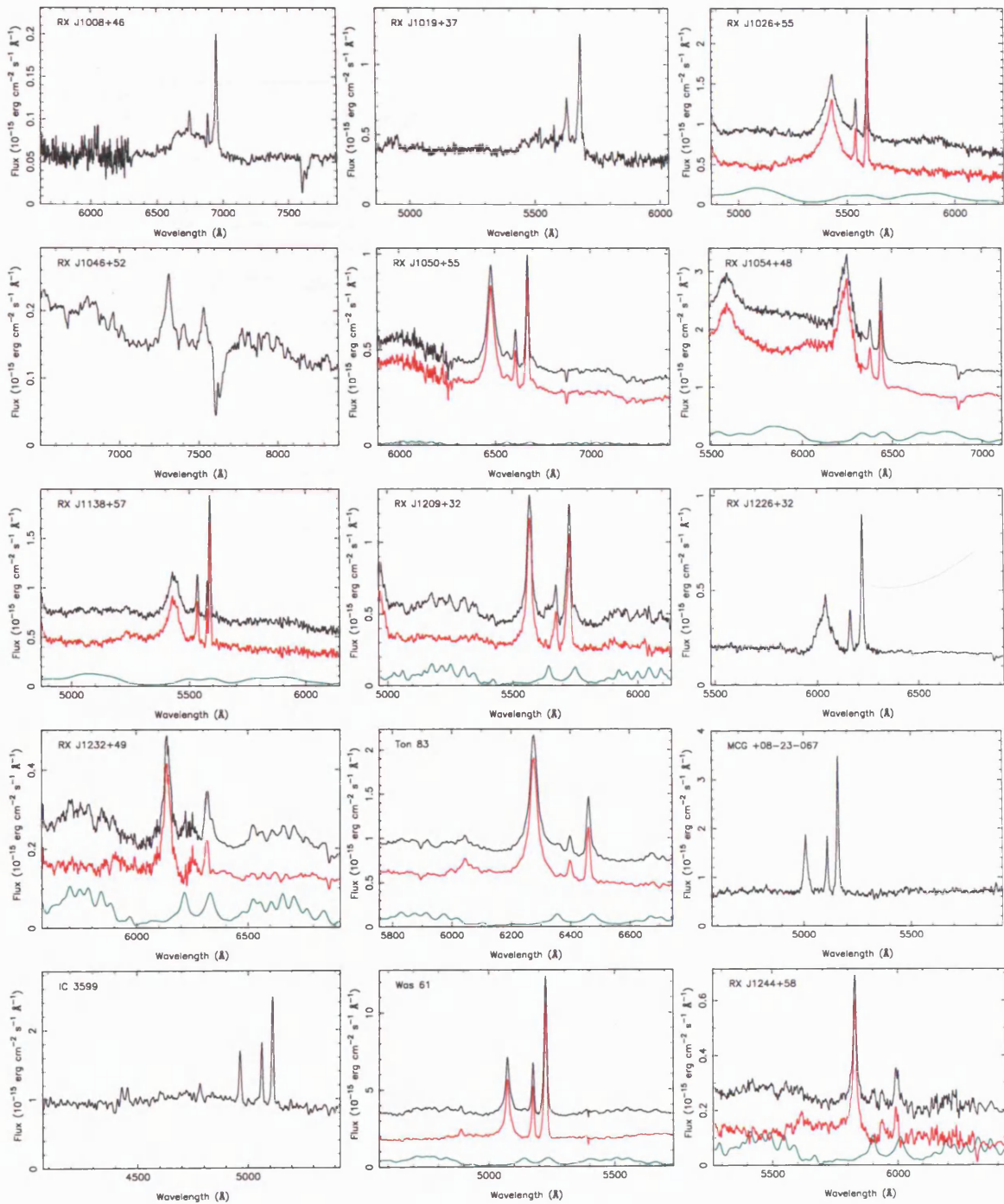
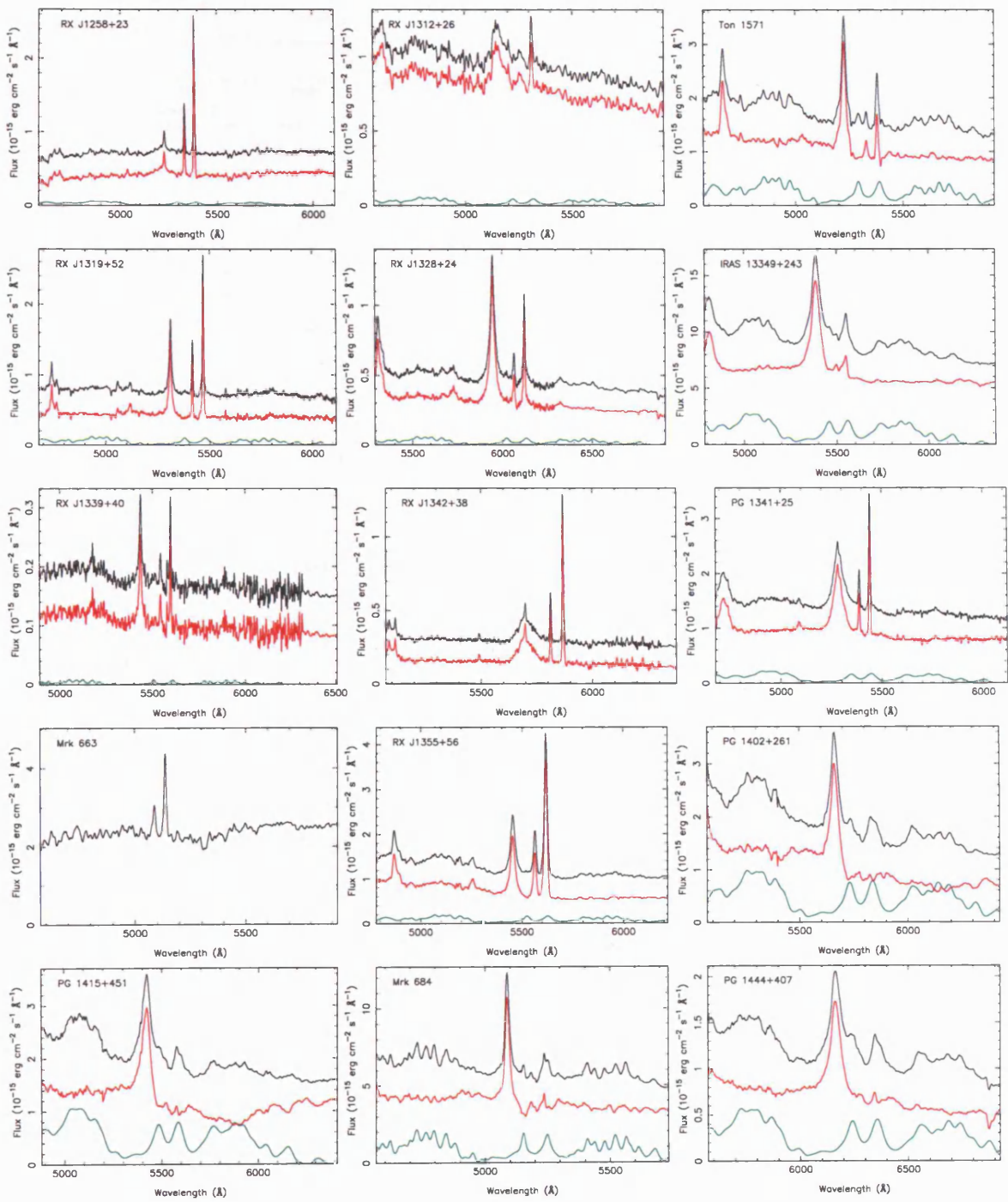
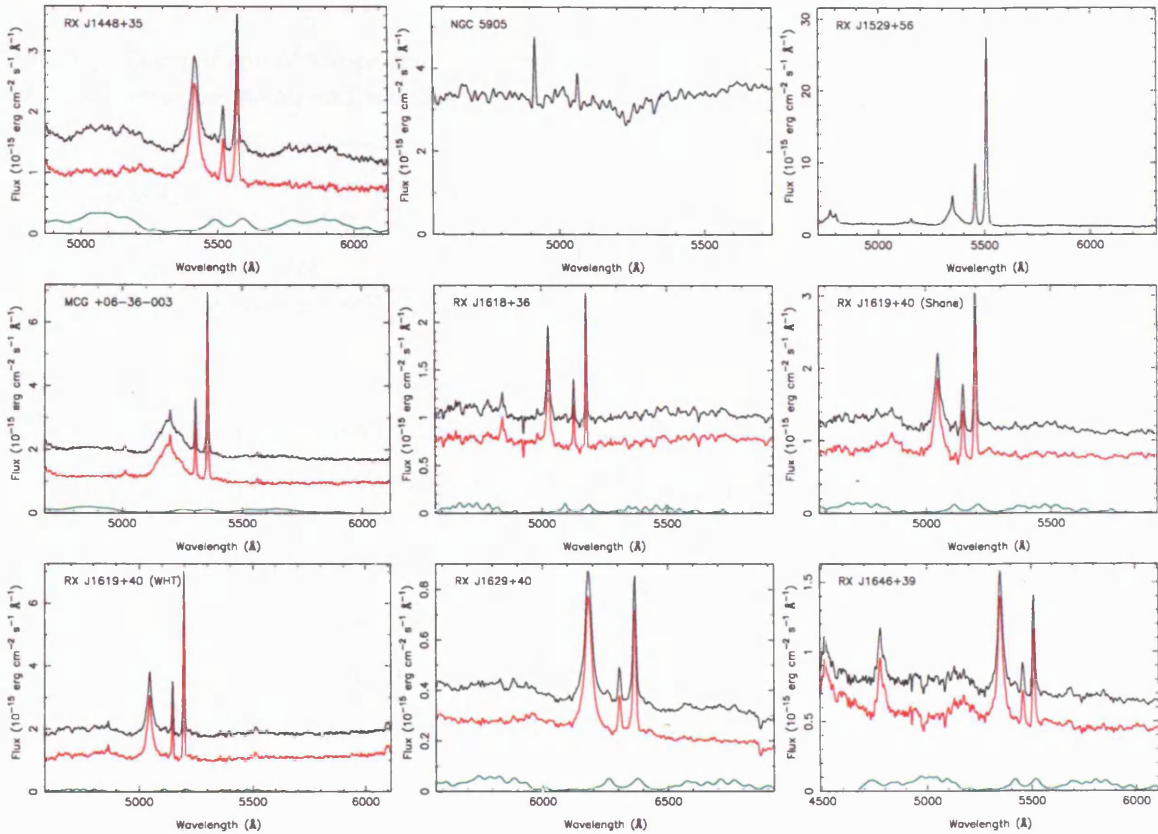


Figure 5.2: Close-up of the  $H\beta$  -  $[O III]$  region showing the fitted Fe II emission. In each panel the topmost curve shows the original spectrum, the middle curve shows the spectrum after Fe II subtraction and the lower curve shows the blurred Fe II template. Objects with no measurable Fe II emission are shown with only one curve. The topmost curve is shifted upwards by an arbitrary amount for clarity.





## 5.4 Analysis

The full optical dataset was used to define the global properties of the sample, as described in the next subsection, and to search for correlations between the various observed properties as discussed in Section 5.4.2. Section 5.4.3 considers the objects which lie at extreme ends of these correlations. Finally the luminosity functions of the complete sample of Seyfert galaxies and of various subsamples of objects are derived in section 5.4.4.

### 5.4.1 General sample properties

The Seyfert galaxy sample comprises roughly equal numbers of “ultrasoft” (here defined by  $\alpha_X > 1.7$ ) sources (28) and “normal” spectrum objects (26) with an overall mean  $\langle \alpha_X \rangle = 1.73$ . The sample can also be divided on the basis of  $H\beta$  line width. Twenty objects conform to the standard definition of an NLS1 leaving 31 broad-line Seyfert 1s (BLS1s) or Seyfert 2s (including one H II galaxy) and two objects for which  $H\beta$  measurements are not available. (Two objects appear to be transient in nature, and hence

Table 5.5: Comparison of the present sample with those of Grupe *et al.* (1999) and Boroson & Green (1992) showing the mean and standard deviation of the redshift, H $\beta$  line width and Fe II equivalent width.

Sample	Redshift		FWHM H $\beta$ (km s $^{-1}$ )		EQW Fe II ( $\text{\AA}$ )	
	mean	s.d.	mean	s.d.	mean	s.d.
1/4 keV	0.134	0.103	2752	2068	49	41
Grupe <i>et al.</i> (1999)	0.140	0.108	2787	1386	60	28
Boroson & Green (1992)	0.145	0.107	3358	1899	53	26

their exact identification is non-trivial, but have been left in the Seyfert sample. These are discussed further in § 5.4.3.) The mean redshift of the Seyfert sample is  $\langle z \rangle = 0.134$  with a standard deviation of 0.103.

Table 5.4.1 compares the present Seyfert sample with the samples of Grupe *et al.* (1999) and Boroson & Green (1992). The sample presented in Grupe *et al.* (1999) consists of 76 Seyfert galaxies selected mainly on the basis of *ROSAT* broad-band count rate and hardness ratio *HR*1, but unlike the present sample, is not statistically complete and is biased towards steeper spectrum objects. The sample presented in Boroson & Green (1992) consists of 87 BQS objects (Schmidt & Green 1983) with  $z \leq 0.5$ , selected on the basis of ultraviolet excess. Only the 70 radio-quiet members of the Boroson & Green 1992 sample were used for comparison with the present sample. All three samples have similar mean redshifts and the two X-ray selected samples show comparable H $\beta$  widths. It is interesting to note the mean EW Fe II for the present sample is closer to that of the Boroson & Green (1992) sample than the Grupe *et al.* (1999) sample.

## 5.4.2 Correlations between parameters

Correlation tests were first applied to pairs of parameters. In each trial two non-parametric correlation parameters were calculated, namely the Spearman rank-order correlation coefficient  $R_S$  and the Kendall  $\tau$  statistic (see Press *et al.* 1992); the results of the Spearman rank-order tests are shown in Table 5.6. Each entry contains the  $R_S$  (top) and the number of objects (bottom) included in the trial. Those with Spearman rank probabilities  $P_S < 0.01$  are marked in **bold**. At this level of significance,  $\lesssim 1$  spurious correlations might be expected by chance from 55 trials. Figures 5.3 and 5.5 show correlation diagrams for various parameters.

Table 5.6: Results of non-parametric correlation tests. Each entry shows the Spearman rank-order correlation coefficient  $R_S$  and the number of objects included in the test. Correlations significant at the  $> 99\%$  level are shown in bold.

(1)	H $\beta$ FWHM (2)	[O III] FWHM (3)	EW Fe II (4)	H $\alpha$ / H $\beta$ (5)	peak [O III]/H $\beta$ (6)	Fe II/ H $\beta$ (7)	[O III]/ H $\beta$ (8)	$\alpha_{opt}$ (9)	$\alpha_{OX}$ (10)	$\alpha_X$ (11)
$\log(\nu L_{1/4})$	0.26 (51)	0.33 (42)	0.13 (48)	0.16 (39)	-0.23 (35)	-0.14 (47)	<b>-0.43</b> (43)	<b>-0.63</b> (42)	-0.18 (54)	0.24 (54)
H $\beta$ FWHM		-0.14 (40)	-0.13 (47)	0.10 (39)	0.40 (35)	-0.16 (47)	-0.06 (43)	-0.03 (41)	0.21 (51)	-0.31 (51)
[O III] FWHM			0.13 (40)	0.03 (36)	-0.40 (32)	0.04 (39)	-0.19 (40)	-0.36 (38)	0.02 (41)	0.07 (42)
EW Fe II				-0.32 (38)	-0.37 (35)	<b>0.84</b> (47)	<b>-0.48</b> (42)	<b>-0.50</b> (42)	0.27 (48)	<b>0.45</b> (48)
H $\alpha$ /H $\beta$					0.10 (31)	-0.16 (39)	0.36 (36)	0.25 (37)	-0.07 (39)	0.08 (39)
Peak [O III] /H $\beta$						-0.14 (35)	<b>0.72</b> (35)	0.29 (31)	-0.35 (35)	<b>-0.53</b> (35)
Fe II /H $\beta$							-0.30 (42)	-0.30 (41)	0.16 (47)	-0.28 (47)
[O III] /H $\beta$								-0.20 (42)	-0.33 (43)	-0.20 (43)
$\alpha_{opt}$									-0.02 (42)	-0.33 (42)
$\alpha_{OX}$										-0.08 (54)

In total, from 55 trials, 8 correlations were found with two-sided probabilities  $P_S < 0.01$ . However, of these significant correlations, two merely represent trivial correlations between two different measures of the same property (relative strength of [O III] to H $\beta$ , and Fe II strength). All six non-trivial correlations are shown in Figure 5.3.

Caution must be applied when interpreting the remaining correlations as there is an inherent luminosity bias in the data. In the lowest luminosity objects there is often significant contribution from the host galaxy emission. The extreme cases of MCG+08-23-067, IC 3599, RX J1258+23, Mrk 663 and NGC 5905 show Ca II H and K absorption features from the host galaxy emission (see Appendix A). As a result these objects tend to show redder optical spectra (higher  $\alpha_{opt}$  values; see Figure 5.3e). The other potential difficulty with the current dataset is that the optical and X-ray observation were separated by a time interval of roughly nine years. As ultrasoft Seyferts are often highly variable this may introduce a large uncertainty in the derived values of  $\alpha_{OX}$  for individual sources, although the mean for the sample should be robust. Also, the non-simultaneity of the X-ray and optical data may reduce the significance of some of the underlying X-ray/optical correlations.

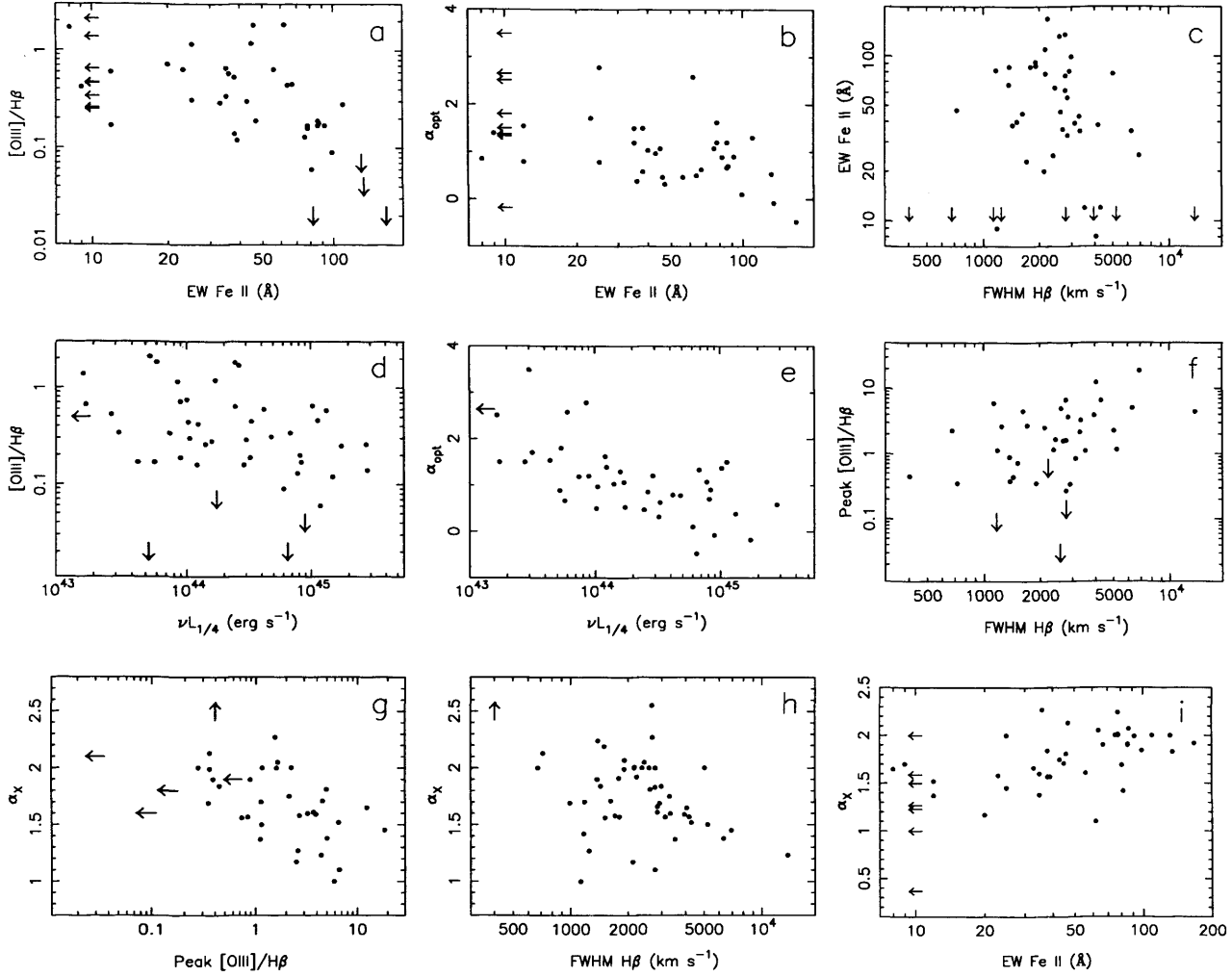


Figure 5.3: Correlation diagrams for various optical and X-ray parameters. Arrows indicate no detection in the case of Fe II and  $1\sigma$  limits for undetected [O III]. NGC 5905 has the steepest  $\alpha_X$  and is represented by an up arrow in panels g and h, it is also the lowest luminosity object as is indicated by the left arrow in panels d and e.

The well-known anti-correlation between FWHM H $\beta$  and  $\alpha_X$  is only weak in the present data ( $R_S = -0.31$ ;  $P = 0.03$ ). One reason for the weakness of the correlation may be the non-simultaneity of the data, as noted above. But it is also important to recognize that the relation between H $\beta$  width and  $\alpha_X$  is not necessarily one-to-one, but probably results instead from a ‘zone of avoidance,’ i.e., virtually all ultrasoft Seyferts have relatively narrow H $\beta$ , whereas optically defined NLS1s can have a wide variety of X-ray slopes. This can be seen Figure 5.3h (see also Boller, Brandt & Fink 1996) where there is only one ultrasoft Seyfert (RX J1026+55) with broad H $\beta$ . The absence of ultrasoft Seyferts with broad H $\beta$  is not the result of selection effects since the present sample is complete in terms of soft X-ray flux and includes no obvious optical selection bias.

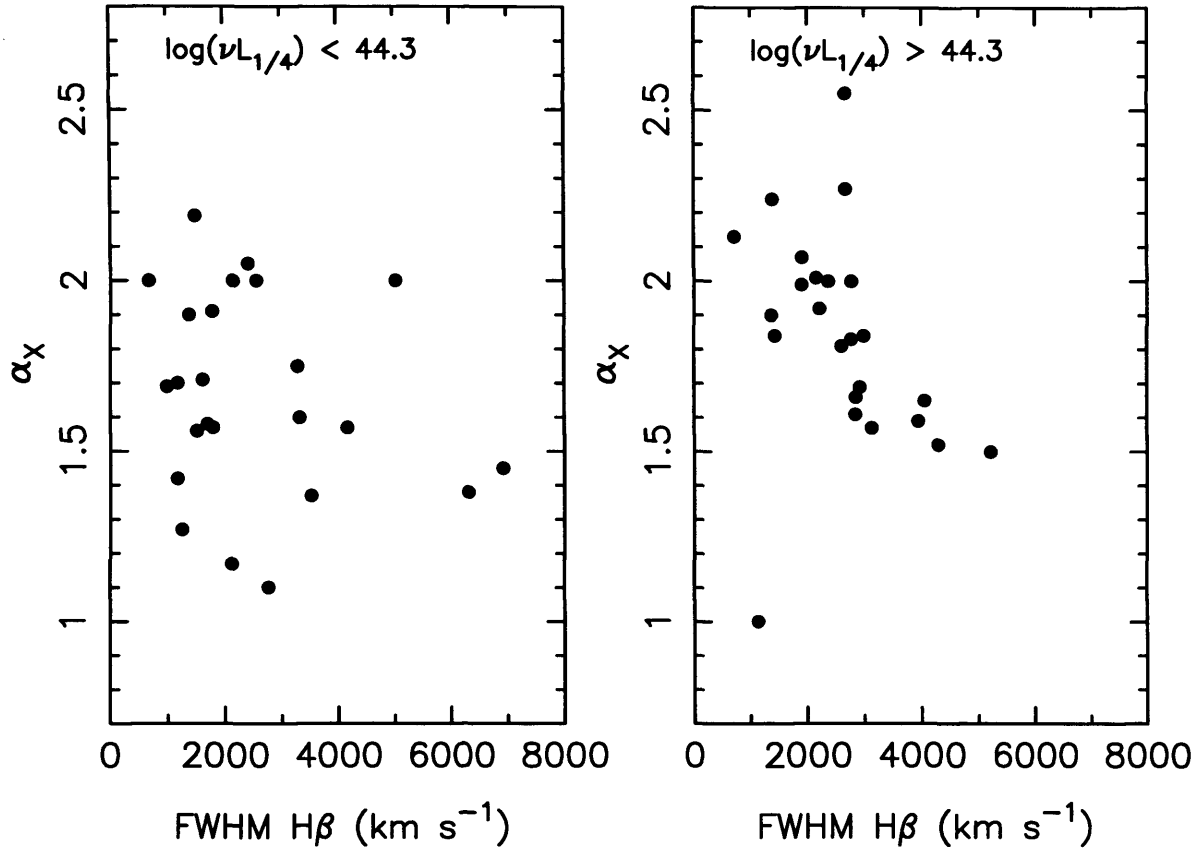


Figure 5.4: Correlation diagrams of FWHM H $\beta$  versus X-ray slope  $\alpha_X$  for lower and higher luminosity sources. The correlation is much stronger in the higher luminosity subsample.

It should also be noted that the correlation is stronger in the higher luminosity sources, as was also the case in the Grupe *et al.* (1999) sample. For the 25 objects with  $\nu L_{1/4} < 10^{44.3}$  erg s $^{-1}$  the correlation is weak ( $R_S = -0.26$ ;  $P_S = 0.20$ ) whereas it for the 26 objects with  $\nu L_{1/4} > 10^{44.3}$  erg s $^{-1}$  it is strong ( $R_S = -0.58$ ;  $P_S = 0.002$ ). See figure 5.4.

There is no significant correlation between the width of H $\beta$  and the strength of Fe II. Such a correlation has been claimed by Wills (1982), Zheng & O'Brien (1990) and Boroson & Green (1992), however, as discussed in Gaskell (1985) and Gaskell (2000), this is a result of how the strength of Fe II is measured. The quantity Fe II/H $\beta$  has been seen to correlate with FWHM H $\beta$ , but this is due to EW H $\beta$  decreasing as the line gets narrower. No correlation is seen if FWHM H $\beta$  is compared directly with EW Fe II. The lack of correlation between H $\beta$  width and Fe II strength (when measured independently of H $\beta$ ) has been confirmed by Grupe *et al.* (1999), Véron-Cetty, Véron & Gonçalves (2001) (see their section 3.3.1) and the present work.

## Principal Component Analysis

A Principal Component Analysis (PCA) was applied to the data in an attempt to separate independent sets of correlations. In essence, PCA defines a new coordinate system, defined by a set of eigenvectors called the principal components, which best describe the variance in the data. The first principal component (PC1) explains the largest fraction of variance in the data, the second (PC2) explains the largest fraction of the remaining variance, and so on. The motivation behind PCA is to extract groups of meaningful, independent correlations from a complex dataset. Francis & Wills (1999) and Francis *et al.* (1992) provide brief descriptions of PCA as applied to quasar spectra.

Table 5.7 reports the first three principal components of an analysis of 8 parameters (as is standard in such analyses, the ranked data were used to reduce the effect of outlying objects and allow for non-linear correlations). Only the 37 objects with measurements of all 8 parameters were used in the analysis (this necessarily excludes some of the most extreme objects with only upper limits on [O III] emission).

The analysis was applied to various sets of input data, with the number of input parameters varied from 7 to 12. In each case the first two principal components explained greater than 50% of the total variance. PC1 was most closely associated with  $\alpha_{opt}$ , [O III] /  $H\beta$  and  $\nu L_{1/4}$  and least associated with FWHM  $H\beta$ , whereas PC2 appears dominated by the FWHM  $H\beta - \alpha_X$  relation. PC3 appears to represent the variance in  $\alpha_{OX}$  and is the only remaining component to have an eigenvalue above 1 (sometimes considered to be an indicator of the significance of a component). The ordering of PC2 and PC3 was reversed in some of the tests, and they can be seen to contribute almost equally to the total variance. These results closely match those of Grupe *et al.* (1999). Indeed, when the PCA was repeated using exactly the same input parameters as those used by Grupe *et al.* (1999) the same PC1 was found. However, the non-simultaneity of the optical/X-ray data, and the luminosity bias noted above, hamper the interpretation of these principal components.

### 5.4.3 Outlying Seyferts

Figure 5.5 shows a correlation diagram with individual outlying objects marked. Four objects in particular stand out as Fe II -strong, [O III] -weak objects with blue optical spectra, these objects are: PG 1402+261, PG 1415+451, Mrk 684 and PG 1444+407. These lie at the extreme negative end of the PC1 defined by Boroson & Green (1992) (see also Kuraszkiwicz *et al.* 2000a). However, of these objects

Table 5.7: Results of PCA. The relative significances of the first three principal components are listed, as well as their projections onto the original input parameters.

	PC1	PC2	PC3
Eigenvalue	2.72	1.53	1.46
Percentage variance	34.01	19.19	18.36
Cumulative	34.01	53.21	71.56
$\alpha_X$	0.52	0.59	-0.20
$\nu L_{1/4}$	0.71	-0.17	0.53
FWHM $H\beta$	0.00	-0.87	-0.18
EW $H\beta$	0.66	-0.48	-0.18
EW Fe II	0.62	0.24	-0.43
$[O III] / H\beta$	-0.72	-0.05	0.38
$\alpha_{opt}$	-0.78	0.05	-0.25
$\alpha_{OX}$	0.06	-0.32	-0.83

only Mrk 684 conforms to the standard definition of an NLS1, with  $FWHM H\beta < 2000 \text{ km s}^{-1}$ , although the other three have ultrasoft X-ray spectra.

At the other end of the parameter space there is a group of six objects which stand out, these are: MCG+08-23-067, IC 3599, Was 61, RX J1258+23, Mrk 663 and NGC 5905. These all tend to possess stronger forbidden than permitted line emission ( $[O III] / H\beta > 1$ ) and weak (and therefore redder, due to host galaxy emission) optical continua when compared to soft X-rays ( $\alpha_{OX} > 1.5$ ). However, with the exception of Mrk 663, which shows no detectable  $H\beta$  emission, none of these objects have  $[O III] / H\beta > 3$ , a commonly used criterion for classifying Seyfert 2s. Only two of these objects stand out from the  $\alpha_X$  distribution; NGC 5905 had a remarkably steep soft X-ray spectrum at the time of the *ROSAT* survey, while Mrk 663 shows the hardest spectrum in the 1/4 keV sample. Mrk 663 is probably therefore the only candidate Seyfert 2 in the present sample besides the transient IC 3599.

Both IC 3599 and NGC 5905 have been identified as X-ray transient AGN (e.g., Grupe *et al.* 1995b; Brandt, Pounds & Fink 1995; Bade, Komossa & Dahlem 1996; Komossa & Bade 1999b). Both objects seem to have been detected by *ROSAT* during some kind of nuclear outburst and have in recent years ‘switched off,’ showing a substantial drop in their X-ray and optical continua as well as broad and high-excitation line emission. IC 3599 was originally identified as a NLS1 (see Brandt, Pounds & Fink 1995) but now shows only very weak and narrow permitted lines, while NGC 5905 now resembles an H II region more than a Seyfert galaxy. The striking similarity of the optical spectrum of the other weak- $H\beta$  objects to the two known transient AGN raises the interesting question of whether these objects also exhibit X-ray transient behaviour (as noted earlier the optical spectroscopy presented here

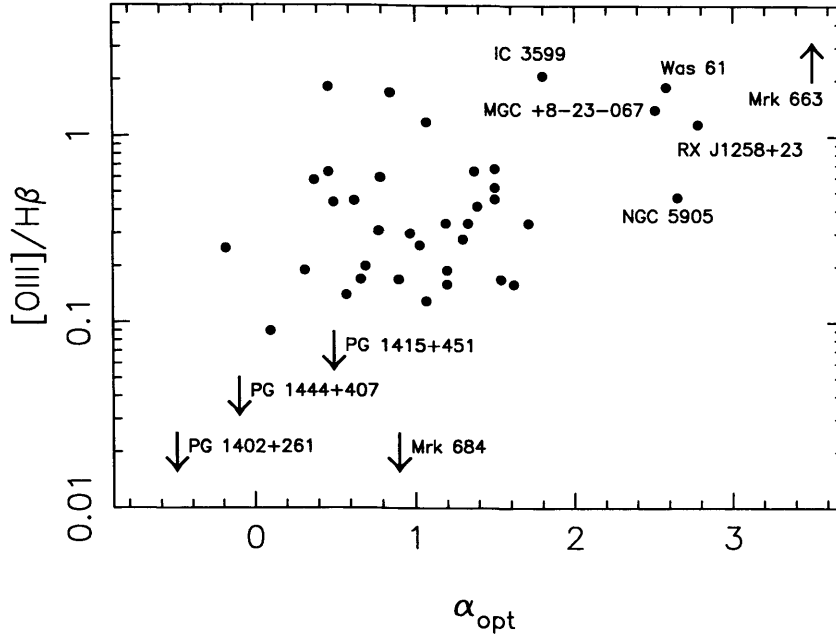


Figure 5.5: Correlation diagram revealing objects which lie at the extremes of the parameter space.

was taken 9 years after the *ROSAT* survey). In this scenario the X-ray continuum has decreased since the *ROSAT* survey, along with the optical continuum and permitted line emission<sup>6</sup>.

#### 5.4.4 The Seyfert Galaxy Luminosity Function

The information given in Tables 5.1 and 5.4 has been used to derive the luminosity function of the 1/4 keV-selected Seyfert galaxy sample. As with the WFC sample, the luminosity function was calculated using the  $1/V_{max}$  method of Schmidt (1968).

Here the luminosity  $\nu L_{1/4}$  is taken to be the monochromatic luminosity at 1/4 keV in the rest-frame of the source, in  $\nu L_\nu$  units (assuming spectral model comprising a  $\alpha_X = 2$  power-law modified by Galactic absorption). The  $\nu L_{1/4}$  values are tabulated for each source in Table 5.4. For a survey at 1/4 keV, the  $V_{max}$  calculation is greatly complicated by the variation of the Galactic foreground absorption across the sky. A similar problem was encountered for the WFC sample (previous chapter), here the same approach is employed.

For each source,  $V_{max}$  was estimated as:

<sup>6</sup>Mrk 663 was detected by the *ROSAT* HRI during a 3.1 ksec pointed observation in 1995 at a count rate of  $\sim 0.2$  ct  $s^{-1}$ . This is comparable with the PSPC count rate observed during the *ROSAT* survey and suggests that Mrk 663 is a persistent X-ray source.

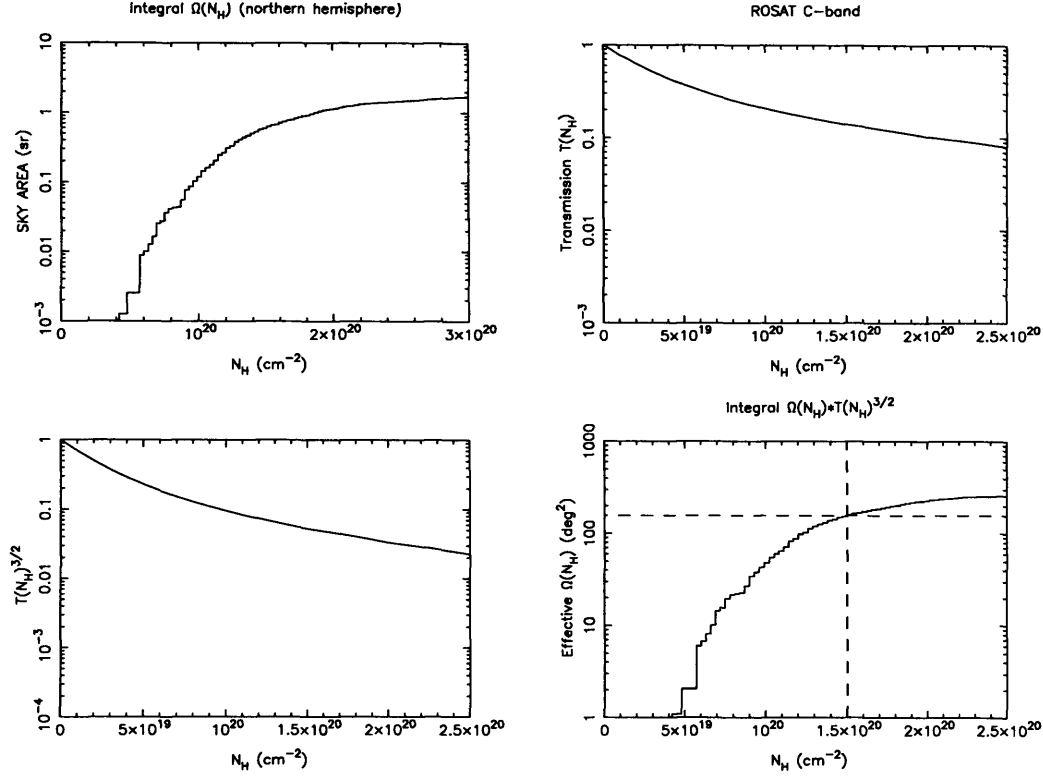


Figure 5.6: Cumulative form of the effective sky area function  $\Omega(N_H)T(N_H)^{\frac{3}{2}}$ , c.f. Figure 4.5. The dotted line shows the  $N_H$  limit used in this survey.

$$V_{max_i} = \int_0^{N_{Hlim}} \frac{1}{3} \Omega(N_H) \left( \frac{T(N_H)}{T(N_{H_i})} \right)^{\frac{3}{2}} d_i^3 \left( \frac{C_i}{C_{lim}} \right)^{\frac{3}{2}} dN_H,$$

The function  $\Omega(N_H)$  represents the differential sky area as a function of Galactic  $N_H$ . The integral  $\int \Omega(N_H) dN_H$  represents the area of sky actually surveyed whereas the integral  $\int \Omega(N_H) T(N_H)^{\frac{3}{2}} dN_H$  gives the equivalent area of *unabsorbed* sky. For the present survey the latter integral is  $4.8 \times 10^{-2}$  steradians or 157 square degrees (whereas integration of  $\Omega(N_H)$  between the same limits gives  $\sim 0.6$  steradians). The integrations were carried out over the northern hemisphere only, as the sample is restricted to  $\delta \geq 0^\circ$ , and are shown in Figure 5.6.  $C_i$  is the count rate of source  $i$  and  $C_{lim}$  is the survey count rate limit ( $C_{lim} = 0.25$ ).

Figure 5.7 shows the resulting luminosity function binned into logarithmic luminosity intervals and Table 5.8 lists the corresponding numerical information. (Note this analysis range excludes the sources NGC 4051 and NGC 5905 which have unusually low luminosities,  $\nu L_{1/4} < 10^{42}$  erg s $^{-1}$ .) The error bars were calculated using the prescription of Marshall (1985). The luminosity function derived for full

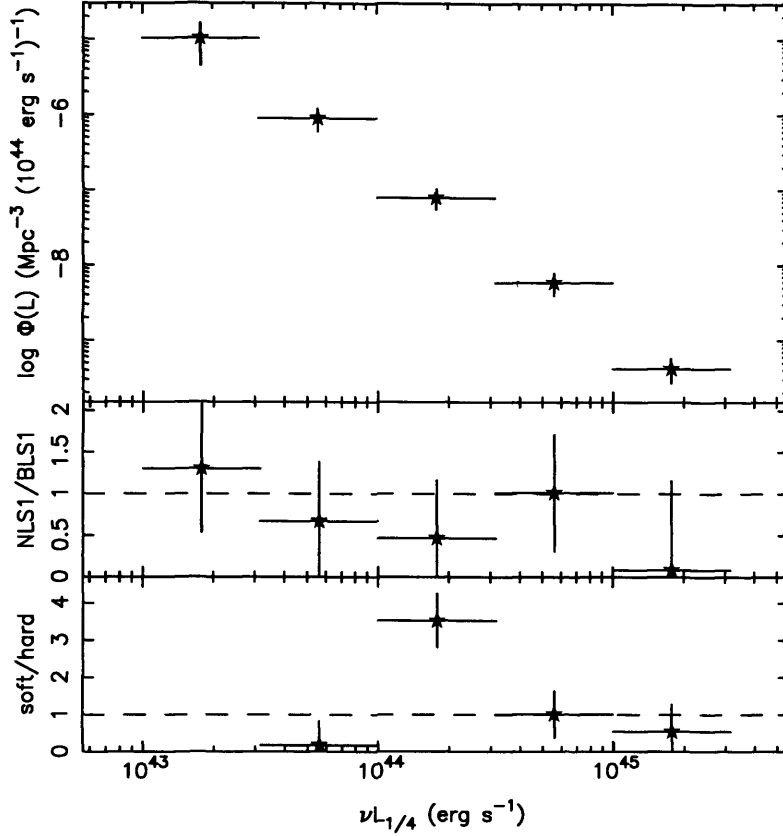


Figure 5.7: Luminosity function of the 1/4 keV-selected Seyfert galaxies. The top panel shows the function for the complete sample. The middle panel shows the ratio of luminosity functions when the sample is divided into narrow- and broad-line Seyfert 1s. The lower panel shows the ratio when the sample is divided on the basis of X-ray spectral slope. The binning is every half-decade in luminosity.

sample of 1/4 keV-selected Seyferts is entirely consistent with that previously calculated for the WFC-selected AGN (see previous chapter).

Next the sample was divided into subsamples and luminosity functions of each subsample calculated. The ratio of the two luminosity functions then gives the relative of space densities as a function of luminosity. The middle panel of Figure 5.7 shows this when the Seyferts were split into subsamples on the basis of  $H\beta$  width (i.e. NLS1 versus BLS1) or X-ray spectral slope (“ultrasoft” versus “normal” spectrum objects) as discussed in Section 5.4.1.

The ratio of the space densities of NLS1s and BLS1s is formally consistent with a constant over the range of luminosities probed. It is somewhat more difficult to interpret the incidence of ultrasoft Seyferts. In the present sample there are no such objects in the luminosity range  $\log(\nu L_{1/4}) = 43.0 - 43.5$  and the next highest luminosity bin there is the suggestion of incompleteness (see Table 5.8). However, in the range

Table 5.8: Luminosity functions for the 1/4 keV sample.  $\Phi(L)$  is in units of  $\text{Mpc}^{-3}(10^{44} \text{ erg s}^{-1})^{-1}$ .

$\log(\nu L_{1/4})$ ( $\text{erg s}^{-1}$ )	All Seyferts			(5)	(6)	(7)	(8)
	$\Phi(L)$	$\langle V/V_{max} \rangle$	$N$				
(1)	(2)	(3)	(4)				
43.0-43.5	$2.2 \pm 1.3 \times 10^{-6}$	$0.58 \pm 0.13$	5				
43.5-44.0	$6.1 \pm 2.0 \times 10^{-7}$	$0.41 \pm 0.08$	12				
44.0-44.5	$1.7 \pm 0.5 \times 10^{-7}$	$0.53 \pm 0.08$	13				
44.5-45.0	$4.0 \pm 1.5 \times 10^{-8}$	$0.58 \pm 0.08$	13				
45.0-45.5	$9.1 \pm 3.3 \times 10^{-9}$	$0.58 \pm 0.10$	9				
	NLS1s			BLS1s			NLS1/ BLS1
	$\Phi(L)$	$\langle V/V_{max} \rangle$	$N$	$\Phi(L)$	$\langle V/V_{max} \rangle$	$N$	
43.0-43.5	$6.4 \pm 5.1 \times 10^{-7}$	$0.46 \pm 0.20$	2	$4.9 \pm 3.6 \times 10^{-7}$	$0.54 \pm 0.20$	2	$1.3 \pm 0.8$
43.5-44.0	$2.2 \pm 1.2 \times 10^{-7}$	$0.19 \pm 0.11$	6	$3.3 \pm 1.7 \times 10^{-7}$	$0.57 \pm 0.13$	5	$0.7 \pm 0.7$
44.0-44.5	$5.4 \pm 3.2 \times 10^{-8}$	$0.68 \pm 0.17$	3	$1.2 \pm 0.4 \times 10^{-7}$	$0.48 \pm 0.09$	10	$0.5 \pm 0.7$
44.5-45.0	$1.8 \pm 0.8 \times 10^{-8}$	$0.52 \pm 0.12$	6	$2.0 \pm 0.9 \times 10^{-8}$	$0.59 \pm 0.12$	6	$1.0 \pm 0.7$
45.0-45.5	$7.1 \pm 7.1 \times 10^{-10}$	$0.53 \pm 0.29$	1	$8.4 \pm 3.2 \times 10^{-9}$	$0.58 \pm 0.10$	8	$0.1 \pm 1.1$
	ultrasoft			hard			soft/ hard
	$\Phi(L)$	$\langle V/V_{max} \rangle$	$N$	$\Phi(L)$	$\langle V/V_{max} \rangle$	$N$	
43.0-43.5	—	—	0	$2.2 \pm 1.3 \times 10^{-6}$	$0.58 \pm 0.13$	5	—
43.5-44.0	$9.0 \pm 4.7 \times 10^{-8}$	$0.11 \pm 0.14$	4	$5.2 \pm 2.0 \times 10^{-7}$	$0.55 \pm 0.10$	8	$0.2 \pm 0.6$
44.0-44.5	$1.3 \pm 4.7 \times 10^{-7}$	$0.57 \pm 0.10$	9	$3.7 \pm 2.3 \times 10^{-8}$	$0.54 \pm 0.17$	3	$3.5 \pm 0.7$
44.5-45.0	$2.3 \pm 8.1 \times 10^{-8}$	$0.52 \pm 0.09$	10	$2.3 \pm 1.2 \times 10^{-8}$	$0.61 \pm 0.14$	4	$1.0 \pm 0.6$
45.0-45.5	$3.2 \pm 1.8 \times 10^{-9}$	$0.56 \pm 0.14$	4	$5.9 \pm 2.8 \times 10^{-9}$	$0.59 \pm 0.13$	5	$0.5 \pm 0.7$

$\log(\nu L_{1/4}) = 44.0 - 45.5$  the relative number of ultrasoft objects appears to decrease with luminosity. Interestingly a deficit of ultrasoft Seyferts at high luminosities might be expected due to the effects of the ‘ $K$ -correction.’ Basically the steep spectrum objects will be harder to detect at higher redshifts due to the decrease in flux *observer’s frame* flux by a factor  $(1+z)^{\alpha-1}$ , where  $\alpha$  is the spectral index; in effect the bright soft X-ray emission is being redshifted out of the observing band. Unfortunately the statistical limitations of the present sample mitigate against a more detailed quantitative analysis of this point.

To date only two NLS1s have been reported at a redshift  $z > 0.5$  namely the quasar E 1346+266 with  $z = 0.92$ , which shows optical and X-ray spectra characteristic of NLS1s (Puchnarewicz, Mason & Cordova 1994), and RX J2241-44 at  $z = 0.55$  (Grupe *et al.* 1998a). Of the 69 spectroscopically identified AGN in the deep *ROSAT* surveys of the Lockman Hole (Hasinger *et al.* 1998; Schmidt *et al.* 1998) only one can be positively identified with an NLS1 (at  $z = 0.462$ ; Hasinger *et al.* 2000).

## 5.5 Discussion

A new sample of soft X-ray bright Seyfert galaxies is presented. The sample is the first to be selected in the  $\sim 1/4$  keV *ROSAT* band and is statistically complete.

The analysis reported in Section 5.4.2 reveals correlations between the soft X-ray spectral slope  $\alpha_X$  and the optical [O III] and Fe II line strengths, and the previously known relation between  $\alpha_X$  and FWHM  $H\beta$ . These relationships appear more like zones of avoidance than linear correlations (see also Section 4.2 of Lawrence *et al.* 1997). A steep X-ray slope (e.g.,  $\alpha_X \gtrsim 1.7$ ) seems to be a prerequisite for strong Fe II ( $EW > 100\text{\AA}$ ) and is almost invariably accompanied by strong, narrow  $H\beta$  (FWHM  $H\beta \lesssim 3000 \text{ km s}^{-1}$ ; Peak [O III] /  $H\beta \lesssim 0.5$ ). Given the non-simultaneity of the optical/X-ray data and the significant soft X-ray variability exhibited by the source population, these relationships must be intrinsically strong to remain apparent in the current analysis.

The link between  $\alpha_X$  and the optical parameters therefore seems to be driving the correlations responsible for the first principal component of Boroson & Green (1992) (which is dominated by the strength of [O III] and Fe II and to a lesser extent FWHM  $H\beta$ ). This is supported by the strong correlation between Boroson & Green (1992) PC1 and X-ray slope found by Brandt & Boller (1998). Thus it appears that the high energy continuum, and the slope of the soft X-ray spectrum in particular, are driving many of the relationships observed in optical correlation analyses. This is perfectly reasonable since the physical conditions of the line-emitting plasma will be strongly effected by the incident high-energy continuum. A similar conclusion was reached by Kuraszek *et al.* (2000b), who explained the different ultraviolet emission properties of a small sample of NLS1s as an effect of the different photoionising continuum in these objects.

The ultrasoft Seyferts, defined by their steep X-ray spectra, are also characterised by extreme values of other observables. The high energy continuum is more closely linked to the underlying accretion processes than are the optical line ratios/widths. However, it is the overlapping class of optically defined NLS1s that have received particular attention, largely on the basis of exceptional X-ray properties in many ultrasoft examples (e.g., Boller *et al.* 1993; Pounds, Done & Osborne 1995). It is now clear that Seyferts selected on the basis of  $H\beta$  line width span a range of observed properties, many showing spectra otherwise characteristic of ‘normal’ Seyfert 1s; the present analysis confirms that optically defined NLS1s do not show enhanced Fe II emission compared to BLS1s, as has been previously suggested. The shape of the high energy continuum is therefore a much more direct indicator of the primary driving processes in AGN than is the width of  $H\beta$ . The present sample then represents the ideal one in which to search for extremes of behaviour.

Seyferts with weak permitted line emission (e.g.,  $H\beta$  and Fe II) sit at at one end of the observed

correlations. These are generally rare in soft X-ray surveys, yet the present sample contains a number of such objects. Two of these are known to be X-ray transient and it is plausible that other  $H\beta$ -weak Seyferts in the sample are transient in nature. This hypothesis clearly needs to be tested with repeat X-ray and optical observations. If a significant number of the 1/4 keV-selected sources are confirmed as X-ray transients then this would suggest that, at least for a significant fraction of the population, the ultrasoft Seyfert state may be a relatively short-lived one.

The alternative explanation, namely that these objects have not changed significantly since the *ROSAT* survey, is equally interesting. Puchnarewicz & Mason (1998) and Grupe *et al.* (1998b) discuss soft X-ray selected Seyferts which appear to show optical reddening but no X-ray absorption. One possible solution is that these objects all contain dusty, ionised gas along the line-of-sight. The small dust grains are needed to redden the optical continuum, while the surrounding gas is ionised and so produces no soft X-ray absorption. However the lack of any correlations involving the Balmer decrement (indicative of reddening by dust) suggests this may not be the solution. It is difficult to see how Seyfert galaxies that are bright in the 1/4 keV band, and so presumably contain little or no absorption, yet have weak permitted lines, are compatible with the standard Seyfert unification scheme (e.g., Antonucci 1993).

## Chapter 6

# Conclusions

A brief summary of the main results of the present work is given, followed by possible direction for future work.

### 6.1 Summary of results

In Chapter 2 an analysis of the *ASCA* X-ray spectral data for a sample of 22 NLS1s was presented. Absorption from *neutral* gas intrinsic to the host galaxy appears to be a rare occurrence in NLS1s, on the contrary, most NLS1s exhibit “soft excess” emission superposed on the hard power-law continuum which can be modelled as a blackbody. This soft component often contains a significant fraction of the X-ray luminosity in these sources, even in the relatively hard *ASCA* bandpass (0.6–10 keV) and in the most extreme cases this presents an argument against an origin for the soft excess by reprocessing of the hard continuum. The underlying power-law spectra span a wide range of slopes ( $\Gamma = 1.6 - 2.5$ ) with a mean spectral index of 2.1, which is only slightly steeper than the norm for BLS1s. Iron  $K_{\alpha}$  emission lines are detected at a modestly significant level in roughly half of the objects observed, but unfortunately the line properties such as centroid energy, equivalent width and intrinsic width are in general rather poorly constrained by the *ASCA* data.

The X-ray spectra of NLS1s below 2 keV often exhibit additional features, which have been discussed in terms of absorption by ionised material in the line of sight. Three of the NLS1s show evidence for absorption in the 0.7–0.9 keV range, probably arising from O VII and O VIII edges, warm absorber features commonly observed in BLS1s. Six NLS1s also show spectral features in the 1.1–1.4 keV band-

pass, which, at least in some instances, may arise from resonance absorption in highly ionised material. An unexpected result was that all objects showing indications of highly ionised gas lie in the lower half of the  $H\beta$  line width distribution (i.e. the sources with complex X-ray spectra have  $H\beta$  FWHM  $\leq 1000 \text{ km s}^{-1}$ ). If confirmed in future samples (using larger numbers of objects and better quality X-ray data) this would indicate another link between the X-ray and optical properties of AGN.

In Chapter 3 a simultaneous *ASCA* and *RXTE* observation of the bright NLS1 Ark 564 was presented. The measured X-ray spectrum is dominated by a steep ( $\Gamma \approx 2.6$ ) power-law continuum extending to at least 20 keV, with imprinted Fe K-line and -edge features and an additional soft excess below  $\sim 1.5$  keV. The energy of the iron K-edge indicates the presence of highly ionised material, which we identify in terms of reflection from a strongly irradiated accretion disc. The high reflectivity of this putative disc, together with its strong intrinsic O VIII Ly- $\alpha$  and O VIII recombination emission, can also explain much of the observed soft excess flux. The source is much more rapidly variable than ‘normal’ Seyfert 1s of comparable luminosity, increasing by a factor of  $\sim 50\%$  in 1.6 hours, with no measurable lag between the 0.5–2 keV and 3–12 keV bands.

Chapter 4 described a sample of extragalactic sources selected on the basis of their detection in the EUV by the *ROSAT* WFC. A catalogue of 34 sources is constructed, which after the exclusion of those identified with Galactic objects, reduced to a sample of 19 EUV-bright AGN. These represent the first complete and unbiased sample of EUV-selected AGN. NLS1s are well represented, making up just under half the sample, with BLS1s and BL Lac objects comprising the remainder. This is in stark contrast with hard X-ray selected samples, in which NLS1s have negligible representation. These data are used to directly derive the first luminosity function for AGN measured at EUV energies (specifically at 200 eV). The luminosity function implies a roughly equal contribution to the EUV volume emissivity from each decade of luminosity for  $L_{200}$  between  $10^{43}$  to  $10^{46} \text{ erg s}^{-1} \text{ keV}^{-1}$ , but with a sharp cut off at higher luminosities. Finally, it is noted that NLS1s contribute roughly half of the local ( $z \approx 0$ ) volume emissivity at 200 eV, again in contrast to the situation pertaining at harder X-ray energies.

Chapter 5 extended this work to a much larger sample, describing the first complete sample of AGN selected on the basis of their  $\sim 1/4$  keV flux. The  $1/4$  keV selected Seyfert sample comprises 54 Seyfert galaxies, 20 of which are identified as NLS1s on the basis that FWHM  $H\beta \leq 2000 \text{ km s}^{-1}$ . The well-known anti-correlation between the strengths of Fe II and [O III] emission is detected, along with correlations between the soft X-ray slope and [O III] emission, Fe II strength and  $H\beta$  width. These suggest that

the so-called ‘primary eigenvector’ found in other samples is a direct result of a few optical lines being correlated with the soft X-ray spectrum. It also appears to be the case that Seyfert 1s with narrow permitted lines do not tend to have stronger Fe II emission than Seyfert 1s with broader permitted lines, as has been previously claimed. Thus it seems that a steep X-ray spectrum is a better indicator of an “extreme” set of physical properties in Seyfert galaxies than is the narrowness of the optical  $H\beta$  line. These data are used to isolate objects that lie at one end of the correlations, with relatively strong [O III] emission and weak optical continua, as these are rare in most other samples of soft X-ray selected AGN. Two of these objects are known to show X-ray transient behaviour, future observations are needed to confirm the nature of the other objects. The luminosity function for 1/4 keV selected Seyferts is presented and broken down into subsamples to investigate the relative space densities of Seyferts when separated on the basis of either X-ray slope or  $H\beta$  line width.

## 6.2 Future work

During the course of writing this thesis the next generation of X-ray observatories was launched. *Chandra* was launched on 23 July 1999 and *XMM-Newton* was launched 10 December 1999, both without problems. These new missions provide the opportunity to study some of the phenomena described in this work with unprecedented detail.

The combination of high effective area, good spectral and spatial resolution and extended bandwidth afforded by *Chandra* and *XMM-Newton* should allow unambiguous identification of the spectral features which appear to characterise NLS1 galaxies and also confirm whether highly ionised absorption systems are preferentially observed in NLS1s with extremely narrow  $H\beta$  line widths. For example, recent *XMM-Newton* observations of IRAS 13349+2438 have revealed a rich absorption spectrum (Sako *et al.* 2001). Another aspect of the X-ray spectra of NLS1s that has, until recently, been difficult to study is the profile of the iron  $K_{\alpha}$  line. This could in principle allow one to distinguish between the various competing models for NLS1 activity (e.g. face-on accretion disc or high accretion rate).

A recent, intensive, multi-wavelength monitoring campaign has been performed on Ark 564, the subject of Chapter 3. The combination of *RXTE*, *HST*, *Chandra*, *ASCA* and ground-based optical spectroscopy should enable a detailed measurement of many of the important parameters of this interesting source. For example, correlated variability of the ultraviolet/optical continuum and emission lines, if observed,

could be used to ‘reverberation map’ the broad-line region and provide an estimate of the mass of the central putative black hole.

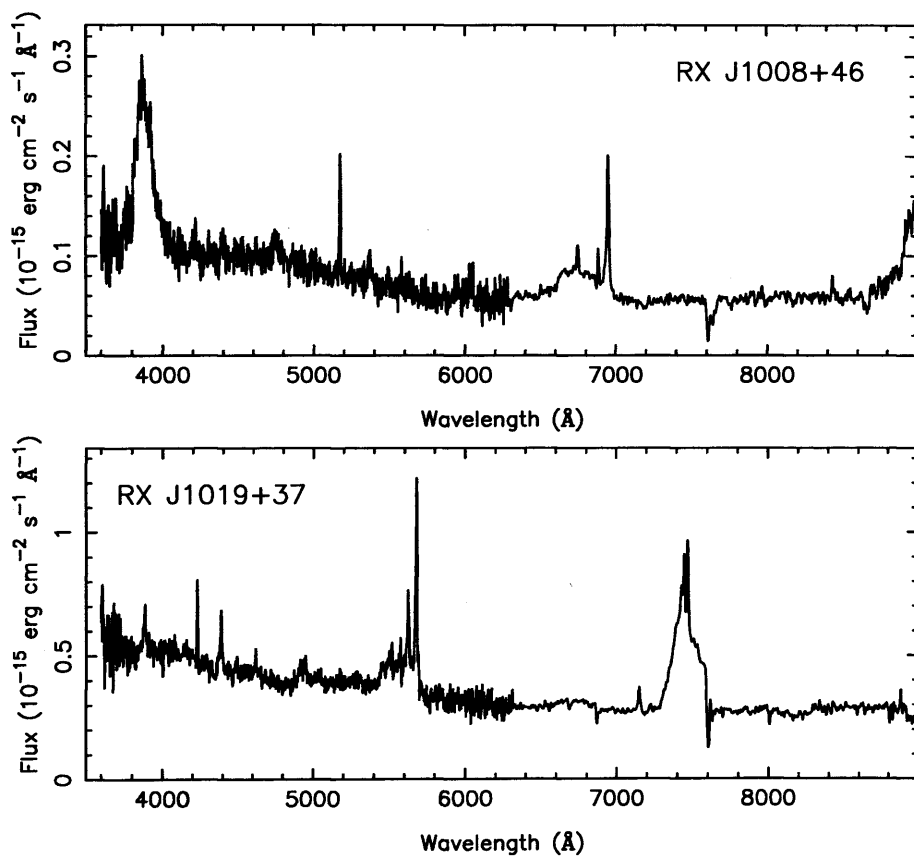
The nature of the soft excess in NLS1s can be probed with high spectral resolution using the *Chandra* Low Energy Transmission Grating (LETG). A simultaneous observation of the soft X-ray bright NLS1 Mrk 478 with the *Chandra* LETG and *BeppoSAX*, performed during August 2000, should provide an interesting test of the various competing models of soft excess emission.

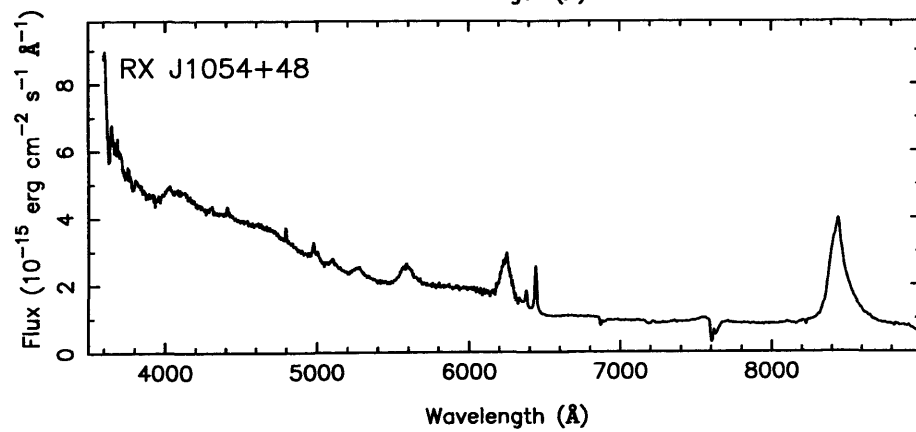
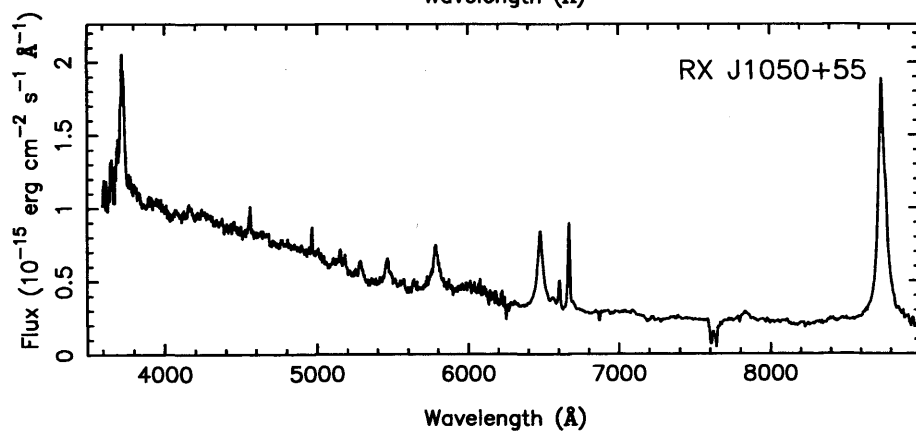
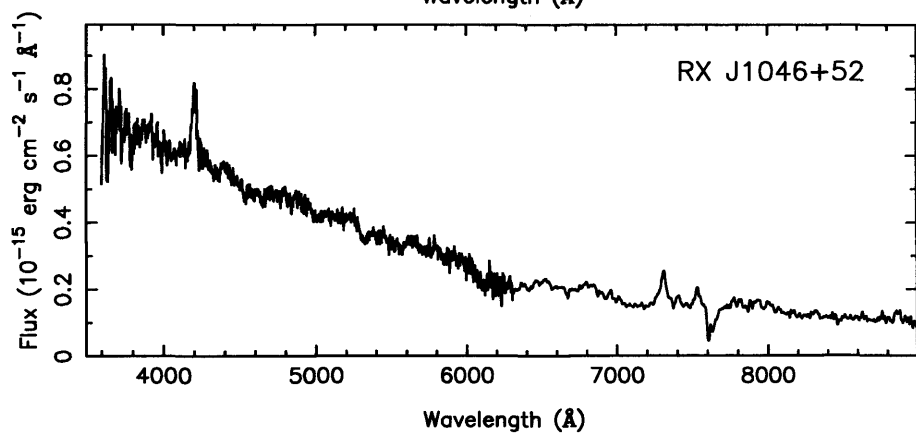
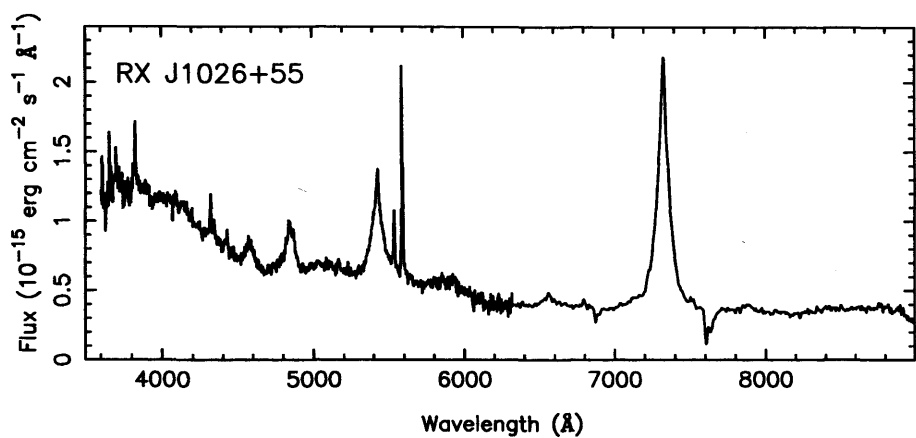
The samples of soft X-ray bright AGN defined in Chapters 4 and 5 provide excellent material for future studies. These represent the soft X-ray brightest and least absorbed AGN on the sky. Broad-band X-ray observations of these objects with *XMM-Newton* would allow a detailed comparison of the X-ray spectral and temporal properties of NLS1s and BLS1s selected on the same basis. High signal-to-noise soft X-ray spectra provided by the EPIC instruments may also allow an accurate determination of the shape of the soft excess and, in principle, measure the temperature of the inner accretion disc. New X-ray and optical observations are also needed to determine how many of these objects, if any, exhibit transient behaviour. If a significant fraction of these Seyferts were found to have “switched off” in repeat observations this would imply that, at least for some fraction of the population, the “ultrasoft” Seyfert state is a relatively short lived one.

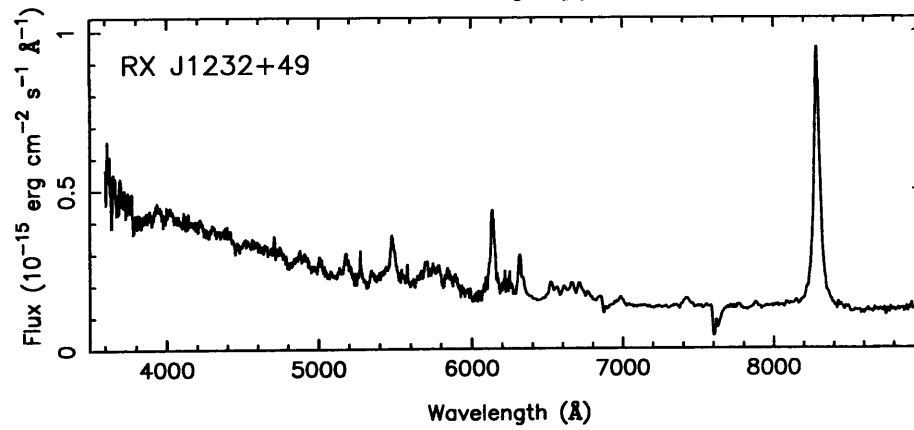
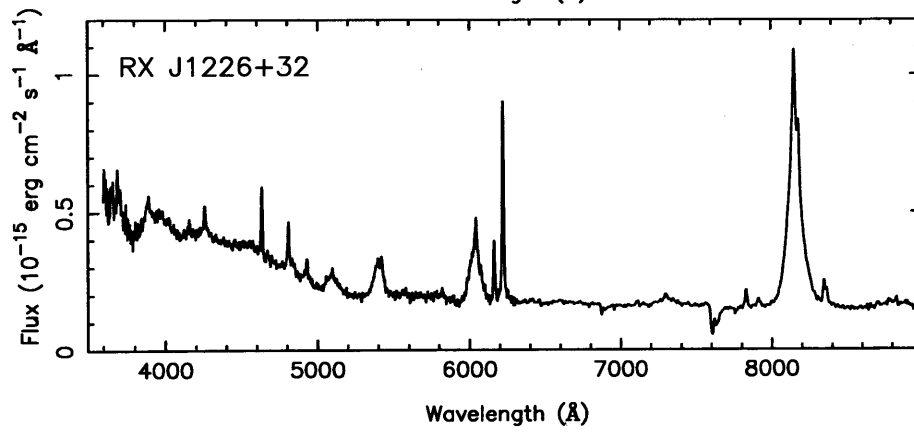
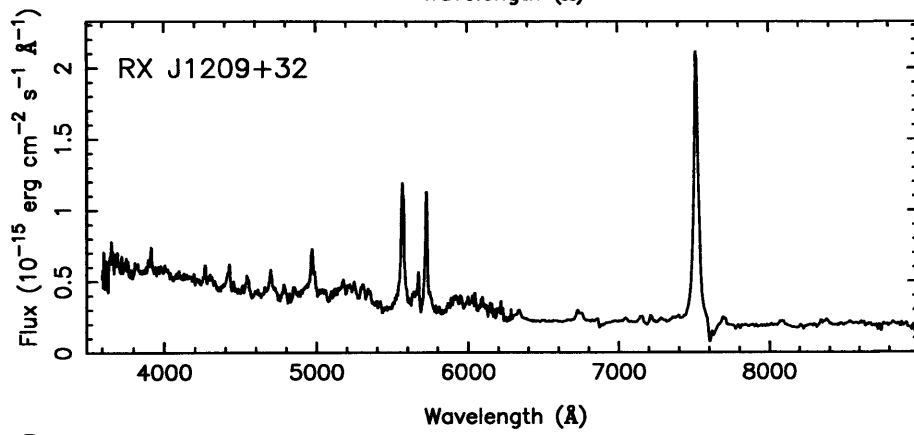
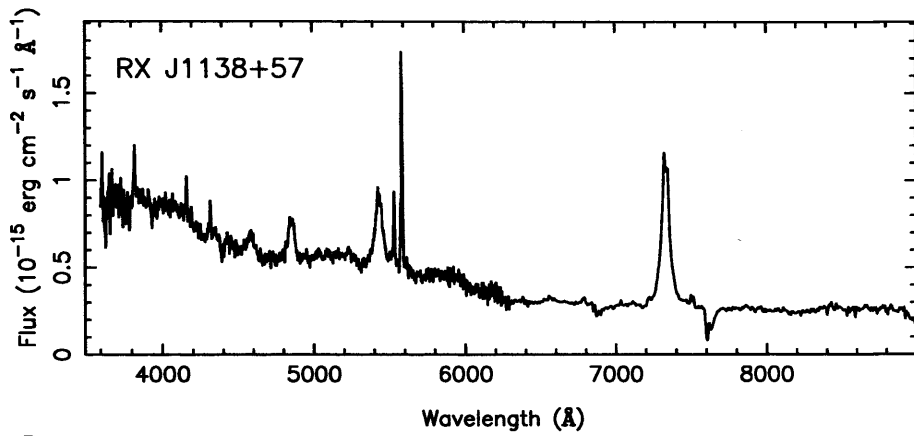
## Appendix A

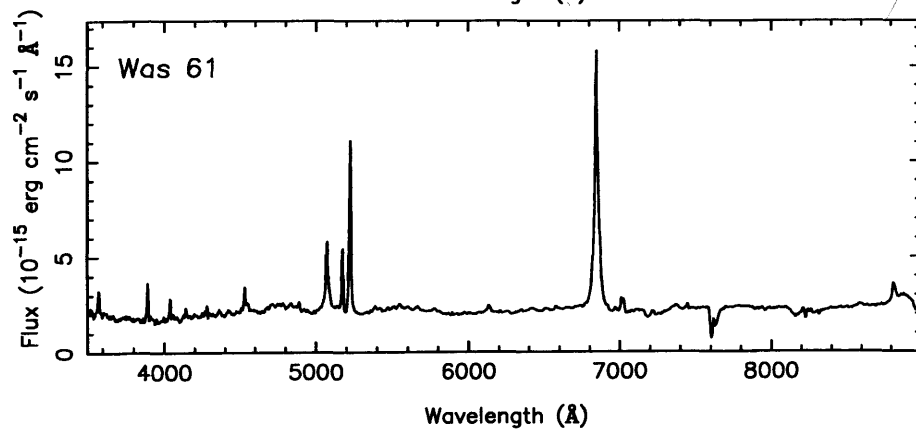
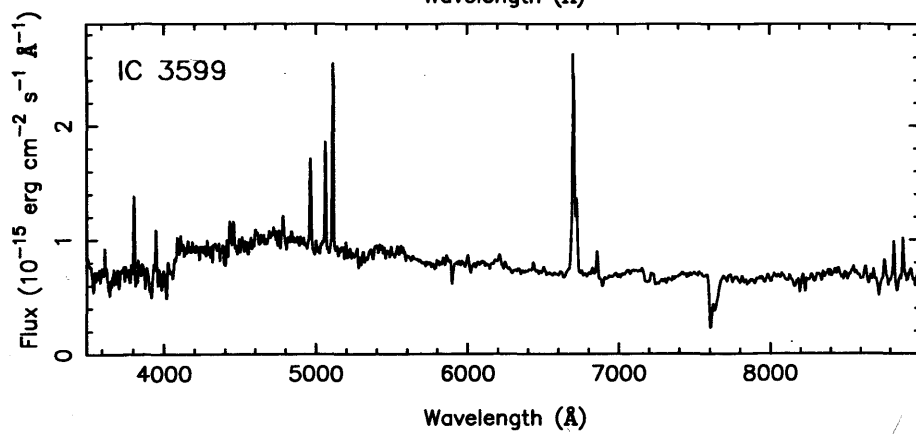
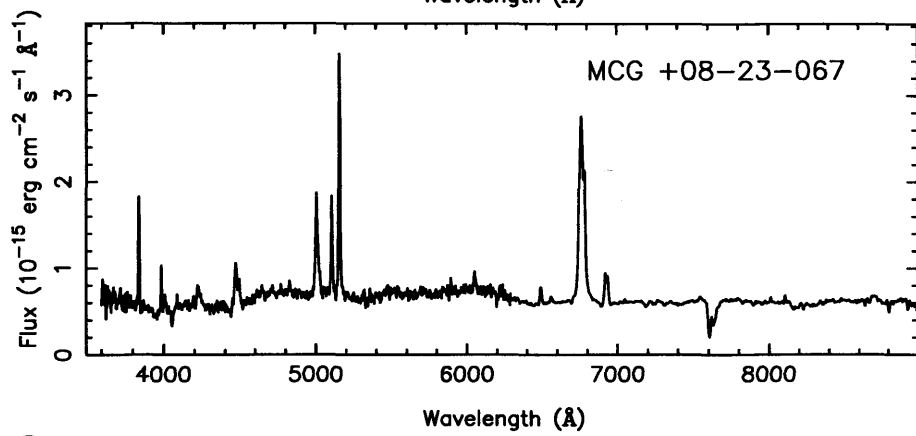
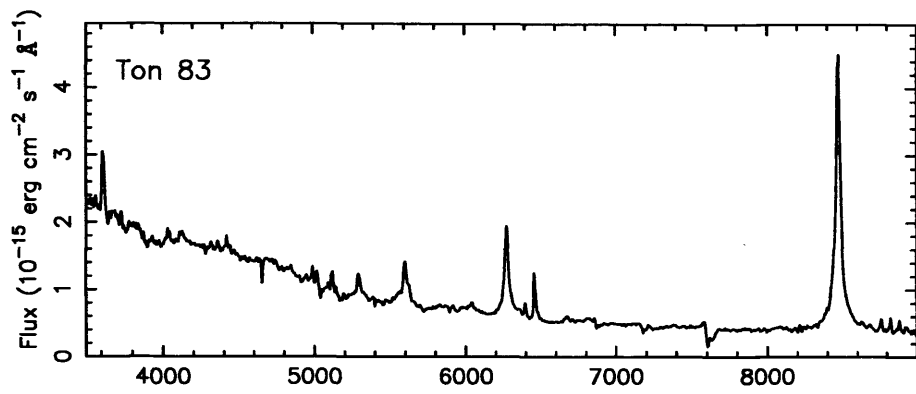
# Optical spectra

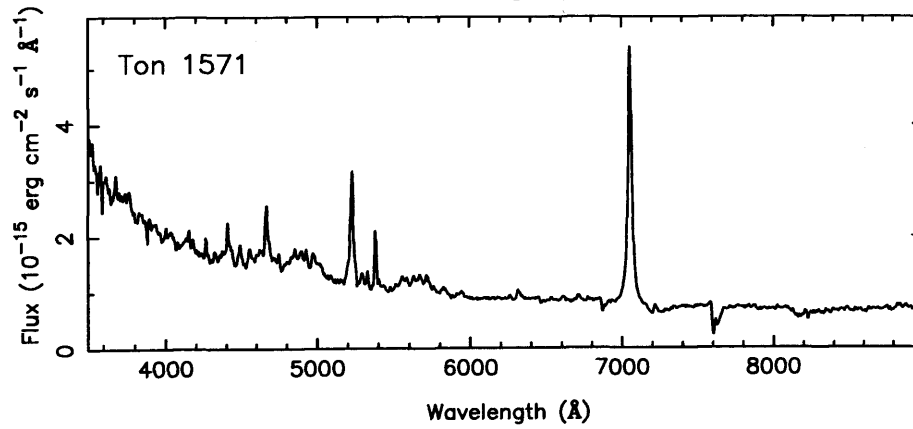
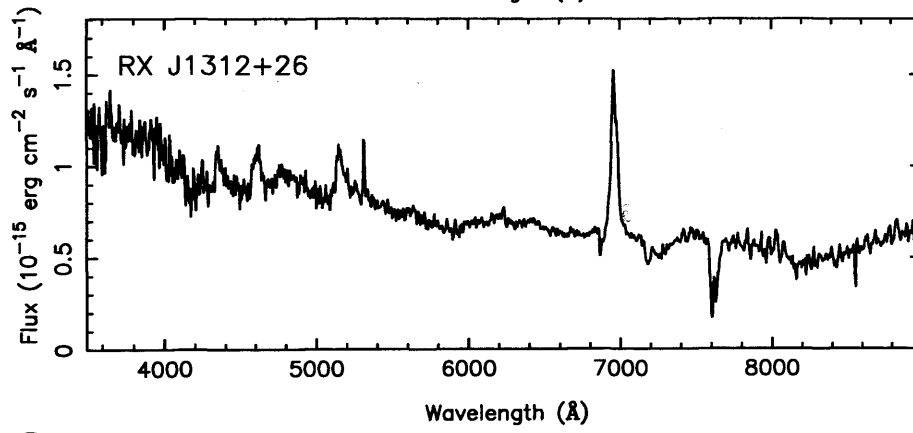
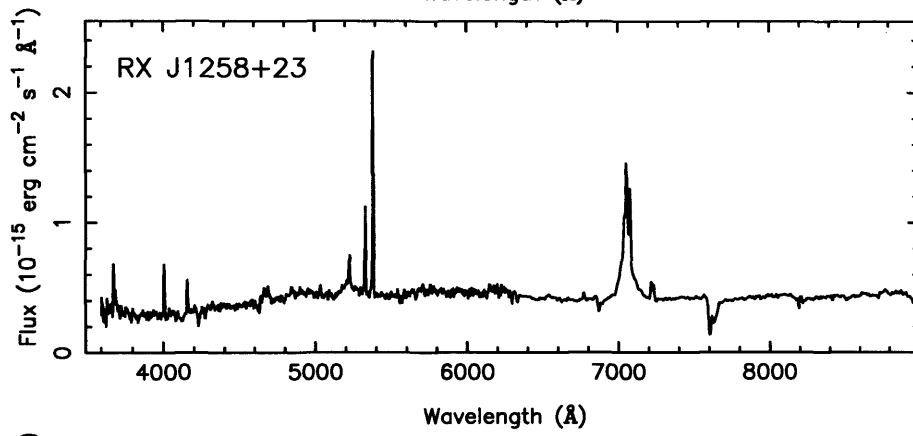
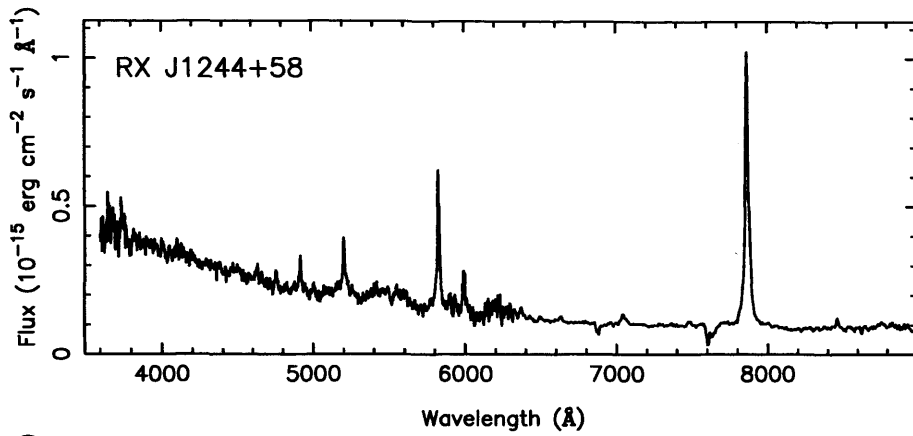
Figure A.1: Optical spectra of the 1/4 keV Seyfert sample described in Chapter 5, based on observations taken at the WHT and Shane telescopes. Data are shown in the observed wavelength frame.

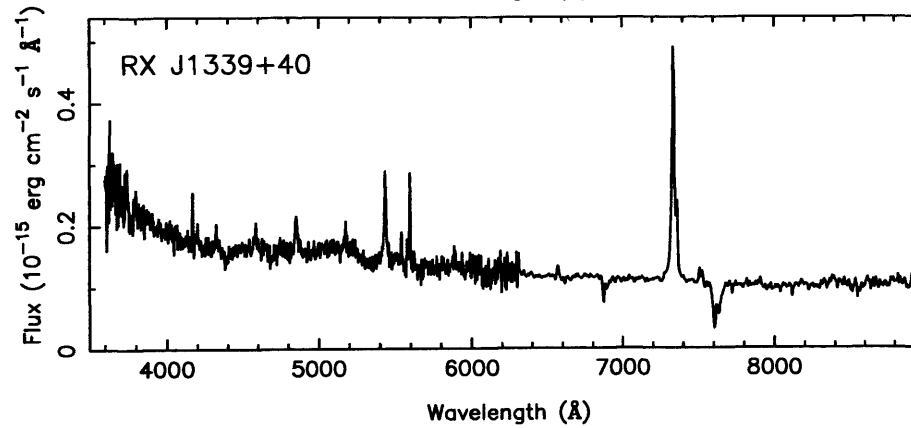
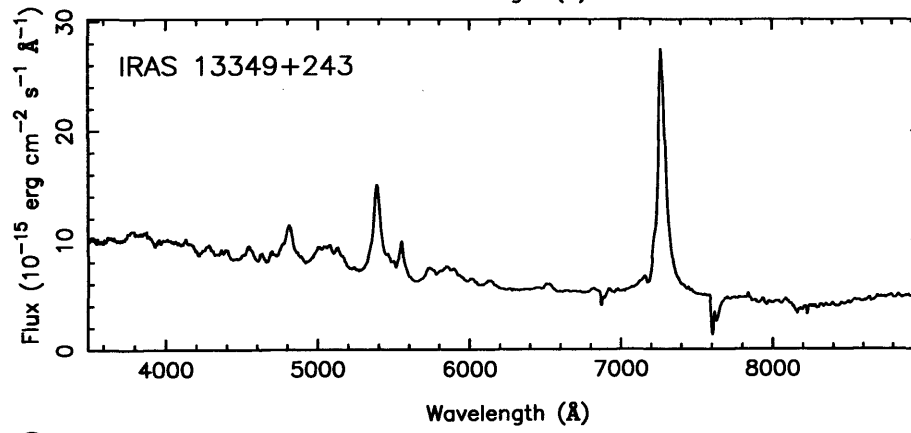
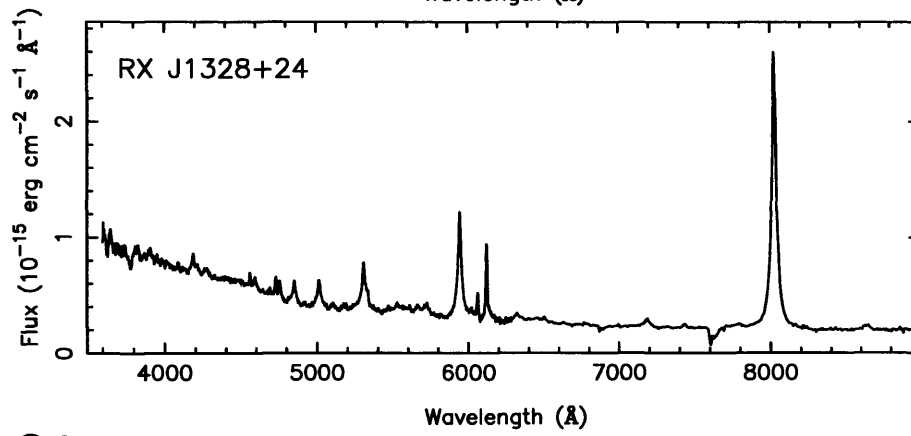
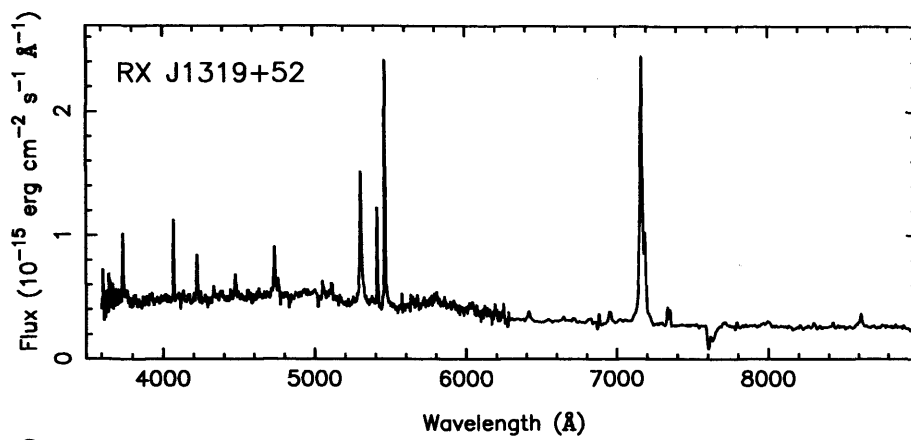


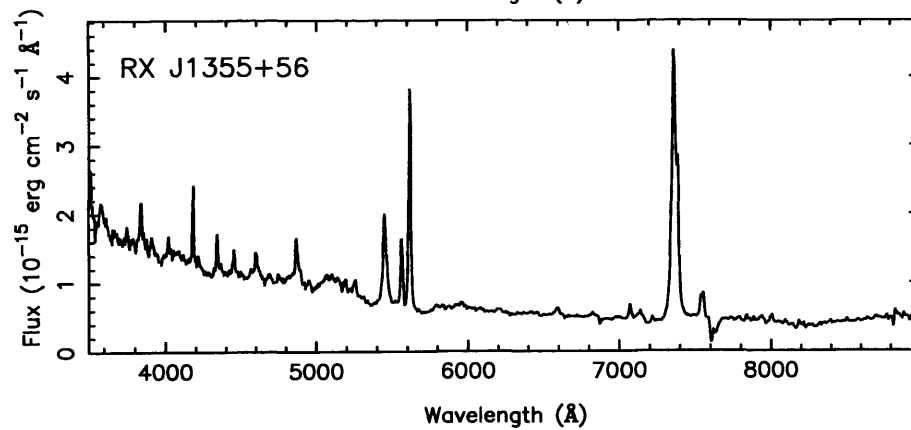
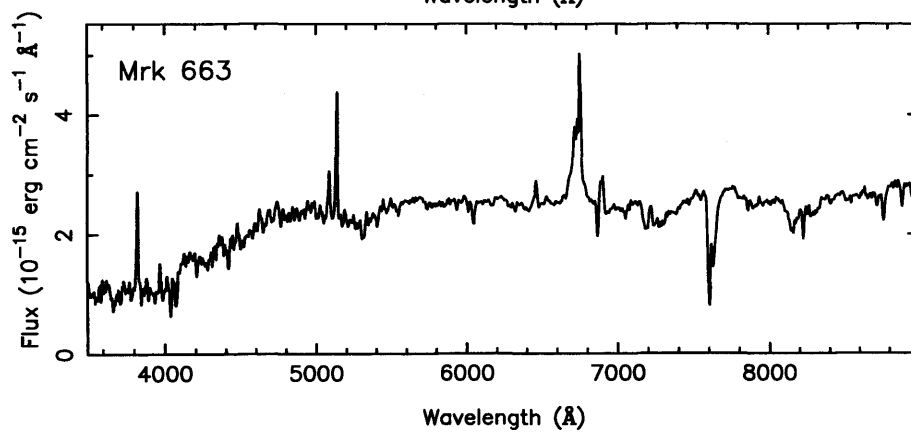
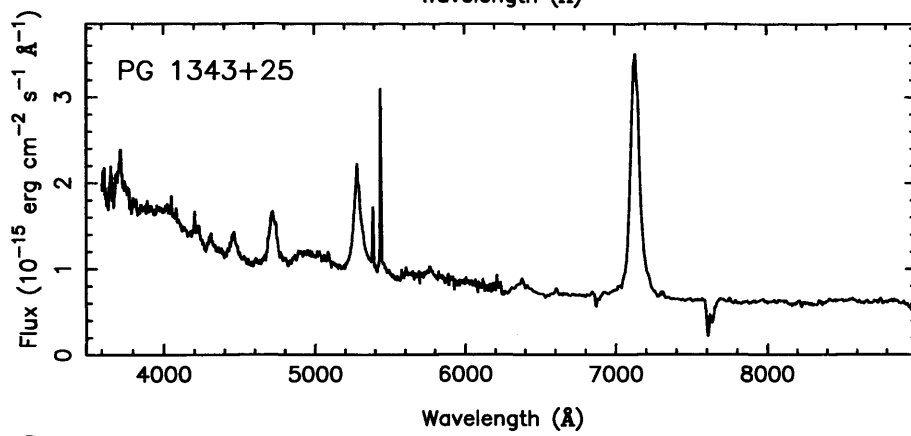
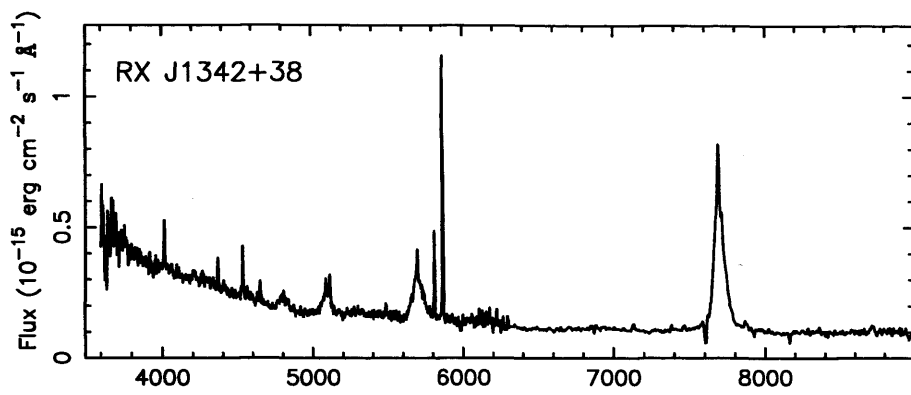


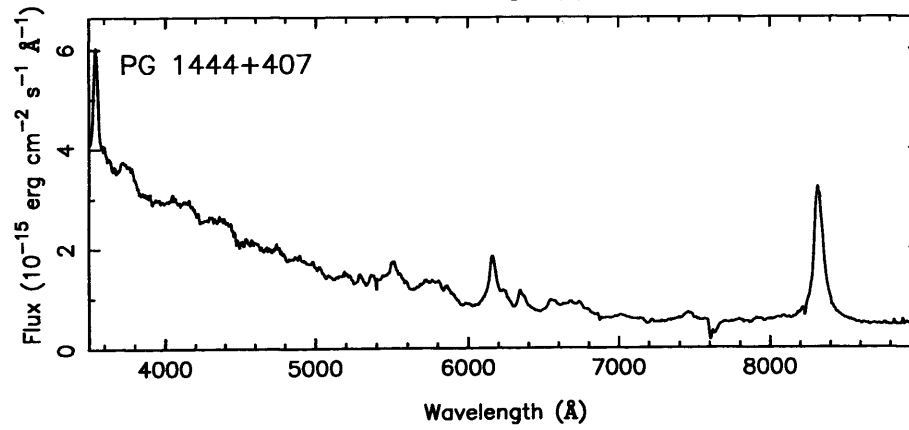
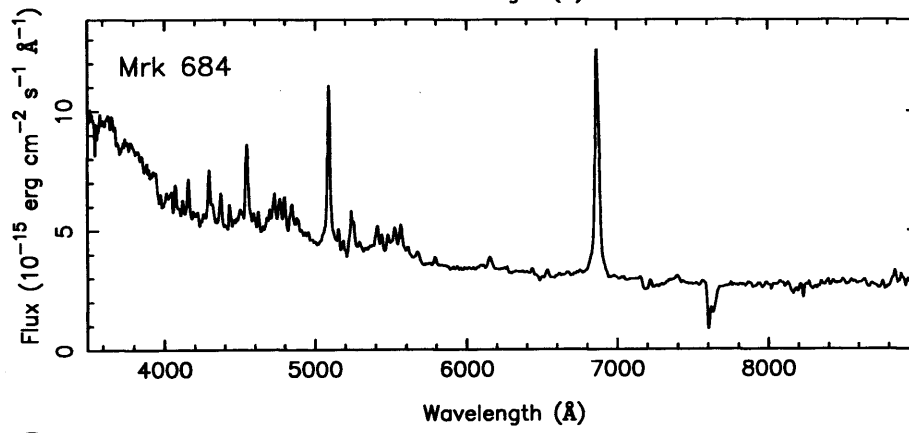
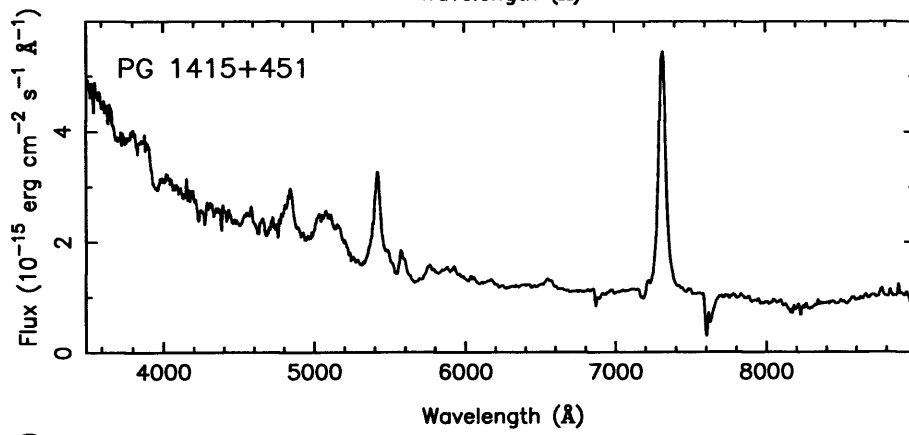
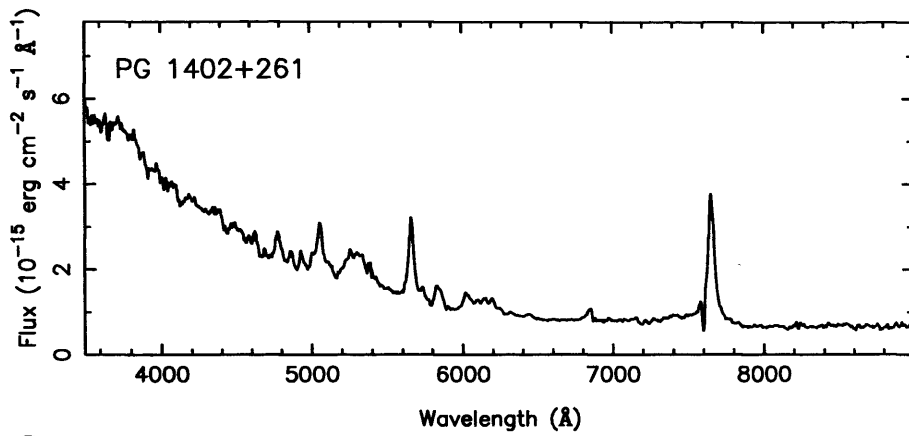


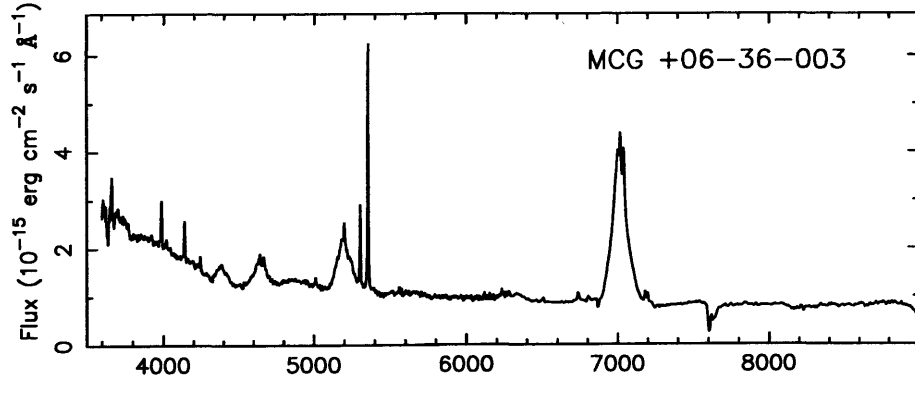
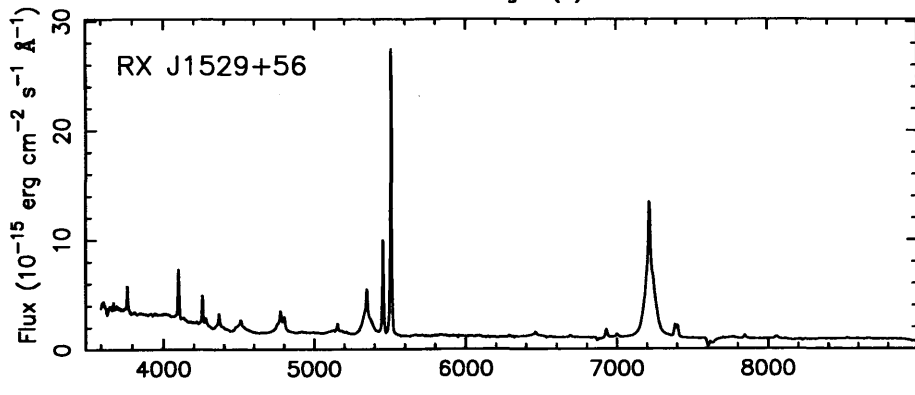
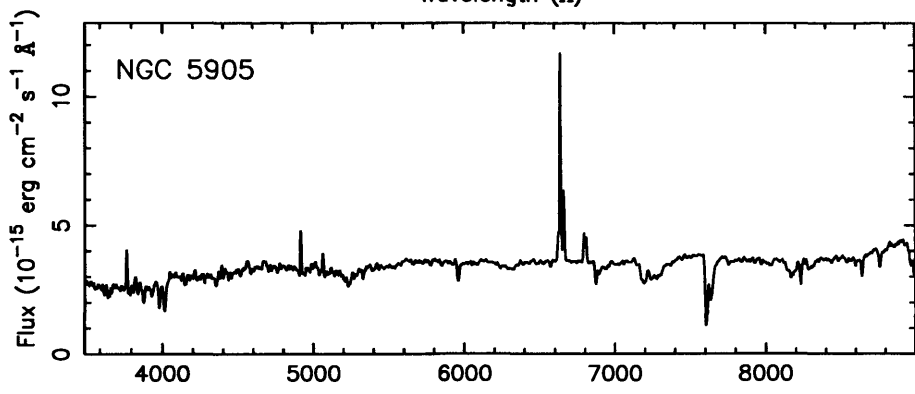
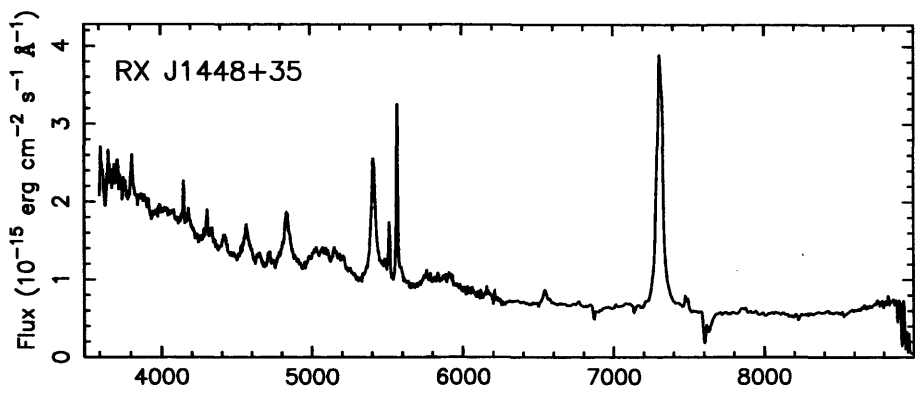


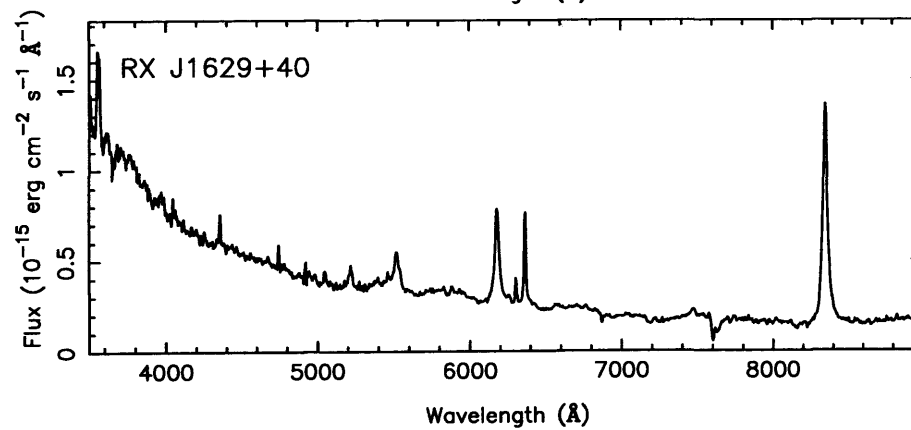
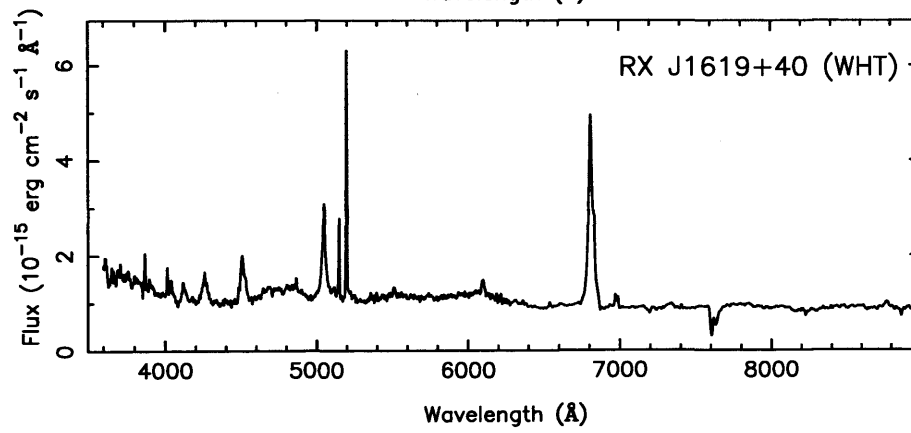
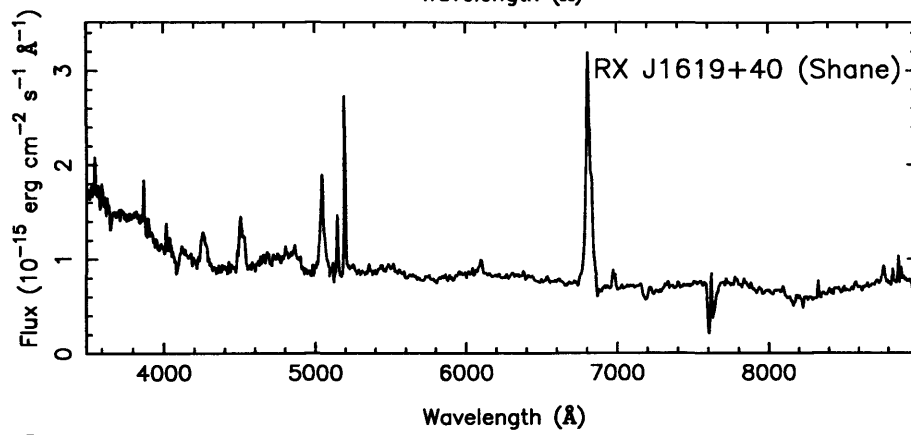
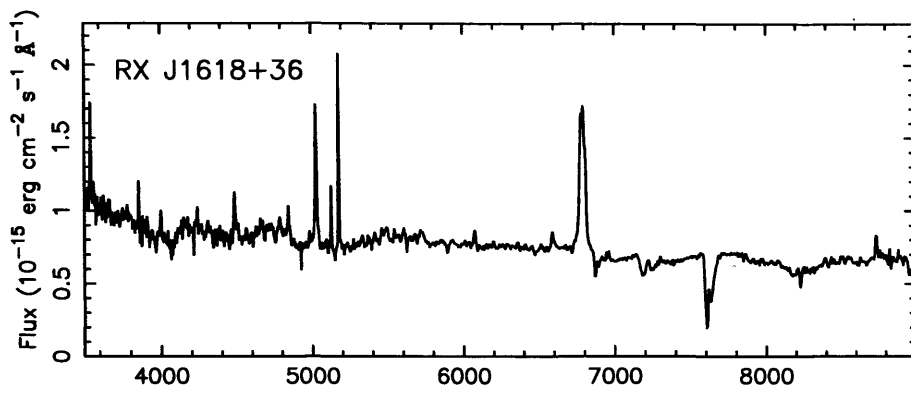


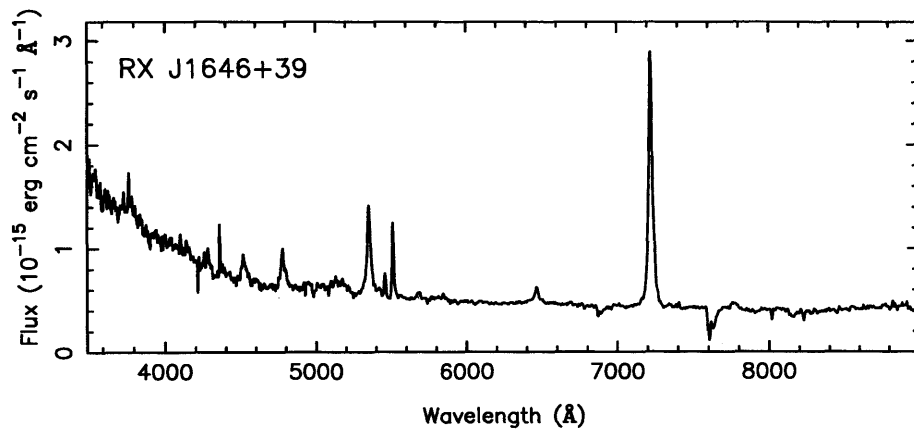












## References

- Antonucci, R. R. J. & Miller, J., 1985. *Astrophys. J.*, **297**, 621.
- Antonucci, R. R. J., 1993. *Ann. Rev. Astron. Astrophys.*, **31**, 473.
- Arnaud, K. A. *et al.*, 1985. *Mon. Not. R. astr. Soc.*, **217**, 105.
- Arnaud, K., 1996. In: *Astronomical Data Analysis Software and Systems*, Jacoby, G. & Barnes, J., eds., ASP Conf. Series Vol. 101, p. 17.
- Avni, Y. & Bahcall, J. N., 1980. *Astrophys. J.*, **235**, 694.
- Bade, N., Beckmann, V., Douglas, N. G., Barthel, P. D., Engels, D., Cordis, L., Nass, P. & Voges, W., 1998. *Astr. Astrophys.*, **334**, 459.
- Bade, N., Komossa, S. & Dahlem, M., 1996. *Astr. Astrophys.*, **309**, L35.
- Ballantyne, D. R., Iwasawa, K. & Fabian, A. C., 2000. *Mon. Not. R. astr. Soc.*, **323**, 506.
- Ballantyne, D. R., Ross, R. R. & Fabian, A. C., 2001. *Mon. Not. R. astr. Soc.*, **in press**, astro.
- Barr, P. & Mushotzky, R. F., 1986. *Nature*, **320**, 421.
- Bechtold, J., Czerny, B., Elvis, M., Fabbiano, G. & Green, R. F., 1987. *Astrophys. J.*, **314**, 699.
- Bedford, D. K., Vilhu, O. & Petrov, P., 1988. *Mon. Not. R. astr. Soc.*, **234**, 319.
- Bevington, P. R. & Robinson, D. K., 1992. *Data Reduction and Error Analysis for the Physical Sciences*, Mc Graw-Hill.
- Blandford, R. D. & McKee, C. F., 1982. *Astrophys. J.*, **255**, 419.
- Blandford, R. D. & Rees, M. J., 1978. In: *Pittsburgh Conference on BL Lac Objects, Pittsburgh, Pa., April 24-26, 1978, Proceedings. (A79-30026 11-90) Pittsburgh, Pa., University of Pittsburgh, 1978, p. 328-341; Discussion, p. 341-347. NATO-supported research, p. 328.*
- Blandford, R. D., McKee, C. F. & Rees, M. J., 1977. *Nature*, **267**, 211.
- Boller, Th., Brandt, W. N. & Fink, H., 1996. *Astr. Astrophys.*, **305**, 53.
- Boller, Th., Trümper, J., Molendi, S., Fink, H., Schæidt, S., Caulet, A. & Dennefeld, M., 1993. *Astr.*

*Astrophys.*, **279**, 53.

- Boller, T., Brandt, W. N., Fabian, A. C. & Fink, H. H., 1997. *Mon. Not. R. astr. Soc.*, **289**, 393.
- Boroson, T. A. & Green, R. F., 1992. *Astrophys. J. Suppl.*, **90**, 109.
- Boyle, B. J., Shanks, T. & Peterson, B. A., 1988. *Mon. Not. R. astr. Soc.*, **235**, 935.
- Brandt, W. N. & Boller, T., 1998. *Astronomische Nachrichten*, **319**, 163.
- Brandt, W. N., Fabian, A. C., Nandra, K., Reynolds, C. S. & Brinkmann, W., 1994. *Mon. Not. R. astr. Soc.*, **271**, 958.
- Brandt, W. N., Mathur, S., Reynolds, C. S. & Elvis, M., 1997. *Mon. Not. R. astr. Soc.*, **292**, 407.
- Brandt, W. N., Boller, T., Fabian, A. C. & Ruszkowski, M., 1999. *Mon. Not. R. astr. Soc.*, **303**, L53.
- Brandt, W. N., Mathur, S. & Elvis, M., 1997. *Mon. Not. R. astr. Soc.*, **285**, L25.
- Brandt, W. N., Pounds, K. A. & Fink, H., 1995. *Mon. Not. R. astr. Soc.*, **273**, L47.
- Brandt, W. N., 1996. *PhD thesis*, University of Cambridge.
- Branduardi-Raymont, G. *et al.*, 1989. In: *Two Topics in X-ray Astronomy*, Hunt, J. & Battrock, B., eds., ESA Publications, p. 713.
- Burke, B. E., Mountain, R. W., Harrison, D. C., Bautz, M. W., Doty, J. P., Ricker, G. R. & Daniels, P. J., 1991. *IEEE Trans. Nuc. Sci.*, ED-38, 1069.
- Chiang, J., Reynolds, C. S., Blaes, O. M., Nowak, M. A., Murray, N., Madejski, G., Marshall, H. L. & Magdziarz, P., 2000. *Astrophys. J.*, **528**, 292.
- Corbin, M. R. & Boroson, T. A., 1996. *Astrophys. J. Suppl.*, **107**, 69.
- Craig, N. & Fruscione, A., 1997. *Astron. J.*, **114**, 1356.
- Czerny, B. & Elvis, M., 1987. *Astrophys. J.*, **321**, 305.
- Day, C., Arnaud, K., Ebisawa, K., Gotthelf, E., Ingham, J., Mukai, K. & White, N. *The ABC Guide to ASCA Data Reduction*. NASA Goddard Space Flight Center, 1995.
- Dickey, J. M. & Lockman, F. J., 1990. *Ann. Rev. Astron. Astrophys.*, **28**, 215.

- Done, C. & Smith, D. A., 1996. *Vistas in Astronomy*, **40**, 209.
- Done, C. & Zycki, P. T., 1999. *Mon. Not. R. astr. Soc.*, **305**, 457.
- Edelson, E. A. & Malkan, M. A., 1987. *Astrophys. J.*, **323**, 516.
- Edelson, R. & Nandra, K., 1999. *Astrophys. J.*, **514**, 682.
- Edelson, R., Vaughan, S., Warwick, R., Puchnarewicz, E. & George, I., 1999. *Mon. Not. R. astr. Soc.*, **307**, 91.
- Edelson, R., Koratkar, A., Nandra, K., Goad, M., Peterson, B. M., Collier, S., Krolik, J., Malkan, M., Maoz, D., O'Brien, P., Shull, J. M., Vaughan, S. & Warwick, R., 2000. *Astrophys. J.*, **534**, 180.
- Edelson, R. A., Pike, G. F. & Krolik, J. H., 1990. *Astrophys. J.*, **359**, 86.
- Elvis, M. *et al.*, 1978. *Mon. Not. R. astr. Soc.*, **183**, 129.
- Elvis, M., Wilkes, B. J., McDowell, J. C., Green, R. F., Bechtold, J., Willner, S. P., Oey, M. S., Polomski, E. & Cutri, R., 1994. *Astrophys. J. Suppl.*, **95**, 1.
- Elvis, M., Wilkes, B. J. & Lockman, F. J., 1989. *Astron. J.*, **97**, 777.
- Fabian, A. C., Rees, M. J., Stella, L. & White, N. E., 1989. *Mon. Not. R. astr. Soc.*, **238**, 729.
- Fabian, A. C., Nandra, K., Reynolds, C. S., Brandt, W. N., Otani, C., Tanaka, Y., Inoue, H. & Iwasawa, K., 1995. *Mon. Not. R. astr. Soc.*, **277**, 11P.
- Fabian, A. C., 1979. *Royal Society of London Proceedings Series*, **366**, 449.
- Falomo, R., Pesce, J. & Lockman, F. J., 1993. *Astrophys. J. Letts.*, **411**, 61.
- Ferland, G. J. & Osterbrock, D. E., 1986. *Astrophys. J.*, **300**, 658.
- Fiore, F., Matt, G., Cappi, M., Elvis, M., Leighly, K. M., Nicastro, F., Piro, L., Siemiginowska, A. & Wilkes, B. J., 1998. *Mon. Not. R. astr. Soc.*, **298**, 103.
- Forster, K. & Halpern, J. P., 1996. *Astrophys. J.*, **468**, 565.
- Francis, P. J. & Wills, B. J., 1999. In: *ASP Conf. Ser. 162: Quasars and Cosmology*, Ferland, G. & Baldwin, J., eds., p. 363.
- Francis, P. J., Hewett, P. C., Foltz, C. B. & Chaffee, F. H., 1992. *Astrophys. J.*, **398**, 476.

- Frank, J., King, A. R. & Raine, D. J., 1992. *Accretion Power in Astrophysics*, Cambridge University Press.
- Fruscione, A., 1996. *Astrophys. J.*, **459**, 509.
- Galeev, A. A., Rosner, R. & Vaiana, G. S., 1979. *Astrophys. J.*, **229**, 318.
- Gaskell, C. M., 1985. *Astrophys. J.*, **291**, 112.
- Gaskell, C. M., 2000. *New Astronomy Review*, **44**, 563.
- Gebhardt, K., Bender, R., Bower, G., Dressler, A., Faber, S. M., Filippenko, A. V., Green, R., Grillmair, C., Ho, L. C., Kormendy, J., Lauer, T. R., Magorrian, J., Pinkney, J., Richstone, D. & Tremaine, S., 2000. *Astrophys. J. Letts.*, **539**, 13.
- George, I. M. & Fabian, A. C., 1991. *Mon. Not. R. astr. Soc.*, **249**, 352.
- George, I. M., Turner, T. J., Netzer, H., Nandra, K., Mushotzky, R. F. & Yaqoob, T., 1998. *Astrophys. J. Suppl.*, **114**, 73.
- George, I. M., Turner, T. J., Yaqoob, T., Netzer, H., Laor, A., Mushotzky, R. F., Nandra, K. & Takahashi, T., 2000. *Astrophys. J.*, **531**, 52.
- Ghez, A. M., Klein, B. L., Morris, M. & Becklin, E. E., 1998. *Astrophys. J.*, **509**, 678.
- Goad, M., 2001. In: *Probing the Physics of Active Galactic Nuclei by Multiwavelength Monitoring*, Peterson, B. M., Polidan, R. S. & Pogge, R. W., eds., ASP Conferences Series, Vol TBD, p. TBD.
- Goodrich, R. W., 1989. *Astrophys. J.*, **342**, 224.
- Green, A. R., McHardy, I. M. & Lehto, H. J., 1993. *Mon. Not. R. astr. Soc.*, **265**, 664.
- Greenhill, L. J., Jiang, D. R., Moran, J. M., Reid, M. J., Lo, K. Y. & Claussen, M. J., 1995. *Astrophys. J.*, **440**, 619.
- Griffiths, R. G., Warwick, R. S., Georgantopoulos, I., Done, C. & Smith, D. A., 1998. *Mon. Not. R. astr. Soc.*, **298**, 1159.
- Grupe, D., Beuerman, K., Mannheim, K., Thomas, H. ., Fink, H. H. & de Martino, D., 1995a. *Astr. Astrophys.*, **300**, L21.

- Grupe, D., Beuermann, K., Mannheim, K., Bade, N., Thomas, H. ., de Martino, D. & Schwope, A., 1995b. *Astr. Astrophys.*, **299**, L5.
- Grupe, D., Beuermann, K., Thomas, H. C., Mannheim, K. & Fink, H. H., 1998a. *Astr. Astrophys.*, **330**, 25.
- Grupe, D., Wills, B. J., Wills, D. & Beuermann, K., 1998b. *Astr. Astrophys.*, **333**, 827.
- Grupe, D., Beuermann, K., Mannheim, K. & Thomas, H. C., 1999. *Astr. Astrophys.*, **350**, 805.
- Grupe, D., 1996. *PhD thesis*, University of Göttingen.
- Guainazzi, M., Mihara, T., Otani, C. & Matsuoka, M., 1986. *Pub. Astr. Soc. Japan.*, **48**, 781.
- Guainazzi, M. *et al.*, 1998. *Astr. Astrophys.*, **339**, 327.
- Guilbert, P. W. & Rees, M. J., 1988. *Mon. Not. R. astr. Soc.*, **233**, 475.
- Haardt, F. & Maraschi, L., 1993. *Astrophys. J.*, **413**, 507.
- Haardt, F., 1997. *Memorie della Societa Astronomica Italiana*, **68**, 73.
- Halpern, J. P. & Moran, E. C., 1998. *Astrophys. J.*, **494**, 194.
- Halpern, J. P. & Oke, J. B., 1987. *Astrophys. J.*, **312**, 91.
- Halpern, J. P., Leighly, K. M., Marshall, H. L., Eracleous, M. & Storchi-Bergmann, T., 1998. *Pub. Astr. Soc. Pacific.*, **110**, 1394.
- Halpern, J. P., 1984. *Astrophys. J.*, **281**, 90.
- Hasinger, G., Burg, R., Giacconi, R., Schmidt, M., Trumper, J. & Zamorani, G., 1998. *Astr. Astrophys.*, **329**, 482.
- Hasinger, G., Lehmann, I., Schmidt, M., Gunn, J. E., Schneider, D. P., Giacconi, R., Trümper, J. & Zamorani, G., 2000. *New Astronomy Review*, **44**, 497.
- Haywood, M., Robin, A. C. & Creze, M., 1997. *Astr. Astrophys.*, **320**, 440.
- Heckman, T. M., 1980. *Astr. Astrophys.*, **87**, 152.
- Ho, L. C., Filippenko, A. V. & Sargent, W. L. W., 1993. *Astrophys. J.*, **417**, 63.

- Horne, K., 1986. *Pub. Astr. Soc. Pacific.*, **98**, 609.
- Huchra, J. & Burg, R., 1992. *Astrophys. J.*, **393**, 90.
- Iwasawa, K., Brandt, W. N. & Fabian, A. C., 1998. *Mon. Not. R. astr. Soc.*, **293**, 251.
- Iwasawa, K., Fabian, A. C. & Nandra, K., 1999. *Mon. Not. R. astr. Soc.*, **307**, 611.
- Kaastra, J. S. & Mewe, R., 1993. *Astr. Astrophys. Suppl.*, **97**, 443.
- Kaspi, S., Smith, P. S., Netzer, H., Maoz, D., Jannuzi, B. T. & Giveon, U., 2000. *Astrophys. J.*, **533**, 631.
- Kellermann, K. I., Sramek, R., Schmidt, M., Shaffer, D. B. & Green, R., 1989. *Astron. J.*, **98**, 1195.
- Khachikian, E. Y. & Weedman, D. W., 1974. *Astrophys. J.*, **192**, 581.
- Kohmura, Y. *et al.*, 1993. *Proc. SPIE Int. Soc. Opt. Eng.*, **2006**, 78.
- Komossa, S. & Bade, N., 1999a. *Astr. Astrophys.*, **331**, L49.
- Komossa, S. & Bade, N., 1999b. *Astr. Astrophys.*, **343**, 775.
- Komossa, S. & Fink, H., 1998. In: *Highlights in X-ray astronomy*, Aschenbach, B. *et al.*, eds., p. astro.
- Koratkar, A. & Blaes, O., 1999. *Pub. Astr. Soc. Pacific.*, **111**, 1.
- Kormendy, J. & Richstone, D., 1995. *Ann. Rev. Astron. Astrophys.*, **33**, 581.
- Kuraszkiewicz, J., Wilkes, B. J., Brandt, W. N. & Vestergaard, M., 2000a. *Astrophys. J.*, **542**, 631.
- Kuraszkiewicz, J., Wilkes, B. J., Czerny, B. & Mathur, S., 2000b. *Astrophys. J.*, **542**, 692.
- Laor, A., Fiore, F., Martin, E., Wilkes, B. J. & McDowell, J. C., 1997. *Astrophys. J.*, **477**, 93.
- Laor, A., 2000. *New Astronomy Review*, **44**, 503.
- Lawrence, A. & Papadakis, I., 1993. *Astrophys. J. Letts.*, **414**, 85.
- Lawrence, A., Elvis, M., Wilkes, B. J., McHardy, I. & Brandt, N., 1997. *Mon. Not. R. astr. Soc.*, **285**, 879.
- Lawrence, A., 1987. *Pub. Astr. Soc. Pacific.*, **99**, 309.
- Leighly, K. M., Mushotzky, R. F., Yaqoob, T., Lunieda, H. & Edelson, R., 1996. *Astrophys. J.*, in press.

- Leighly, K. M., and B. J. Wills, L. E. K., Wills, D. & Grupe, D., 1997a. *Astrophys. J.*, **489**, L137.
- Leighly, K. M., Mushotzky, R. F., Nandra, K. & Forster, K., 1997b. *Astrophys. J.*, **489**, L25.
- Leighly, K. M., 1999. *Astrophys. J. Suppl.*, **125**, 297.
- Leighly, K. M., 2000. *New Astronomy Review*, **44**, 395.
- Lightman, A. P. & White, T. R., 1988. *Astrophys. J.*, **335**, 57.
- Lipari, S., Terlevich, R. & Macchetto, F., 1993. *Astrophys. J.*, **406**, 451.
- Lockman, F. J., Jahoda, K. & McCammon, D., 1986. *Astrophys. J.*, **302**, 432.
- Lynden-Bell, D., 1969. *Nature*, **223**, 690.
- Maccacaro, T., Gioia, I. M., Maccagni, D. & Stocke, J. T., 1984. *Astrophys. J. Letts.*, **284**, 23.
- Madau, P., 1988. *Astrophys. J.*, **327**, 116.
- Magdziarz, P. & Zdziarski, A. A., 1995. *Mon. Not. R. astr. Soc.*, **273**, 837.
- Malkan, M. A. & Sargent, W. L. W., 1982. *Astrophys. J.*, **254**, 22.
- Marshall, H. L., Fruscione, A. & Carone, T. E., 1995. *Astrophys. J.*, **439**, 90.
- Marshall, N., Warwick, R. S. & Pounds, K. A., 1981. *Mon. Not. R. astr. Soc.*, **194**, 987.
- Marshall, H. L., 1985. *Astrophys. J.*, **299**, 109.
- Matt, G., Fabian, A. C. & Ross, R. R., 1993. *Mon. Not. R. astr. Soc.*, **262**, 179.
- Matt, G., Perola, G. C. & Piro, L., 1991. *Astr. Astrophys.*, **247**, 25.
- McHardy, I. M., 1989. In: *Two Topics in X-ray Astronomy*, Hunt, J. & Battrick, B., eds., ESA Publications, p. 1111.
- Miller, J. S., 1975. *Astrophys. J. Letts.*, **201**, 109.
- Mushotzky, R. F., Done, C. & Pounds, K. A., 1993. *Ann. Rev. Astron. Astrophys.*, **31**, 717.
- Nandra, K. & Pounds, K. A., 1992. *Nature*, **359**, 215.
- Nandra, K. & Pounds, K. A., 1994. *Mon. Not. R. astr. Soc.*, **268**, 405.

- Nandra, K., George, I. M., Mushotsky, R. F., Turner, T. J. & Yaqoob, T., 1997a. *Astrophys. J.*, **476**, 70.
- Nandra, K., George, I. M., Mushotsky, R. F., Turner, T. J. & Yaqoob, T., 1997b. *Astrophys. J.*, **477**, 602.
- Nandra, K., Clavel, J., Edelson, R. A., George, I. M., Malkan, M. A., Mushotzky, R. F., Peterson, B. M. & Turner, T. J., 1998. *Astrophys. J.*, **505**, 594.
- Nandra, K., George, I. M., Mushotsky, R. F., Turner, T. J. & Yaqoob, T., 1999. *Astrophys. J. Letts.*, **523**, 17.
- Nayakshin, S., Kazanas, D. & Kallman, T., 2000. *Astrophys. J.*, .
- Netzer, H. & Peterson, B. M., 1997. In: *Astronomical Time Series*, Maoz, D., Sternberg, A. & Leibowitz, E., eds., p. 85.
- Netzer, H., 1991. In: *Active Galactic Nuclei; Saas Fee Advanced Course 20*, T. J. L. Courvoiser, M. M., ed., Springer-Verlag, Berlin, p. 57.
- Netzer, H., 1993. *Astrophys. J.*, **411**, 594.
- Nicastro, F., Fiore, F. & Matt, G., 1999. *Astrophys. J.*, **517**, 108.
- Oke, J. B. & Lauer, T. R., 1979. *Astrophys. J.*, **230**, 360.
- Osterbrock, D. E. & Pogge, R. W., 1985. *Astrophys. J.*, **297**, 166.
- Osterbrock, D. E., 1977. *Astrophys. J.*, **215**, 733.
- Otani, C., Kii, T. & Miya, K., 1996. In: *Roentgenstrahlung from the Universe*, Zimmermann, H. U., Trümper, J. & Yorke, H., eds., p. 491.
- Page, M. J. & Carrera, F. J., 2000. *Mon. Not. R. astr. Soc.*, **311**, 433.
- Peterson, B. M., 1993. *Pub. Astr. Soc. Pacific.*, **105**, 247.
- Peterson, B. M., 1997. *An introduction to active galactic nuclei*, Cambridge University Press.
- Phillips, M. M., 1978. *Astrophys. J.*, **226**, 736.
- Piccinotti, G., Mushotzky, R. F., Boldt, E. A., Holt, S. S., Marshall, F. E., Serlenitsos, P. J. & Shafer, R. A., 1982. *Astrophys. J.*, **253**, 485.
- Pogge, R. W., 2000. *New Astronomy Review*, **44**, 381.

- Polomski, E., Vennes, S., Thorstensen, J. R., Mathioudakis, M. & Falco, E. E., 1997. *Astrophys. J.*, **486**, 179.
- Pounds, K. & Vaughan, S., 2000. *New Astronomy Review*, **44**, 431.
- Pounds, K. A., Done, C. & Osborne, J. O., 1995. *Mon. Not. R. astr. Soc.*, **277**, L5.
- Pounds, K. A., Nandra, K., Stewart, G. C., George, I. M. & Fabian, A., 1990. *Nature*, **344**, 132.
- Pounds, K. A. *et al.*, 1993. *Mon. Not. R. astr. Soc.*, **260**, 77.
- Pounds, K. A., Turner, T. J. & Warwick, R. S., 1986. *Mon. Not. R. astr. Soc.*, **221**, 7.
- Press, W. H., Teukolsky, S. A., Vetterling, W. T. & Flannery, B. P., 1992. *Numerical recipes in FORTRAN. The art of scientific computing*, Cambridge: University Press, —c1992, 2nd ed.
- Pringle, J. E., 1981. *Ann. Rev. Astron. Astrophys.*, **19**, 137.
- Puchnarewicz, E. M. & Mason, K. O., 1998. *Mon. Not. R. astr. Soc.*, **293**, 243.
- Puchnarewicz, E. M. *et al.*, 1992. *Mon. Not. R. astr. Soc.*, **256**, 589.
- Puchnarewicz, E. M., Mason, K. O., Siemiginowska, A. & Pounds, K. A., 1995. *Mon. Not. R. astr. Soc.*, **276**, 20.
- Puchnarewicz, E. M., Mason, K. O. & Cordova, F. A., 1994. *Mon. Not. R. astr. Soc.*, **270**, 663.
- Pye, J. P. *et al.*, 1995. *Mon. Not. R. astr. Soc.*, **274**, 1165.
- Rees, M. J., 1984. *Ann. Rev. Astron. Astrophys.*, **22**, 471.
- Reeves, J. N., Turner, M. J. L., Ohashi, T. & Kii, T., 1997. *Mon. Not. R. astr. Soc.*, **292**, 468.
- Reeves, J. N., O'Brien, P. T., Vaughan, S., Law-Green, D., Ward, M., Simpson, C., Pounds, K. A. & Edelson, R., 2000. *Mon. Not. R. astr. Soc.*, **312**, L17.
- Remillard, R. A., Grossan, B., Bradt, H. V., Ohashi, T. & Hayashida, K., 1991. *Nature*, **350**, 589.
- Reynolds, C. S. & Fabian, A. C., 1995. *Mon. Not. R. astr. Soc.*, **273**, 1167.
- Reynolds, C. S., 1997. *Mon. Not. R. astr. Soc.*, **286**, 513.
- Ross, R. R., Fabian, A. C. & Mineshige, S., 1992. *Mon. Not. R. astr. Soc.*, **258**, 189.

- Ross, R. R., Fabian, A. C. & Young, A. J., 1999. *Mon. Not. R. astr. Soc.*, **306**, 461.
- Sako, M., Kahn, S. M., Behar, E., Kaastra, J. S., Brinkman, A. C., Boller, T., Puchnarewicz, E. M., Starling, R., Liedahl, D. A., Clavel, J. & Santos-Lleo, M., 2001. *Astr. Astrophys.*, **in press.**, astro.
- Sambruna, R. *et al.*, 1997. *Astrophys. J.*, **483**, 774.
- Schmidt, M. & Green, R. F., 1983. *Astrophys. J.*, **269**, 352.
- Schmidt, M., Hasinger, G., Gunn, J., Schneider, D., Burg, R., Giacconi, R., Lehmann, I., MacKenty, J., Trumper, J. & Zamorani, G., 1998. *Astr. Astrophys.*, **329**, 495.
- Schmidt, M., 1968. *Astrophys. J.*, **151**, 393.
- Schwope, A. D., Hasinger, G., Lehmann, I., Scharz, R., Brunner, H., Neizvestny, S., Ugryumov, A., Balega, Y., Trumper, J. & Voges, W., 2000. *Astronomische Nachrichten*, **321**, 1.
- Sembay, S., Hanson, C. G. & Coe, M. J., 1987. *Mon. Not. R. astr. Soc.*, **226**, 137.
- Shakura, N. I. & Sunyaev, R. A., 1973. *Astr. Astrophys.*, **24**, 337.
- Shields, G. A., 1978. *Nature*, **272**, 706.
- Shuder, J. M. & Osterbrock, D. E., 1981. *Astrophys. J.*, **250**, 55.
- Shull, J. M., Roberts, D., Giroux, M. L., Penton, S. V. & Fardal, M. A., 1999. *Astron. J.*, **118**, 1450.
- Sims, M. R. *et al.*, 1990. *Optical Engineering*, **29**, 649.
- Stephens, S. A., 1989. *Astron. J.*, **97**, 10.
- Strassmeier, K. G., Hall, D. S., Fekel, F. C. & Scheck, M., 1993. *Astr. Astrophys. Suppl.*, **100**, 173.
- Svensson, R., 1996. *Astr. Astrophys. Suppl.*, **120**, 475.
- Szuskiewicz, W., Malkan, M. & Abramowicz, M. A., 1996. *Astrophys. J.*, **458**, 474.
- Tanaka, Y. *et al.*, 1995. *Nature*, **375**, 659.
- Tanaka, Y., Inoue, H. & Holt, S. S., 1994. *Pub. Astr. Soc. Japan.*, **46**, L37.
- Tananbaum, H., Avni, Y., Branduardi, G., Elvis, M., Fabbiano, G., Feigelson, E., Giacconi, R., Henry, J. P., Pye, J. P., Soltan, A. & Zamorani, G., 1979. *Astrophys. J. Letts.*, **234**, 9.

- Terashima, Y., Ho, L. C. & Ptak, A. F., 2000. *Astrophys. J.*, **539**, 161.
- Thorne, K. S., 1974. *Astrophys. J.*, **191**, 507.
- Trümper, J. *et al.*, 1991. *Nature*, **349**, 579.
- Turner, T. J. & Pounds, K. A., 1989. *Mon. Not. R. astr. Soc.*, **240**, 833.
- Turner, T. J. *et al.*, 1999a. *Astrophys. J.*, **510**, 178.
- Turner, T. J., George, I. M., Nandra, K. & Turcan, D., 1999b. *Astrophys. J.*, **524**, 667.
- Turner, T. J., George, I. M. & Nandra, K., 1998. *Astrophys. J.*, **508**, 648.
- Turner, T. J., George, I. M. & Netzer, H., 1999. *Astrophys. J.*, **526**, 52.
- Uttley, P., McHardy, I. M., Papadakis, I. E., Cagnoni, I. & Fruscione, A., 2000. *Mon. Not. R. astr. Soc.*, **312**, 880.
- Uttley, P., 2000. *PhD thesis*, University of Southampton.
- Vallenari, A., Bertelli, G. & Schmidtobreick, L., 2000. *Astr. Astrophys.*, **361**, 73.
- Vaughan, S., Pounds, K. A., Reeves, J., Warwick, R. & Edelson, R., 1999. *Mon. Not. R. astr. Soc.*, **308**, L34.
- Vennes, S., Thejll, P. A., Galvan, R. G. & Dupuis, J., 1997. *Astrophys. J.*, **480**, 714.
- Véron-Cetty, M. P., Véron, P. & Gonçalves, A. C., 2001. *Astr. Astrophys.*, **in press**, astro-ph/0104151.
- Voges, W. *et al.*, 1999. *Astr. Astrophys.*, **349**, 389.
- Walter, R. & Fink, H. H., 1993. *Astr. Astrophys.*, **274**, 105.
- Wandel, A. & Boller, T., 1998. *Astr. Astrophys.*, **331**, 884.
- Wandel, A., Peterson, B. M. & Malkan, M. A., 1999. *Astrophys. J.*, **526**, 579.
- Wang, T., Brinkmann, B. & Bergeron, J., 1996. *Astr. Astrophys.*, **309**, 81.
- Watson, W. D. & Wallin, B. K., 1994. *Astrophys. J. Letts.*, **432**, 35.
- Weaver, K. A., Gelbord, J. & Yaqoob, T., 2001. *Astrophys. J.*, **550**, 261.

Wills, B. J., Wills, D., Evans II, N. J., Natta, A., Thompson, K. L., Breger, M. & Sitko, M. L., 1992. *Astrophys. J.*, **400**, 96.

Wills, B. J., Laor, A., Brotherton, M. S., Wills, D., Wilkes, B. J., Ferland, G. J. & Shang, Z., 1999. *Astrophys. J.*, **515**, 53.

Wills, B., 1982. In: *IAU Symp. 97: Extragalactic Radio Sources*, p. 373.

Xu, D. W., Wei, J. Y. & Hu, J. Y., 1999. *Astrophys. J.*, **517**, 622.

Zheng, W. & O'Brien, P. T., 1990. *Astrophys. J.*, **353**, 433.

Zycki, P. T., Done, C. & Smith, D. A., 1997. *Astrophys. J. Letts.*, **488**, 113.

Zycki, P. T., Done, C. & Smith, D. A., 1998. *Astrophys. J. Letts.*, **496**, 25.